Spring 5-16-2011

Indirect Detection of Axonal Architecture With Q-Space Imaging

Henry H. Ong
University of Pennsylvania, ongh@seas.upenn.edu

Indirect Detection of Axonal Architecture With Q-Space Imaging

Abstract
Evaluating axon morphology would provide insights into connectivity, maturation, and disease pathology. Conventional diffusion MRI can provide metrics that are related to axon morphology, but cannot measure specific parameters such as mean axon diameter (MAD) and intracellular fraction (ICF). Q-space imaging (QSI) is an advanced diffusion MRI technique that may be able to provide more information on axon morphology. However, QSI has several limitations that affect its implementation and accuracy.

The main objective of this dissertation was to address these limitations and to evaluate the potential of QSI to accurately assess axon morphology. First, a custom-built high-amplitude gradient coil was used to address the limitations in the maximum gradient amplitude available with commercial systems. Second, to understand the relationship between axon morphology and QSI, simulations were used to investigate the effects of the presence of both extracellular and intracellular signals (ECS and ICS) as well as variation in cell size and shape. Third, three QSI-based methods were designed provide specific measures of axon morphology which have not been reported before.

The maximum amplitude of the custom gradient coil was 50 T/m that, for the first time, allowed for sub-micron displacement resolution while fulfilling the short gradient approximation. This enabled near-ideal QSI experiments to be performed. QSI experiments on excised mouse spinal cords showed good correlation with histology, but overestimated MAD. Simulations showed that axon morphology was the dominant effect on QSI and suggested that the presence of ECS and ICS signals may complicate interpretation.

Three methods were designed to account for signal in ECS and ICS: two relied on a two-compartment model of the displacement probability density function and the echo attenuation at low q-values, and a third varied the gradient duration to differentiate diffusion in ECS from ICS. All three methods provided estimates of MAD and ICF that showed better agreement with histology than QSI. The methods were also evaluated implementation on a clinical scanner.

This dissertation demonstrated the sensitivity of QSI to axon morphology and showed the feasibility of three methods to accurately estimate MAD and ICF. Further investigation is warranted to study future applications.

Degree Type
Dissertation

Degree Name
Doctor of Philosophy (PhD)

Graduate Group
Bioengineering

First Advisor
Felix W. Wehrli

Keywords
MRI, white matter, mouse, diffusion, q-space simulation, spinal cord

Subject Categories
Biomedical Engineering and Bioengineering

INDIRECT DETECTION OF AXONAL ARCHITECTURE WITH Q-SPACE IMAGING

Henry H. Ong

A DISSERTATION in Bioengineering

Presented to the Faculties of the University of Pennsylvania in Partial Fulfillment of the Requirements for the Degree of Doctor of Philosophy

2011

_____

Felix W. Wehrli, Ph.D.

Supervisor of Dissertation

_____

Christopher S. Chen, M.D., Ph.D.

Graduate Group Chair

Committee Members:

Charles L. Epstein, Ph.D., Professor of Mathematics (Chair)

Hee Kwon Song, Ph.D., Associate Professor of Radiology

Ravinder Reddy, Ph.D., Professor of Radiology

Indirect Detection of Axonal Architecture with Q-space Imaging

To my mom

And Sophie

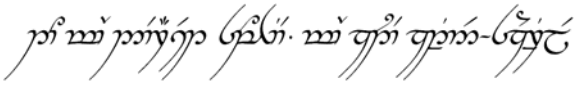

Acknowledgements

Felix W. Wehrli, Ph.D. (Advisor)

Xiaoping Tang, Ph.D.

Chih-Liang Chin, Ph.D.

Suzanne L. Wehrli, Ph.D.

Alexander C. Wright, Ph.D.

Scott N. Hwang, M.D. Ph.D.

Eric D. Schwartz, M.D.

Jeremy F. Magland, Ph.D.

Jiangsheng Yu, Ph.D.

Yusuf Bhagat, Ph.D.

Thesis Committee Members

Charles L. Epstein, Ph.D. (Chair)

Hee Kwon Song, Ph.D.

Ravinder Reddy, Ph.D.

Abstract

INDIRECT DETECTION OF AXONAL ARCHITECTURE WITH Q-SPACE IMAGING

Henry H. Ong

Advisor: Felix W. Wehrli, Ph.D.

Evaluating axon morphology would provide insights into connectivity, maturation, and disease pathology. Conventional diffusion MRI can provide metrics that are related to axon morphology, but cannot measure specific parameters such as mean axon diameter (MAD) and intracellular fraction (ICF). Q-space imaging (QSI) is an advanced diffusion MRI technique that may be able to provide more information on axon morphology. However, QSI has several limitations that affect its implementation and accuracy.

The main objective of this dissertation was to address these limitations and to evaluate the potential of QSI to accurately assess axon morphology. First, a custom-built high-amplitude gradient coil was used to address the limitations in the maximum gradient amplitude available with commercial systems. Second, to understand the relationship between axon morphology and QSI, simulations were used to investigate the effects of the presence of both extracellular and intracellular signals (ECS and ICS) as well as variation in cell size and shape. Third, three QSI-based methods were designed provide specific measures of axon morphology which have not been reported before.

The maximum amplitude of the custom gradient coil was 50 T/m that, for the first time, allowed for sub-micron displacement resolution while fulfilling the short gradient

approximation. This enabled near-ideal QSI experiments to be performed. QSI experiments on excised mouse spinal cords showed good correlation with histology, but overestimated MAD. Simulations showed that axon morphology was the dominant effect on QSI and suggested that the presence of ECS and ICS signals may complicate interpretation.

Three methods were designed to account for signal in ECS and ICS: two relied on a two-compartment model of the displacement probability density function and the echo attenuation at low q-values, and a third varied the gradient duration to differentiate diffusion in ECS from ICS. All three methods provided estimates of MAD and ICF that showed better agreement with histology than QSI. The methods were also evaluated implementation on a clinical scanner.

This dissertation demonstrated the sensitivity of QSI to axon morphology and showed the feasibility of three methods to accurately estimate MAD and ICF. Further investigation is warranted to study the future applications.

Table of contents

List of Tables

List of Figures

Chapter 1: Introduction

1.1 General background on neuro-physiology

The nervous system can be thought of as a network that allows an organism to interact with its environment. This network contains sensory components that sense environmental stimuli and motor components that control both voluntary and involuntary movement. The cells of the nervous system can be classified under two major categories: neurons and glia. Neurons are nerve cells that receive, conduct and transmit electric signals. Glia generally support neurons in various mechanical, metabolic, and phagocytic functions. Understanding the basic structure and function of neurons and glia will provide the necessary context for understanding the anatomy of the nervous system.

There are about 100 billion neurons in the nervous system in many different shapes and sizes. Nevertheless, all neurons share a basic structure: a cell body with two types of processes that extend from it. Like other cells, the cell body contains a nucleus and other structures related to metabolism and protein synthesis. The two processes can be divided into receiving processes (dendrites) or transmitting processes (axons). Dendrites are portions of the neuron which receive signals from other neurons. In general, a single neuron has many dendrites. The axon is the portion of the neuron where electric signals are transmitted to other neurons. Each neuron has only one axon which extends out from one neuron and contacts the dendrites of other neurons. Axons can vary greatly in length and diameter, which effects how efficiently the signals are conducted.

Axons can be thought of as cables conducting electrical activity. The efficiency of conducting a signal over distance, or conduction velocity, is an important physiologic property as it determines the speed at which information can be transmitted. In general,

the conduction velocity depends on the internal electric resistance of the axon; more specifically, higher resistance implies lower conduction velocity. Analogous to the resistance of a wire being inversely proportional to its cross-sectional area, increasing axon diameter lowers internal resistance. Therefore larger axons tend to have higher conduction velocities. Insulation is also an important determinant of conduction velocity. Insulation around wires prevents electric current from leaking out of the wire and into a surrounding conducting environment, as it is the case for axons, so that the current can propagate along the wire. The insulation for an axon is a lipoprotein sheath called myelin. Myelin wraps around axons and prevents electrical signals from leaking out of the axon. Myelinated axons therefore have much higher conduction velocities (~100 m/s) than unmyelinated axons (~5 m/s). Finally, it should be noted that while larger axon diameter does increase conduction velocity, there are anatomic limitations on axon size. Myelination therefore allows smaller axons to have higher conduction velocities.

1.1.1 Gross anatomy of the central nervous system

While essentially a continuum, based on gross anatomy, the nervous system can be divided into parts: the central nervous system (CNS) and peripheral nervous system (PNS). The CNS comprises of the brain and spinal cord, which contains the majority of neuronal cell bodies. The spinal cord is an extension of the brain and is connected to the brainstem at the base of the brain. The PNS comprises of mainly nerves, which are generally the axons of sensory and motor neurons, connecting the brain and spinal cord to other parts of the body.

Within the skull and spine, the brain and spinal cord are essentially floating in a fluid-filled sack. The sack is known as the meninges and is comprised of three membranes. The fluid is called cerebrospinal fluid (CSF). The major functions of CSF are to cushion the brain and spinal cord within their rigid bone enclosures and to maintain a suitable environment for neural tissue by providing an exit pathway into the blood stream for solutes, metabolites and proteins, mirroring the lymphatic system in the rest of the body.

Within the CNS, two tissue types can be visually identified especially with freshly excised tissue: white matter (WM) and gray matter (GM). WM and GM are connected at the cellular level and the distinction between the two is based on the structure of the neuron. WM consists primarily of axons which protrude from the cell bodies of neurons and allow for electric impulses to be conducted to and from other neurons. As discussed earlier, axons are generally surrounded by a myelin sheath, which has a white glistening color – this gives WM its white appearance. GM consists primarily of the cell bodies of neurons and therefore has a grayish color. In the brain, GM is concentrated on the surface, e.g. cerebral cortex, and in clusters below the surface called subcortical nuclei. The non-GM space is generally occupied by WM. In the spinal cord, the WM is found on the surface of the cord and surrounds a core of GM.

1.1.2 Spinal cord anatomy

External anatomy

The spinal cord resides within the spine, which is made up of many vertebrae separated by cartilaginous intervertebral discs. The vertebrae are numbered and divided

into four anatomical regions. Starting from the base of the skull, these regions are, in descending order, cervical, thoracic, lumbar, and sacral. Within each region, each vertebra can be labeled numerically, e.g. C5 or T8. The spinal cord can also be divided and numbered into similar segments. Most mammals such as rats, mice and pigs, which are used in the work presented here, have similar spine and spinal cord divisions (1).

Internal anatomy

The spinal cord, as mentioned previously, has WM on the outer surface of the cord, which surrounds a core of GM. Looking at a cross-section of spinal cord at the mid-cervical level, the core of GM has a butterfly- or H-shape (Figure 1.1). The spinal cord has bilateral symmetry, which means that the left side has the same anatomy as the right side. The GM can be divided into the dorsal and ventral horns as shown in Figure 1.1. The neurons in the dorsal and ventral horns have axons that project out of the cord. The dorsal and ventral horns can be further divided into sub-regions based on functional anatomy. The details are beyond the scope of this dissertation and can be found elsewhere (2-4).

The spinal cord WM can be divided up into three major areas called columns or funiculi (Figure 1.1). The dorsal column is located between the dorsal horns, the lateral column is located between the dorsal and ventral horns, and the ventral column is located between the ventral horns. In general, the spinal cord WM contains axons that run to and from the brain. Axons that have a common origin and convey similar information to a common destination can be grouped together into tracts or fasciculi. In the spinal cord, these tracts are well organized, but there is significant overlap and the boundaries are

somewhat arbitrary. There is a wide range of axon diameters from ≤ 1 μm to about 10 μm, although diameters of ≤ 3 μm predominate (4). Although detailed studies in human spinal cord are few, the data suggests that different WM tracts have different axon diameter distributions (4, 5). Most tracts are longitudinal, i.e. run along the spinal cord. However, there are a minority of tracts that are oblique, e.g. the tracts leading from the ventral horn to ventral root, which are not covered here. Longitudinal tracts can be divided into ascending and descending tracts. Ascending tracts transmit information to the brain, while descending tracts transmit information from the brain. WM tract organization and size will change along the length of the spinal cord as axon fibers leave and enter the cord. The following description of WM tracts focuses on the mid-cervical region as it is most relevant to the work in this dissertation.

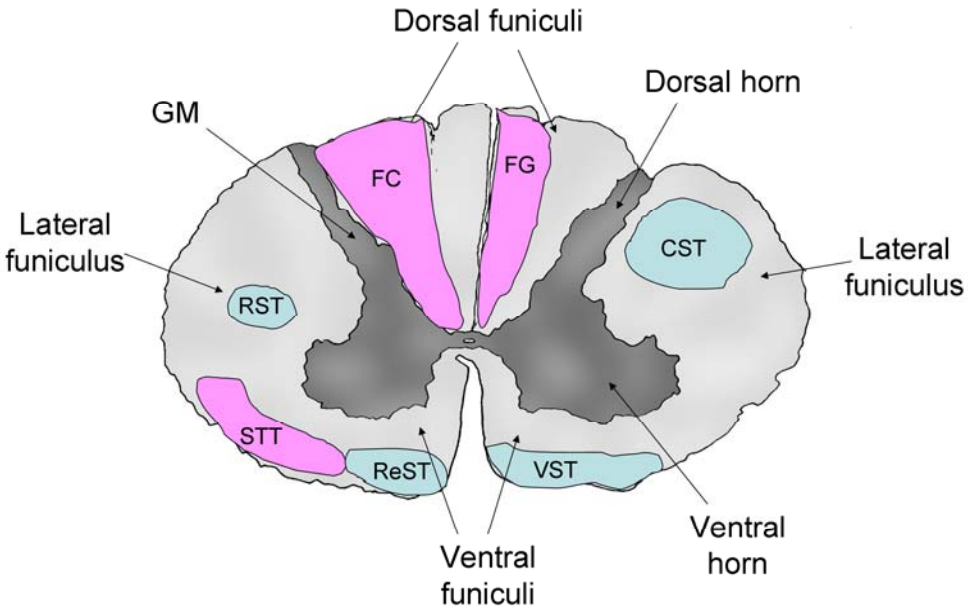

Figure 1.1. Schematic of mid-cervical human spinal cord cross-section showing internal anatomy. Also shown are approximate WM tract location: fasciculus gracilis (FG), fasciculus cuneatus (FC), corticospinal tract (CST), rubrospinal tract (RST), spinothalamic tract (STT), reticulospinal tract (ReST), and vestibulospinal tracts (VST). Pink tracts are ascending and blue tracts are descending.

While there are dozens of known WM tracts in the spinal cord, only the seven tracts that are studied here will be described. These tracts were chosen to represent a wide range of mean axon diameters (MAD) and diameter distributions. WM tracts are generally named after the nuclei in the brain where they originate or where they terminate. Figure 1.1 shows the approximate relative position of the WM tracts in the human spinal cord at the mid-cervical level. WM tract locations can be different in human (2, 4) and rat (6-11). Due to the similarities in anatomy between rats and mice, it is assumed that the WM tract locations and function are the same between the two species (1). The seven tracts are described below:

Fasciculus Gracilis (FG): An ascending tract that transmits sensory information on fine touch, proprioception or position sense, pressure and vibration. It begins in the caudal end of the spinal cord and terminates at the gracilis nucleus in the medulla oblongata of the brain stem. This tract generally transmits sensory information from the lower extremities. In both humans and rodents, the FG tract is located in the medial side of the dorsal column.

Fasciculus Cuneatus (FC): An ascending tract that transmits similar sensory information as the FG tract. It begins in the mid-thoracic level of the spinal cord and terminates at the cuneatus nucleus in the medulla oblongata of the brain stem. This tract generally transmits sensory information from the upper extremities. In both humans and rodents, the FC tract is located in the lateral side of the dorsal column next to the FG tract.

Corticospinal tract (CST): Also known as the pyramidal tract, the CST is a descending tract that transmits signals from the brain controlling skilled voluntary movement. Most of the axons in this tract originate from the motor cerebral cortex in the

brain. In humans, the CST can be found in the lateral and ventral columns. The lateral CST is found at all levels of the spinal cord while the ventral CST terminates at the mid-thoracic level. In the rat, however, the CST is found only in the anterior region of the dorsal column, which, given its proximity to the ascending FG and FC tracts, suggests that it may be part of that animal's sensory system (12). Interestingly, in the pig, where manual dexterity is non-existent, the CST is not evident in the spinal cord (13).

Rubrospinal tract (RST): Originating from red nucleus in the midbrain of the brain stem, the RST is a descending tract that that transmits signals facilitating flexor muscles and inhibiting extensor ones. It is generally found in the lateral column. It is well represented in lower mammals, but is less important in higher mammals where the CST is more developed. For example, in humans, the RST is small and only extends into the upper three cervical cord segments where it intermingles with the much larger lateral CST. In rats, however, the RST extends along the length of the spinal cord and is implicated in precise limb movements such as locomotion, reaching and grasping.

Spinothalamic tract (STT): This is an ascending tract which transmits sensory information relating to pain, temperature and light touch. The STT is present at all levels of the spinal cord and terminates at the thalamus. In humans and rats, this tract is generally located in the ventral and lateral columns and is intermingled with the reticulospinal tract (see below).

Reticulospinal tracts (ReST): The ReST is a collection of descending tracts that originate from the reticular formation, which is a collection of nuclei in the pons and medulla oblongata, and extends the length of the spinal cord. This tract transmits signals that adjust and regulate muscle reflexes during movement. This generally involves

changes in posture to maintain balance during a voluntary movement, e.g. raising one's arms, and the signal is transmitted via the CST. In humans and rats, the ReST is located in the ventral column and shifts laterally while descending the spinal cord.

Vestibulospinal tracts (VST): The VST is a collection of descending tracts that originate from the vestibular nuclei located at the junction between the pons and medulla oblongata. These nuclei are part of the vestibular system, which provides the sense of balance and body position information that allows for rapid compensatory movements in response to both self-induced and externally generated forces. Most of the tracts extend the length of the spinal cord, but one terminates at the mid-thoracic level. The tracts transmit signals that control antigravity muscles, i.e. muscles that continuously oppose gravity like the muscles that keep the lower jaw shut, and muscles that maintain balance and stabilize head and eye movements. In humans and rats, the VST is located in the ventral column.

1.1.3 White matter pathology

Axon morphology plays an important role for normal signal conduction. Damage to axon or myelin integrity will compromise signal transmission and can lead to a variety of symptoms. It is not the purpose to describe WM pathology in general here, but rather to provide a description of the common changes that occur to axon morphology under pathologic conditions. The hallmarks of WM pathology are axon loss and demyelination and their causes include various diseases and trauma.

Axon loss is the disappearance of axons. These axons may or may not reappear. The loss of axons leads to abnormal disconnections between neurons and will cause

interruptions in neural signaling. Demyelination is the partial or full loss of myelin surrounding an axon. As described above, myelin acts as an insulator to promote efficient signal conduction. Demyelination will therefore disrupt neural signaling as electric impulses may not travel as fast or as far along the same axon. Depending on the root cause, axon loss and demyelination may be localized within a lesion or occur diffusely throughout WM tissue.

Brief descriptions of how disease and trauma affects axon morphology are given below. The most common WM disease is multiple sclerosis (MS) which afflicts 2.5 million individuals world-wide (14). MS is an inflammatory disease in which the immune system attacks WM, leading to axon loss and demyelination. It is this WM damage that is the primary cause of clinical disability. Trauma can be any mechanical force applied to the CNS and can lead to tearing or even transection of axons (15). These injuries can cut-off nutrient transport within the axon, leading to degeneration of the axon distal to the injury site. This type of axon loss is known as Wallerian degeneration.

1.2 Histologic methods

Many details on neural architecture were given in the previous section and this knowledge comes primarily from histologic techniques. The developments in microscope design, tissue preparation and staining have allowed histology to become the standard technique to assess axonal architecture. The basic histologic protocol can be divided into three parts: tissue preparation, staining, and visualization. Full details on histologic methods can be found elsewhere (16) and a brief description will be given here.

Tissue preparation usually begins with fixation, which not only prevents tissue degradation over time, but also preserves microstructure during histologic processing. In order to cut very thin sections, the tissue must be embedded in a harder material such as paraffin wax. Once embedded, tissue sections can be cut and mounted onto a microscope slide. Tissues generally need to be stained in order to visualize structure. There are a multitude of possible stains and the list continues to grow. Silver staining is a classic method that has been used to visualize neurons in their entirety. There are also dyes that form bonds with certain chemical groups within tissue, e.g. toluidine blue stains myelin a shade of blue-purple. Then there are immunohistochemical stains that rely on antibodies binding to specific proteins. The antibodies can be labeled with a dye or a fluorescent molecule. Depending on the staining method, light, electron, or fluorescent microscopes can be used for visualization. Image processing techniques can then be used for quantitative analysis.

Histology is a powerful and flexible technique to investigate axonal architecture. There are limitations, however, such as the impossibility of performing histology *in vivo* due to its destructive methods. Furthermore, as histology relies on visualizing thin tissue sections, 3D axonal architecture information is difficult to obtain.

1.3 Magnetic resonance imaging

Magnetic resonance imaging (MRI) is a non-invasive imaging method widely used in medicine. Along with x-ray computed tomography (CT), it is the major imaging modality used in neuroimaging. An advantage MRI has is that it can describe an object in terms of many different properties such as relaxation, density, and diffusion, while CT

generally describes an object only in terms of its density. MRI's richness in information comes from the fact that its signal is sensitive to a variety of phenomena such as molecular motion and variation in the local magnetic fields. As it will be described in this work, MRI experiments can be designed to infer information on axon morphology. A full account of MRI theory is beyond the scope of this dissertation chapter and can be found elsewhere (17, 18). However, a brief description of how spatial position is encoded with magnetic field gradients is given below.

The MR signal arises from the intrinsic magnetic moment and spin of certain nuclei. The hydrogen atom is most commonly used in MRI due to its abundance in the human body. When a hydrogen nucleus is placed in a magnetic field, its nuclear spin will begin to precess with a frequency governed by

$$\omega = \gamma B_0 \tag{1.1}$$

where ω is the Larmor frequency, γ is the nucleus specific gyromagnetic ratio, and B_0 is the magnetic field strength. To encode for spatial information, a magnetic field gradient field is applied in addition to B_0 and the Larmor frequency then becomes spatially dependent. When the gradient is turned on and off, spins at different spatial locations will have accrued different phases. Therefore, the phase of a spin will represent its spatial location.

In conventional MRI, a variety of image contrasts between soft tissues can be obtained by changing the acquisition parameters. For example, an image can be generated in which the primary contrast is determined by spin density. After it has been excited by a radio frequency pulse the MRI signal decays over time. This decay, or relaxation, is characterized by two time constants: transverse relaxation (T_2) and longitudinal

relaxation (T_1). Again, images can be generated in which the primary contrast is determined by T_1 or T_2 values (T_1-weighted or T_2-weighted). This is useful as different tissues have different T_1 and T_2 values (e.g. GM T_1/T_2 = 950/100 ms, and WM T_1/T_2 = 600/80 ms (17)) and different images can be generated to highlight contrast between specific tissues. Furthermore, diseases such as cancer can change T_1 and T_2. Therefore relaxation contrasts can be used to emphasize tissue affected by pathology. The mechanisms for relaxation are intimately related to molecular motion (19) and T_1 and T_2 contrast can be used to gain insight into tissue architecture and pathology.

As a specific example, the role of MRI in the management and study of multiple sclerosis (MS) is discussed here. MRI aids in the diagnosis, monitoring of disease progression and treatment efficacy, and furthering the understanding of MS pathogenesis (14, 20-22). It can provide quantitative measures and is sensitive to subtle changes of the disease. Conventional MRI allows detection of MS lesions in neural tissue. These are typically hyperintense in proton density and T_2-weighted, and hypointense in T_1-weighted images. However, correlations between lesion appearance or volume and clinical disability are moderate at best. Most attribute this to heterogeneity of MS pathogenesis and the lack of conventional MRI specificity for MS pathology such as axon loss, demyelination, remyelination, edema, inflammation, gliosis, or Wallerian degeneration (23-26). Further, tissue that appears normal with conventional MRI contrasts (so-called normal appearing white matter (NAWM) or normal appearing gray matter (NAGW)), has been shown to exhibit abnormal biochemical composition and microarchitecture (14, 27). As a consequence, advanced MRI techniques, such as functional MRI (28), magnetic resonance spectroscopy (29, 30), magnetization transfer

imaging (31, 32), and diffusion MRI (33-35) have been used to study MS as these techniques have shown to reveal changes in biochemical content and microarchitecture in MS lesions as well as in NAWM and NAGM, and thus may lead to more robust clinical correlations (23-26).

1.3.1 Diffusion MRI

Due to the nature of nuclear spin precession, the spatial encoding which arises from the applied gradients can actually be removed by application of another gradient with opposite polarity. This process forms the basis of all diffusion MRI methods. Before discussing the technical aspects of diffusion MRI, a brief background based on Ref. (36) on molecular diffusion in biological tissues is given.

Diffusion concepts

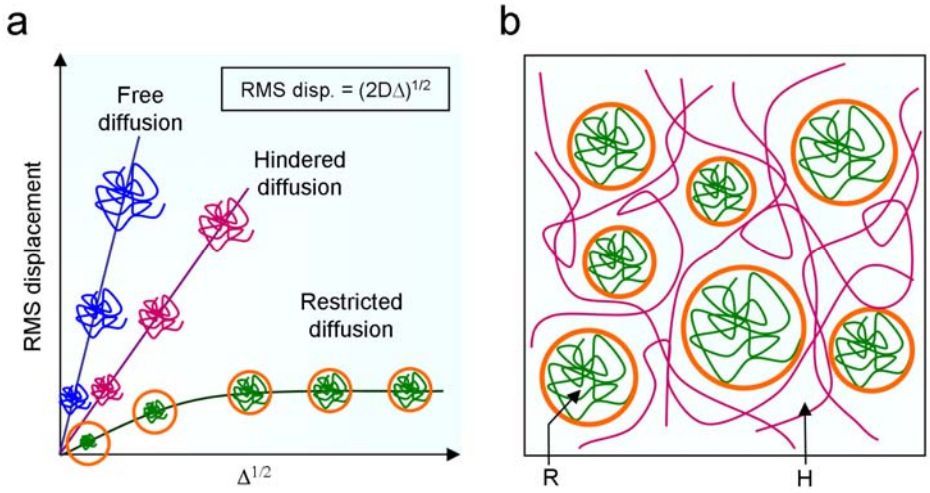

Figure 1.2. (a) In 1D, RMS displacement = 2DΔ, where Δ is the diffusion time and D is the diffusion coefficient. In free diffusion, RMS displacement increases linearly with the square root of Δ. For hindered diffusion, the RMS displacement still increases linearly with Δ, but the slope is lower. For restricted diffusion of molecules in a confined space, the RMS displacement will initially increase, but then be limited by the size of the confinement. (b) In biological tissues, different obstacles modulate the free diffusion process. Diffusing molecules can be restricted in closed spaces such as cells (R). Diffusing molecules may also be hindered by obstacles that impede motion (H).

Molecular diffusion, also known as Brownian motion, refers to the random translational motion of molecules that results from the thermal energy associated with these molecules. Albert Einstein, in his early work, developed a theoretical framework to characterize this physical process (37). In a medium without any barriers, during a specific time interval, random molecular displacements obey a 3-D Gaussian distribution with zero mean. The root-mean-squared (RMS) displacement is statistically well characterized by a diffusion coefficient (D). This coefficient depends only on the mass of the molecules, the temperature, and the viscosity of the medium in which the molecules are diffusing. For example, for 'free' water molecules diffusing in water at 37 °C, D is equal to 3×10^{-5} cm^2/s, which gives an average RMS displacement of 17 μm during a period of 50 ms (Figure 1.2a) – about 68% of the molecules will remain within a sphere of this diameter.

Diffusion MRI is particularly well suited at being sensitive to the RMS displacement of diffusing molecules. In effect, diffusing molecules are used to probe tissue structure at length scales well below the image resolution. During diffusion times of 50-100 ms, the RMS displacement of water molecules in brain tissues is about 1-15 μm. The diffusing water molecules bounce off, cross, or interact with many tissue components such as cell membranes, fibers and macromolecules (Figure 1.2b). As movement of molecules is impeded by such obstacles, the actual RMS displacement is reduced when compared with free water and the displacement distribution is no longer Gaussian. A new diffusion coefficient, the apparent diffusion coefficient (ADC), is defined to characterize these displacements. It is important to note that unlike the case of free diffusion, there are new diffusion phenomena that can be defined in systems with

barriers to diffusion like biological tissues. Water molecules confined in closed spaces, such as cells, experience restricted diffusion in that the molecules cannot displace farther than the confines of the cell (Figure 1.2a). Water molecules diffusing between cells may be "slowed down" due the impediments to motion they encounter. These molecules experience hindered diffusion, which has a reduced RMS displacement compared with free water, but does not have an upper limit in displacements as does restricted diffusion (Figure 1.2a). The non-invasive observation of water-diffusion driven RMS displacement distributions *in vivo* provides insights into the microstructure and geometric organization of neural tissues, as well as the changes in these features with varying physiological and pathological states.

Diffusion MRI applications

The fundamental diffusion MR experiment is the pulsed-field gradient spin-echo (PGSE) experiment (38) and consists of a 90°-180° spin-echo pulse sequence where a pair of gradient pulses is inserted before and after the 180° RF pulse (Figure 1.3). The first gradient pulse encodes for spatial information and the second gradient pulse will remove this spatial encoding by reversing the accrued phase. If there were no diffusion, spins would not change spatial location between the two gradient pulses and the spatial encoding reversal would be complete, i.e. there will be no residual phase. However, if there were diffusion, spins would change spatial location between the two gradient pulses. Therefore, the second gradient pulse would not completely remove the spatial encoding imparted by the first gradient pulse and there would be residual phase. It is this residual phase that contains information on the displacements due to diffusion.

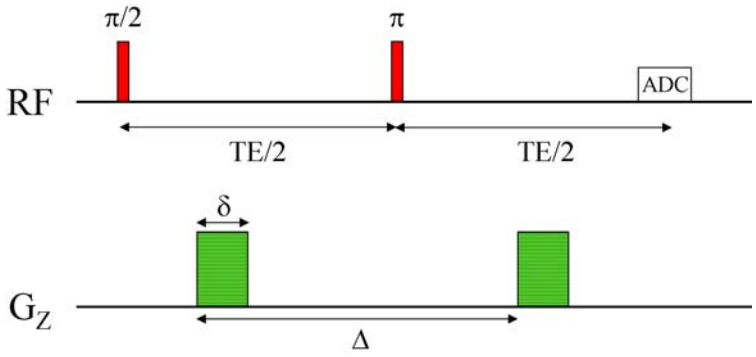

Figure 1.3. Schematic of a pulse-gradient spin-echo (PGSE) diffusion encoding sequence. Only diffusion gradients along the z-axis are shown. ADC is the analog-to-digital converter. TE is echo time. Δ is the time between diffusion gradients and δ is the gradient duration.

Diffusion MRI is sensitive to the architecture of neural tissues as the diffusion of water molecules is hindered by axon membranes, myelin, and intracellular and extracellular organelles (39). While it is believed that axon membranes provide the primary barrier to diffusion, there is evidence to suggest that myelin also modulates the ability for water to diffuse between the intracellular and extracellular spaces (39, 40). Structural changes due to pathology will affect how far and in what direction molecules diffuse. Therefore, diffusion MRI, which is sensitive to the average molecular displacement within an image voxel, has been used to study changes in axonal architecture due to pathology (33-35). The ability to assess regional axonal architecture has applications ranging from studying brain connectivity and maturation, to the study of WM diseases such as MS

Diffusion weighted imaging (DWI) and diffusion tensor imaging (DTI) are the most common diffusion MRI techniques employed and are used to calculate ADC and mean diffusivity/fractional anisotropy (MD/FA), respectively. DWI and DTI provide a non-invasive means to provide indirect estimates of WM tract orientation and axon

integrity without explicitly resolving the structures (34, 36). The main difference between DWI and DTI is that DTI measures the orientation dependence of diffusion. It is important to note that both DWI and DTI fundamentally assume that the underlying diffuse is anisotropic free water diffusion, i.e. no barriers to water motion. Clearly, this notion is incorrect in biologic tissues.

DWI has been used to investigate regional axon architecture. Schwartz *et al*. (9, 10) performed *ex vivo* DWI of normal adult rat cervical spinal cords and computed transverse ADC (tADC) maps and longitudinal ADC (lADC) maps, i.e. ADC perpendicular and parallel to the WM tract. The authors compared tADC and lADC values to parameters such as axon diameter, and extra-cellular and intra-cellular space (ECS and ICS, respectively) fractions derived from histology of the same WM tracts. Interestingly, no correlation was found between tADC and axon diameter. However, a positive correlation was found between tADC with ECS fraction and axon spacing and a negative correlation was also found between axon count and myelin volume fraction. Such correlations are indicative of extra-cellular water mobility as the primary determinant of tADC, which is in agreement with the conjecture that signal attenuation at low diffusion encoding values (low b-values) is dominated by ECS water diffusion (41). Therefore, DWI and DTI may not provide direct information on ICS water diffusion.

While DWI and DTI are both valuable clinical tools, neither has been demonstrated to provide specific information on axonal architecture such as MAD or ECS and ICS volume fractions, which could potentially provide insight into brain maturation or pathology. Such limitations may arise from the simplistic approach of DWI and the erroneous assumption of free diffusion, i.e. absence of barriers to molecular

diffusion, in the analysis of DTI. Furthermore, DWI and DTI may be limited by only being sensitive to ECS water diffusion. These limitations suggest the need for different diffusion MRI techniques.

1.4 Q-space imaging

An alternative diffusion MRI technique used in this dissertation, q-space imaging (QSI), as proposed by Callaghan (42, 43) and by Cory & Garroway (44), does not assume any model of diffusion. As such, QSI more accurately describes water diffusion in biological tissues and has the potential to provide information on axonal architecture not amenable by conventional diffusion MRI techniques.

QSI allows assessment of microarchitecture by exploiting the regularity of restrictions to molecular diffusion in porous systems as applied to determine pore geometry in porous solids (45), the study of packed erythrocytes (46), and the assessment of axonal architecture (47-49). In WM tracts, the porous system consists of water diffusion restricted by axon membranes and myelin sheaths (39). The application of QSI to assess axonal architecture, where one extracts information such as MAD, should not be confused with the application of QSI to estimate axon fiber orientation in tractography, as used in techniques such as diffusion spectrum imaging (DSI) and q-ball imaging (QBI) (50, 51) in which multiple fiber orientations within a single voxel can be differentiated, in contrast to DTI.

As it will be discussed later, current QSI applications to study WM have several limitations that hinder its ability to accurately assess axonal architecture. If its limitations can be overcome, QSI may potentially provide valuable axonal architecture information that may aid in the assessment and treatment of WM diseases and injury. Before the

limitation of QSI can be properly described, a summary of its underlying theory is given below.

1.4.1 Theory

The q-space experiment uses a pulsed-gradient sequence, such as PGSE (Figure 1.3), with two diffusion-sensitizing gradients of amplitude G and duration δ, which are separated by a diffusion time Δ. For simplicity we assume the diffusion gradients along a single direction, arbitrarily labeled x. Typically, one measures the signal echo maximum while stepping the amplitude of the diffusion-sensitizing gradients. As a result of molecular diffusion, the echo maximum will decrease with increasing gradient amplitude and the function describing the evolution of the signal referred to as "echo attenuation." In highly regular porous structures, the echo attenuation will exhibit maxima and minima and information about pore geometry can be directly read from these diffraction patterns (45).

For the following derivation to hold true, molecular diffusion must be minimal during the diffusion-sensitizing gradient pulses (short gradient pulse (SGP) approximation where $\delta << \Delta$). Given the conditional probability, $P(\mathbf{x} \mid \mathbf{x}', \Delta)$, that a molecule starting at location x is displaced to position x' during the period Δ, the normalized echo attenuation is given as:

$$E(\mathbf{G}_x, \Delta) = \iint \rho(\mathbf{x}) P(\mathbf{x} \mid \mathbf{x}', \Delta) \exp\left[i\gamma\delta\mathbf{G}_x \cdot (\mathbf{x} - \mathbf{x}')\right] d\mathbf{x} d\mathbf{x}' \qquad (1.2)$$

where $\rho(\mathbf{x})$ is the spin density at the starting location and G_x is the amplitude of the diffusion gradients. The argument $\gamma\delta\mathbf{G}_x \cdot (\mathbf{x} - \mathbf{x}')$ is thus the phase the spins accrue at the

end of their displacement. Eq. 1.2 can be simplified into a more useful form by defining a displacement probability density function (PDF) $P(\mathsf{R},\Delta) = \int \rho(\mathsf{x})P(\mathsf{x}\,|\,\mathsf{x}+\mathsf{R},\Delta)d\mathsf{x}$, which expresses the probability that a molecule at *any* initial position is displaced along the gradient direction by $\mathsf{R} = \mathsf{x}' - \mathsf{x}$ during the period Δ. Consequently, Eq. 1.2 reduces to

$$E(\mathsf{q},\Delta) = \int P(\mathsf{R},\Delta)\exp[i2\pi\mathsf{q}\cdot\mathsf{R}]d\mathsf{R} \qquad (1.3)$$

where $\mathsf{q} = (2\pi)^{-1}\gamma\delta\mathsf{G}_x$ is the q-value with dimensions of inverse length units. It follows from Eq. 1.3 that the inverse FT of the echo attenuation with respect to q returns the displacement PDF. For the free diffusion case, it is known that the displacement PDF is a Gaussian (42).

In the case of molecules contained within a pore, diffusion leads to collisions with the pore wall; therefore the displacement PDF will reflect properties characteristic of the pore geometry. For example, consider a fluid constrained to a pore with a perfectly reflecting wall. Under conditions that $\Delta >> a^2/2D$ where a is the characteristic pore dimension, most molecules will have collided with the wall during Δ. Assuming constant molecular density, the conditional probabilities become independent of initial position so that $P(\mathsf{x}\,|\,\mathsf{x}',\Delta)$ approaches $\rho(\mathsf{x}')$, or $\rho(\mathsf{x}+\mathsf{R})$, the pore molecular density function. Consequently, the displacement PDF becomes the autocorrelation function of the molecular density

$$P(\mathsf{R},\Delta\to\infty) = \int \rho(\mathsf{x}+\mathsf{R})\rho(\mathsf{x})d\mathsf{x} \qquad (1.4)$$

from which pore geometry information can be extracted. Since the displacement PDF does not represent a single pore, only an average displacement probability from all pores within the imaging volume (typically a voxel) can be obtained in this manner.

As an illustrative example, a 1-D pore of rectangular molecular density function, e.g. fluid constrained to the space between parallel planes, would yield a triangular displacement profile, as a triangle function is the autocorrelation of a *rect* function. Notably, the full-width at half-maximum (FWHM) of the triangle profile function is precisely equal to the width of the *rect* function. Finally, the FT of the triangular displacement profile – the echo attenuation $E(\mathbf{q})$ – would be a $|sinc|^2$ function.

The displacement PDF will be influenced by axonal architecture as axon membranes and myelin sheaths impede the motion of diffusing molecules such as water and hence affect its displacement probabilities, e.g. higher probability of displacement parallel as opposed to displacement perpendicular to WM fiber tracts. The displacement PDF has a particularly simple interpretation as long as the gradients are applied perpendicular to the axon fibers, which can be thought of as having a tubular geometry (52). The width of the displacement PDF, typically characterized by its FWHM, should correlate with the scale of restrictions which, in WM, is the mean axon diameter averaged over the imaging volume. Therefore, it is possible to estimate mean axon diameter as the FWHM. Other metrics that are used to characterize the displacement PDF include the peak value, otherwise known as the zero-displacement probability (ZDP), which is inversely related to FWHM and reflects the fraction of molecules that diffuse short distance or not at all, and kurtosis, i.e. the fourth moment of the displacement PDF, which is a measure of the degree of deviation from a Gaussian distribution and therefore reflects the degree of restriction to diffusion (48). Kurtosis may correlate with axon density and may provide insight to long-range diffusion behavior (53).

It is important to note that the displacement PDF is an empirical measurement, i.e. we are simply observing the average molecular displacement within an imaging volume. In order to interpret the features of the displacement PDF, one must compare it with the underlying tissue structure as seen with histology in order to understand how the structures impede water diffusion. Q-space simulations, on both simple circular axon models and histologic images, provide valuable insight into the effect of tissue structure on the displacement profile. In particular, axon models allow for the investigation of specific structure effects, like axonal degeneration or demyelination. With this knowledge, one can link structural attributes to displacement profile features.

1.4.2 QSI of neural tissue

QSI has been successfully applied to study mice, rats, and swine both *in vivo* and *ex vivo*. King *et al.* (54, 55) first used QSI to study ischemia in mouse brains. They found that the proportion of molecules displacing less than 10 μm increased in mouse brain post mortem and *in vivo* upon surgical interruption of blood supply to the forebrain, which mirrors the reduced ADC observed in brain ischemia. Assaf *et al.* (40, 47) used QSI to study spinal cord maturation in rats and found the mean displacement (defined as FWHM of the displacement PDF) in WM steadily increased toward maturation, unlike in GM, which remained constant throughout the development stages. Furthermore, Biton *et al.* used QSI to study excised spinal cords from swine model of MS, and reported increased water displacement in both lesions and normal appearing WM, parameters that correlated with histology (56).

In order to study the tortuous WM tracts of the brain, Assaf *et al.* (57) incorporated a tensor analysis into QSI to produce rotationally invariant parameters analogous to DTI. Importantly, the tensor analysis allows for extraction of the displacement PDF corresponding to water diffusing perpendicular to WM tracts. Avram *et al.* (52) demonstrated experimentally that to extract accurate diameters from a cylindrical pore phantom, the diffusion gradients had to be applied orthogonally, or nearly so, to the long axis of the cylinders.

In brief, a tensor analysis can be applied whenever a set of measured parameters can be modeled as being proportional to a tensor. Basser *et al.* (58) showed that it was possible to extract the tensor elements from a linear combination of the experimental measurements through a system of equations. Intuitively, the displacement PDF will depend on the diffusion gradient direction due to the anisotropic diffusion arising from tissue microarchitecture. Consequently, one can solve for the displacement PDF tensor elements from a linear combination of measured displacement PDFs with different diffusion gradient directions. In this way, one can calculate parameters like the displacement profile FWHM and ZDP, or any other parameter characterizing the displacement PDF, of molecules displacing perpendicular or parallel to the WM tract orientation.

Assaf *et al.* (57) used this tensor analysis to study MS patients. They observed increased water displacement in MS plaques and normal appearing WM, reflecting loss of axonal architecture integrity. These changes were more pronounced than the changes in conventional DTI metrics. The same group also showed that q-space displacement

parameters in MS patients correlated with lowered N-acetylaspartate levels as measured with MR spectroscopy, which suggests sensitivity of QSI to axonal damage (59).

In 2007, Nilsson *et al*. (60) investigated the accuracy of such a tensor analysis in QSI by observing the molecules displacing perpendicular and parallel to the WM tract in human brain *in vivo*, via the FWHM of the displacement PDF, as a function of diffusion time. Nilsson *et al.* observed that the perpendicular FWHM remained constant while the parallel FWHM increased linearly with the square root of diffusion time, indicating restricted and hindered diffusion, respectively, as expected. Nordh *et al*. (61) investigated the effects of not fulfilling the SGP approximation on the tensor analysis in QSI by observing the perpendicular and parallel FWHMs in human brain *in vivo.* The perpendicular FWHM deceased only slightly while the parallel FWHM decreased more markedly when not fulfilling the SGP approximation, also confirming previous observations. Recently, QSI has also been applied to image *in vivo* human spinal cord by Farrell *et al.* (62). In this case, due to the simple WM structure, no tensor analysis was necessary and the diffusion gradients were applied orthogonally to the spinal cord. Farrell found that the displacement PDF FWHM and zero-displacement probability correlated well with lesions observed with conventional MRI.

1.4.3 Limitations of current QSI methods

Despite the numerous studies mentioned above that demonstrate QSI is sensitive to neural tissue microstructure, those studies suffered from limitations that impair accurate assessment of axonal architecture. These limitations may have obscured any specific information on axonal architecture QSI could have provided.

The first major limitation is the maximum gradient amplitude available on the commercial systems is insufficient for the displacement PDF resolution needed to study cellular length scales. The displacement PDF resolution is determined by the maximum q-value used due to its Fourier relationship with the echo attenuation. Imposition of the SGP approximation demands very high gradient amplitudes not commercially available even on micro-imaging systems. As a result, the QSI studies cited above either violated the SGP approximation or their displacement PDF resolutions (ranging from 2 (48) to 20 (54) μm) exceeded typical axon diameters (1-2 μm). Mitra *et al.* (63) predicted that as the gradient duration increased in relation to diffusion time, the displacement profile would artifactually narrow, which has been observed experimentally (57).

The second major limitation is that QSI of biological tissues is complicated by the presence of water in ECS and ICS and exchange of molecules between these compartments. Due to the lack of precise knowledge of parameters such as ECS and ICS T_2 and membrane permeability, the consequences of these effects are poorly understood. The measured displacement PDF reflects displacements due to molecular diffusion in both compartments. Diffusion in the ECS and ICS is hypothesized to be hindered and restricted (41), respectively. As a result, the displacement PDF may be broader than the actual MAD due to the addition of displacements resulting from hindered diffusion in the ECS. Furthermore, variations in cell shape and size complicates QSI experiments. While it is generally accepted that echo attenuation diffraction peaks are not usually observed in biological tissues due to heterogeneity in cell shape and size variation, it is not well understood how these variations affect the displacement PDF.

The third major limitation is that, up until now, MAD is the only specific measurement of axonal architecture cited in previous QSI studies of WM. An estimate of MAD by itself offers limited insight into axonal architecture. If it were coupled with information on ECS and ICS volume fractions, new information could be inferred such as an estimate of axon loss, which would affect the ECS and ICS volume fractions, and demyelination, which would increase the FWHM of the displacement PDF. Both of these changes in axonal architecture are hallmarks of spinal cord injury and a variety of WM diseases from multiple sclerosis to Alzheimer's disease (10, 34, 64).

1.4.4 Addressing the limitations of QSI

The main objective of this dissertation is to address the current limitations of QSI mentioned in the previous section and to evaluate its capacity to accurately assess axonal architecture *in vivo*. While there is overlap between the different approaches taken in the work presented here, the research strategy employed in this dissertation to address the limitations can be divided into three parts.

First, a custom built high amplitude gradient coil was used to address the limitations in the maximum gradient amplitude achievable with commercial systems. The high gradient amplitude available with this coil allows QSI to be performed under more ideal experimental conditions: the SGP approximation is fulfilled and the displacement PDF resolution is sufficient to study displacements on the cellular length scale. With the ability to perform an ideal QSI experiment, a proper comparison can be made with non-ideal QSI experiments. Both the SGP approximation and the displacement PDF

resolution are systematically varied to mimic experimental conditions using commercial systems and effects on QSI can be experimentally observed.

Second, QSI simulations are used to investigate the effects of the presence of both ECS and ICS signals on QSI. By using simulations, parameters such as the T_2s and concentrations of the ECS and ICS as well as membrane permeability can be explicitly defined. There is a lack of precise knowledge of these parameters and systematically varying them in simulations provides insight into their effects on QSI. In addition, simulations are also used to further understanding on the effects of axonal architecture on QSI-derived measurements by varying axon size and shape distribution.

Third, three QSI-based methods designed to account for ECS and ICS signals and to extract different axonal architecture metrics are evaluated for accuracy and potential application *in vivo*. The first method, described in Chapter 4, referred to as the "displacement PDF method", employs a two-compartment model of the displacement PDF to account for signal from ECS and ICS. The second method, described in Chapter 5, referred to as the "low q-value method", extracts axonal architecture information by fitting the echo attenuation at low q-values, which obviates the need for high-gradient amplitudes. The third method, described in Chapter 6, referred to as the "varying gradient pulse duration (VGPD) method", empirically separates ECS and ICS signals from which MAD and ICS volume fraction can be estimated

1.5 Outline of thesis chapters

The main objective of this thesis was to address the current limitations of QSI and to evaluate capacity of the above mentioned methods to accurately assess axonal architecture *in vivo*.

In Chapter 2, all common materials and methods used throughout this thesis are described. This includes a description of the custom-built gradient coil, animal specimen preparation, QSI acquisition parameters, and histologic methods and results.

In Chapter 3, QSI simulations on both synthetic axons and histologic images are used to investigate the effects of signal from both ECS and ICS and variability of cell size and shape on QSI measurements of axonal architecture. The simulation results show that despite all the variable and unknown effects, QSI may still provide accurate measures of axon morphology. The insights from these results support the potential of QSI to indirectly assess axonal architecture and aids in the understanding and interpretation of the experimental results to be discussed in the following chapters.

In Chapter 4, one- and two-compartment displacement PDF methods are described and used to assess MAD, ICS volume fraction, and axon diameter distribution in mouse spinal cords. The results show that the two-compartment displacement PDF method, which accounts for ECS and ICS signals, can accurately estimate MAD, ICS volume fraction, and axon diameter distribution as compared with histology. However, the accuracy is dependent on fulfilling the SGP approximation.

In Chapter 5, one- and two-compartment low q-value methods are described and used to assess MAD and ICS volume fraction in mouse spinal cords. The major advantage of these methods is that they do not require high gradient strengths. The results

show that while MAD is accurately measured, the ICS volume fraction is over estimated. Under conditions violating the SGP approximation, the low q-value method still accurately measures MAD, which supports the potential for this method to be implemented on a clinical scanner.

In Chapter 6, the VGPD method is described. This method allows for empirical separation of ECS and ICS signal from which MAD and ICS volume fraction can be estimated. QSI subvoxel processing is used to correct for insufficient displacement resolution inherent in the method. The results show that MAD and ICS volume fraction are accurately measured compared with histology. However, the accuracy is again dependent on fulfilling the SGP approximation.

In Chapter 7, all three methods described above are implemented on a clinical scanner to investigate the feasibility of implementation on a clinical scanner. Excised pig spinal cords were used. The major limitation on a clinical scanner is the low gradient strengths available. This severely hampers the accuracy of MAD estimates with the displacement PDF and VGPD methods. The two-compartment low q-value method seemed to provide estimates of MAD close to expected values. Unfortunately, histology was not available for validation.

The q-space simulations were carried out with a previously developed finite-difference computer program (65). A previously built custom gradient coil was used here for QSI experiments (66). The displacement PDF and low q-value methods have already been published (67, 68). The VGPD method is an extension of the ICF method described in (67). Preliminary data has also been published in abstract form (69-74).

1.6 Literature citations

1. Watson, C., G. Paxinos, and G. Kayalioglu, eds. *The spinal cord: a Christopher and Dana Reeve Foundation text and atlas*. 2009, Elsevier Academic Press: San Diego.
2. Cramer, G.D. and S.A. Darby, *Basic and clinical anatomy of the spine, spinal cord, and ANS*. 2005, St. Louis, MI: Elsevier.
3. Heimer, L., *The human brain and spinal cord: functional neuroanatomy and dissection guide*. 2nd ed. 1995, New York: Springer-Verlag.
4. Williams, P.L., et al., eds. *Gray's anatomy: the anatomical basis of medicine and surgery*. 38th ed. 1995, Churchill Livingstone: New York, NY.
5. Makino, M., et al., *Morphometric study of myelinated fibers in human cervical spinal cord white matter.* Spine (Phila Pa 1976), 1996. **21**(9): p. 1010-6.
6. Grant, G. and H.R. Koerber, *Spinal Cord Cytoarchitecture*, in *The Rat Nervous System*, G. Paxinos, Editor. 2004, Elsevier Academic Press: Amsterdam. p. 121-128.
7. Kuchler, M., et al., *Red nucleus projections to distinct motor neuron pools in the rat spinal cord.* J Comp Neurol, 2002. **448**(4): p. 349-59.
8. Raineteau, O., et al., *Reorganization of descending motor tracts in the rat spinal cord.* Eur J Neurosci, 2002. **16**(9): p. 1761-71.
9. Schwartz, E.D., et al., *Ex vivo evaluation of ADC values within spinal cord white matter tracts.* AJNR Am J Neuroradiol, 2005. **26**(2): p. 390-7.
10. Schwartz, E.D., et al., *MRI diffusion coefficients in spinal cord correlate with axon morphometry.* Neuroreport, 2005. **16**(1): p. 73-6.

11. Tracey, D., *Ascending and Descending Pathways in the Spinal Cord*, in *The Rat Nervous System*, G. Paxinos, Editor. 2004, Elsevier Academic Press: Amsterdam. p. 149-164.

12. Miyabayashi, T. and T. Shirai, *Synaptic formations of the corticospinal tract in the rat spinal cord.* Okajimas Folia Anat Jpn, 1988. **65**(2-3): p. 117-39.

13. Palmieri, G., et al., *Course and termination of the pyramidal tract in the pig.* Arch Anat Microsc Morphol Exp, 1986. **75**(3): p. 167-76.

14. Compston, A., *McAlpine's Multiple Sclerosis*. 2006, Churchill Livingstone Elsevier. p. Chapters 2,6,7,11,12,13.

15. Blumbergs, P., P. Reilly, and R. Vink, *Trauma*, in *Greenfield's Neuropathology*, S. Love, D.N. Louis, and D.W. Ellison, Editors. 2008, Edward Arnold Ltd: London. p. 733-833.

16. Kiernan, J.A., *Histological and Histochemical Method: Theory and Practice*. 2008, Bloxham: Scion Publishing Ltd.

17. Haacke, E.M., *Magnetic resonance imaging : physical principles and sequence design*. 1999, New York: Wiley. xxvii, 914 p.

18. Liang, Z.-P., P.C. Lauterbur, and IEEE Engineering in Medicine and Biology Society., *Principles of magnetic resonance imaging : a signal processing perspective*. IEEE Press series in biomedical engineering. 2000, Bellingham, Wash. New York: SPIE Optical Engineering Press ; IEEE Press. xv, 416 p.

19. Farrar, T.C. and E.D. Becker, *Pulse and Fourier transform NMR introduction to theory and methods*. 1971, New York,: Academic Press. xiv, 115 p.

20. Filippi, M., C. Tortorella, and M. Rovaris, *Magnetic resonance imaging of multiple sclerosis.* J Neuroimaging, 2002. **12**(4): p. 289-301.

21. Filippi, M. and M.A. Rocca, *The use of modern magnetic resonance techniques to monitor disease evolution in multiple sclerosis.* Adv Neurol, 2006. **98**: p. 167-83.

22. Bakshi, R., et al., *Imaging of multiple sclerosis: role in neurotherapeutics.* NeuroRx, 2005. **2**(2): p. 277-303.

23. Inglese, M., B. Benedetti, and M. Filippi, *The relation between MRI measures of inflammation and neurodegeneration in multiple sclerosis.* J Neurol Sci, 2005. **233**(1-2): p. 15-9.

24. Zivadinov, R. and T.P. Leist, *Clinical-magnetic resonance imaging correlations in multiple sclerosis.* J Neuroimaging, 2005. **15**(4 Suppl): p. 10S-21S.

25. Wayne Moore, G.R., *MRI-clinical correlations: more than inflammation alone-what can MRI contribute to improve the understanding of pathological processes in MS?* J Neurol Sci, 2003. **206**(2): p. 175-9.

26. Goodin, D.S., *Magnetic resonance imaging as a surrogate outcome measure of disability in multiple sclerosis: have we been overly harsh in our assessment?* Ann Neurol, 2006. **59**(4): p. 597-605.

27. Filippi, M. and M.A. Rocca, *MRI evidence for multiple sclerosis as a diffuse disease of the central nervous system.* J Neurol, 2005. **252 Suppl 5**: p. v16-24.

28. Buckle, G.J., *Functional magnetic resonance imaging and multiple sclerosis: the evidence for neuronal plasticity.* J Neuroimaging, 2005. **15**(4 Suppl): p. 82S-93S.

29. Narayana, P.A., *Magnetic resonance spectroscopy in the monitoring of multiple sclerosis.* J Neuroimaging, 2005. **15**(4 Suppl): p. 46S-57S.

30. Filippi, M., et al., *Magnetic resonance techniques for the in vivo assessment of multiple sclerosis pathology: consensus report of the white matter study group.* J Magn Reson Imaging, 2005. **21**(6): p. 669-75.

31. Filippi, M., *Magnetization transfer MRI in multiple sclerosis and other central nervous system disorders.* Eur J Neurol, 2003. **10**(1): p. 3-10.

32. Horsfield, M.A., *Magnetization transfer imaging in multiple sclerosis.* J Neuroimaging, 2005. **15**(4 Suppl): p. 58S-67S.

33. Rovaris, M., et al., *Diffusion MRI in multiple sclerosis.* Neurology, 2005. **65**(10): p. 1526-32.

34. Horsfield, M.A. and D.K. Jones, *Applications of diffusion-weighted and diffusion tensor MRI to white matter diseases - a review.* NMR Biomed, 2002. **15**(7-8): p. 570-7.

35. Goldberg-Zimring, D., et al., *Diffusion tensor magnetic resonance imaging in multiple sclerosis.* J Neuroimaging, 2005. **15**(4 Suppl): p. 68S-81S.

36. Le Bihan, D., *Looking into the functional architecture of the brain with diffusion MRI.* Nat Rev Neurosci, 2003. **4**(6): p. 469-80.

37. Einstein, A., R. Fürth, and A.D. Cowper, *Investigations on the theory of the Brownian movement*. 1956, [New York]: Dover Publications. 119 p.

38. Stejskal, E.O. and J.E. Tanner, *Spin Diffusion Measurements: Spin Echoes in the Presence of a Time-Dependent Field Gradient.* J Chem Phys, 1965. **42**(1): p. 288-292.

39. Beaulieu, C., *The basis of anisotropic water diffusion in the nervous system - a technical review.* NMR Biomed, 2002. **15**(7-8): p. 435-55.

40. Assaf, Y., A. Mayk, and Y. Cohen, *Displacement imaging of spinal cord using q-space diffusion-weighted MRI.* Magn Reson Med, 2000. **44**(5): p. 713-22.

41. Assaf, Y., et al., *New modeling and experimental framework to characterize hindered and restricted water diffusion in brain white matter.* Magn Reson Med, 2004. **52**(5): p. 965-78.

42. Callaghan, P., *Principles of Nuclear Magnetic Resonance Microscopy*. 1993, New York: Oxford University Press.

43. Callaghan, P.T., *NMR imaging, NMR diffraction and applications of pulsed gradient spin echoes in porous media.* Magn Reson Imaging, 1996. **14**(7-8): p. 701-9.

44. Cory, D.G. and A.N. Garroway, *Measurement of translational displacement probabilities by NMR: an indicator of compartmentation.* Magn Reson Med, 1990. **14**(3): p. 435-44.

45. Callaghan, P.T., et al., *Diffraction-like effects in NMR diffusion studies of fluids in porous solids.* Nature, 1991. **351**: p. 467-469.

46. Torres, A.M., et al., *Characterisation of erythrocyte shapes and sizes by NMR diffusion-diffraction of water: correlations with electron micrographs.* Magn Reson Imaging, 1998. **16**(4): p. 423-34.

47. Cohen, Y. and Y. Assaf, *High b-value q-space analyzed diffusion-weighted MRS and MRI in neuronal tissues - a technical review.* NMR Biomed, 2002. **15**(7-8): p. 516-42.

48. Chin, C.L., et al., *Assessment of axonal fiber tract architecture in excised rat spinal cord by localized NMR q-space imaging: simulations and experimental studies.* Magn Reson Med, 2004. **52**(4): p. 733-40.

49. Malmborg, C., et al., *Mapping the intracellular fraction of water by varying the gradient pulse length in q-space diffusion MRI.* J Magn Reson, 2006. **180**(2): p. 280-5.

50. Wedeen, V.J., et al., *Mapping complex tissue architecture with diffusion spectrum magnetic resonance imaging.* Magn Reson Med, 2005. **54**(6): p. 1377-86.

51. Tuch, D.S., et al., *Diffusion MRI of complex neural architecture.* Neuron, 2003. **40**(5): p. 885-95.

52. Avram, L., Y. Assaf, and Y. Cohen, *The effect of rotational angle and experimental parameters on the diffraction patterns and micro-structural information obtained from q-space diffusion NMR: implication for diffusion in white matter fibers.* J Magn Reson, 2004. **169**(1): p. 30-8.

53. Jensen, J.H., et al., *Diffusional kurtosis imaging: the quantification of non-gaussian water diffusion by means of magnetic resonance imaging.* Magn Reson Med, 2005. **53**(6): p. 1432-40.

54. King, M.D., et al., *Localized q-space imaging of the mouse brain.* Magn Reson Med, 1997. **38**(6): p. 930-7.

55. King, M.D., et al., *q-Space imaging of the brain.* Magn Reson Med, 1994. **32**(6): p. 707-13.

56. Biton, I.E., et al., *Improved detectability of experimental allergic encephalomyelitis in excised swine spinal cords by high b-value q-space DWI.* Exp Neurol, 2005. **195**(2): p. 437-46.

57. Assaf, Y., et al., *High b-value q-space analyzed diffusion-weighted MRI: application to multiple sclerosis.* Magn Reson Med, 2002. **47**(1): p. 115-26.

58. Basser, P.J. and C. Pierpaoli, *A simplified method to measure the diffusion tensor from seven MR images.* Magn Reson Med, 1998. **39**(6): p. 928-34.

59. Assaf, Y., et al., *White matter changes in multiple sclerosis: correlation of q-space diffusion MRI and 1H MRS.* Magn Reson Imaging, 2005. **23**(6): p. 703-10.

60. Nilsson, M., et al. *Dynamic Displacement in Human Brain Studied Using Q-Space Diffusion MRI at a 3T Clinical Scanner*. in *Proceedings of ISMRM 15th Scientific Meeting*. 2007. Berlin, Germany.

61. Nordh, E., et al. *Does Changes in Gradient Duration Influence Q-Space-Based Determinations of Displacements In Vivo*. in *Proceedings of ISMRM 15th Scientific Meeting*. 2007. Berlin, Germany.

62. Farrell, J.A., et al., *High b-value q-space diffusion-weighted MRI of the human cervical spinal cord in vivo: feasibility and application to multiple sclerosis.* Magn Reson Med, 2008. **59**(5): p. 1079-89.

63. Mitra, P. and B. Halperin, *Effect of finite gradient pulse width in pulsed gradient diffusion measurements.* Journal of Magnetic Resonance, Series A, 1995. **113**(1): p. 94-101.

64. Budde, M.D., et al., *Toward accurate diagnosis of white matter pathology using diffusion tensor imaging.* Magn Reson Med, 2007. **57**(4): p. 688-95.

65. Hwang, S.N., et al., *An image-based finite difference model for simulating restricted diffusion.* Magn Reson Med, 2003. **50**(2): p. 373-82.

66. Wright, A.C., et al., *Construction and Calibration of a 50 T/m Z-Gradient Coil for q-Space Microscopy.* Journal of Magnetic Resonance, 2007. **186**: p. 17-25.

67. Ong, H.H. and F.W. Wehrli, *Quantifying axon diameter and intra-cellular volume fraction in excised mouse spinal cord with q-space imaging.* Neuroimage, 2010. **51**(4): p. 1360-6.

68. Ong, H.H., et al., *Indirect measurement of regional axon diameter in excised mouse spinal cord with q-space imaging: simulation and experimental studies.* Neuroimage, 2008. **40**(4): p. 1619-32.

69. Ong, H.H., et al. *Q-Space Simulations on Mouse Spinal Cord White Matter Tract Histologic Images*. in *Proceedings of ISMRM 14th Scientific Meeting*. 2006. Seattle, USA.

70. Ong, H.H. and F.W. Wehrli. *Empirical Estimation of Intra-Cellular Volume Fraction in Mouse Spinal Cord with Q-Space Diffusion MRI*. in *Proceedings of ISMRM 16th Scientific Meeting*. 2008. Toronto, Canada.

71. Ong, H.H. and F.W. Wehrli. *A Two-Compartment Model to Accurately Characterize Extra- and Intra-Cellular Spaces in Neural Tissue with Q-space Imaging*. in *Proceedings of ISMRM 16th Scientific Meeting*. 2008. Toronto, Canada.

72. Ong, H.H. and F.W. Wehrli. *Accurate Measurement of Mean Axon Diameter with Q-space Diffusion MRI* in *Proceedings of ISMRM 16th Scientific Meeting*. 2008 Toronto, Canada.

73. Ong, H.H., et al. *Q-Space Propagator Maps of Mouse Spinal Cord Provide Insight into Regional Axonal Architecture*. in *Proceedings of ISMRM 14th Scientific Meeting*. 2006. Seattle, USA.

74. Ong, H.H., et al. *Effects of Gradient Amplitude and Duration of Q-space Imaging*. in *Proceedings of ISMRM 15th Scientific Meeting*. 2007. Berlin, Germany.

Chapter 2: Methods and Materials

2.1 Introduction

Although several different methodologies are employed in this dissertation, the experimental data acquisition is the same for all except for the clinical implementation feasibility study in Chapter 7. In this chapter, the construction and evaluation of the custom gradient coil is first described. The animal specimen preparation and q-space imaging (QSI) experimental acquisition are then detailed. Finally, the histology protocol to provide a gold standard measurement of mean axon diameter (MAD) and intracellular space (ICS) volume fraction is employed and histologic results are reported here.

2.2 Hardware: Micro-Z gradient

2.2.1 Construction

To overcome instrumental limitations arising from the requirement of high displacement resolution and fulfillment of the short gradient pulse (SGP) approximation, as discussed in the previous chapter, a customized high-amplitude z-axis gradient and RF micro coil were designed. The gradient coil is capable of gradient strengths up to 50 T/m and it was interfaced to a 9.4T spectrometer/micro-imaging system (Bruker DMX 400 with Micro2.5 gradients and BAFPA40 amplifiers). The z-gradient, which will be referred to as the Micro-Z gradient, was constructed by Wright *et al.* and full details of the design features can be found in reference (1). Reduced gradient coil size has several advantages including lower power requirements and reduced Lorentz forces and eddy currents while smaller RF coil size leads to enhanced SNR from improved filling factor.

The z-axis gradient coil can be used in conjunction with the vendor-provided x- and y-axis gradient coils for imaging purposes.

The design chosen is based on one proposed by Callaghan *et al.* (2) consisting of a gradient coil patterned on a elongated Maxwell pair and a solenoidal RF coil, represented by the red circles and orange lines, respectively, in Figure 2.1a. The Maxwell pair comprised of magnet wire wound in four horizontal bunches through four holes drilled in two phenolic posts. A horizontal glass NMR tube was centered between the four wire bunches around which a three-turn solenoidal RF coil was wound. A smaller sample tube (o.d./i.d. = 3.0/2.4 mm) could then be inserted inside the larger tube. The whole set up was embedded in epoxy to provide mechanical stability and limit vibrations from Lorentz forces. A photo of the finished gradient/RF coil set before and after epoxy application is shown in Figure 2.1b. For additional protection, a Delrin cylindrical lid covered the entire assembly. The lid was fastened by Nylon screws that clamped the epoxy covered coil and o-rings on the lid allowed for a tight fit inside the NMR bore which provided further mechanical stability.

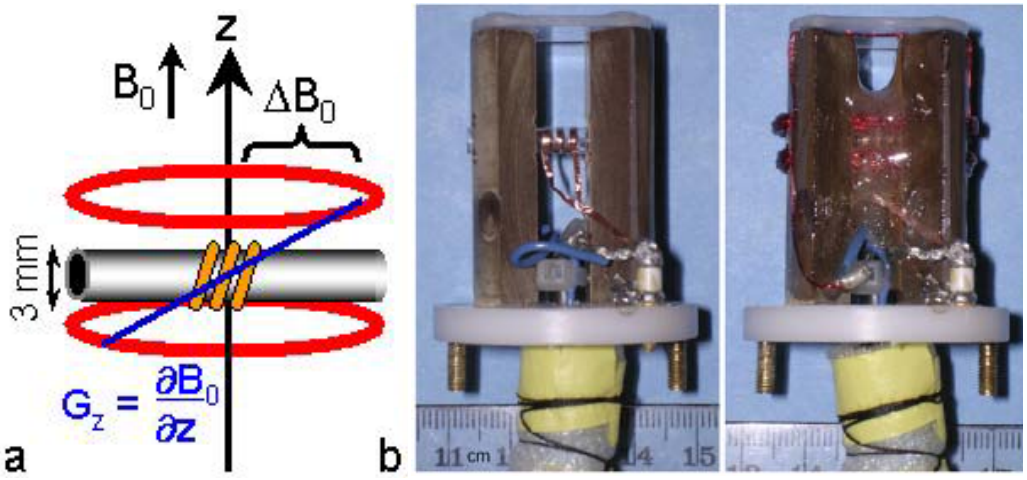

Figure 2.1. Micro-Z gradient coil: (a) Schematic of gradient/RF coil design. (b) Image of finished gradient/RF coil set before and after epoxy application.

2.2.2. Gradient calibration and performance evaluation

I assisted on the gradient calibration and performance evaluation, as detailed in reference (1), and a brief summary pertaining to my contributions is given here. Quantitative molecular diffusion measurements require accurate gradient pulse calibration. Specifically, one needs to know what gradient strength is generated for a given applied current. Gradient strength is linearly proportional to the applied current. The calibration procedure involves determining the proportionality constant, which is known as the gradient gain. Standard calibration methods usually work only for low gradient amplitudes. The same proportionality constant is used for higher amplitudes by assuming that the gradient coil continues to behave linearly at high amplitudes, which may not be true due to hardware imperfections. Here we accomplished a direct calibration of high gradient values in two steps: A) following conventional approaches to calibrate low gradient amplitudes (<4 T/m), we used a 1D imaging spin-echo experiment with the Micro-Z gradient as the read-out gradient and imaged a water-filled capillary, and B) using the results from step A, we calibrated higher gradient amplitudes by using a non-localized spin-echo experiment with the Micro-Z gradient applied as a bipolar gradient pair to measure the ^{1}H signal from polyethylene glycol (PEG) dissolved in D_2O in a 2.4 mm i.d. tube. Pulse sequences for steps A and B are shown in Figure 2.2.

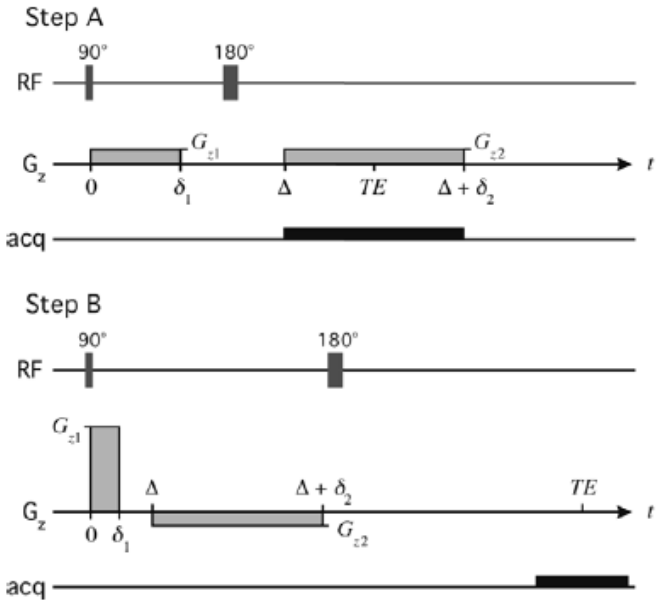

Figure 2.2. Pulse sequences for calibration steps A and B. G_z represents the Micro-Z gradient. In step A, the gradient amplitude $G_{z1} = G_{z2}$ and the delay $\delta_1 = 2\delta_2$. In step B, G_{z1}, G_{z2}, δ_1, and δ_2 are varied as described in the text. All RF pulses are non-selective. This figure is reproduced from reference (1) with permission from Alexander C. Wright.

In calibration step A, the width in Hz, $\Delta\nu$, of the 1D projection of the water-filled capillary as shown in Figure 2.3a (inset) is related to the capillary diameter, Δz, by

$$\Delta\nu = \frac{\gamma}{2\pi} G_z \Delta z \tag{2.1}$$

where G_z is the applied Micro-Z gradient. As the capillary has a known inner diameter of 1.1 mm, from the width $\Delta\nu$, the gradient amplitude can be derived for a given applied current. According to Eq. 2.1, $\Delta\nu$ should increase linearly with increasing applied current. Thus the gradient strength in step A was limited to calibrating gradient amplitudes lower than 4 T/m by the largest available receive bandwidth (200 kHz) of the Bruker system, which restricted the largest measurable $\Delta\nu$ for the given capillary diameter, i.e. Δz. By plotting the gradient amplitude derived from $\Delta\nu$ relative to the applied current as measured from an oscilloscope, the gradient gain can be calculated from the slope. Figure

2.3 shows the calibration curve for step A. The gradient gain was calculated to be 1.253 T/m/A, meaning that for every 1 A of applied current, the gradient amplitude will increase by 1.253 T/m. The high R^2 of 0.9998 indicates a linear current response as expected.

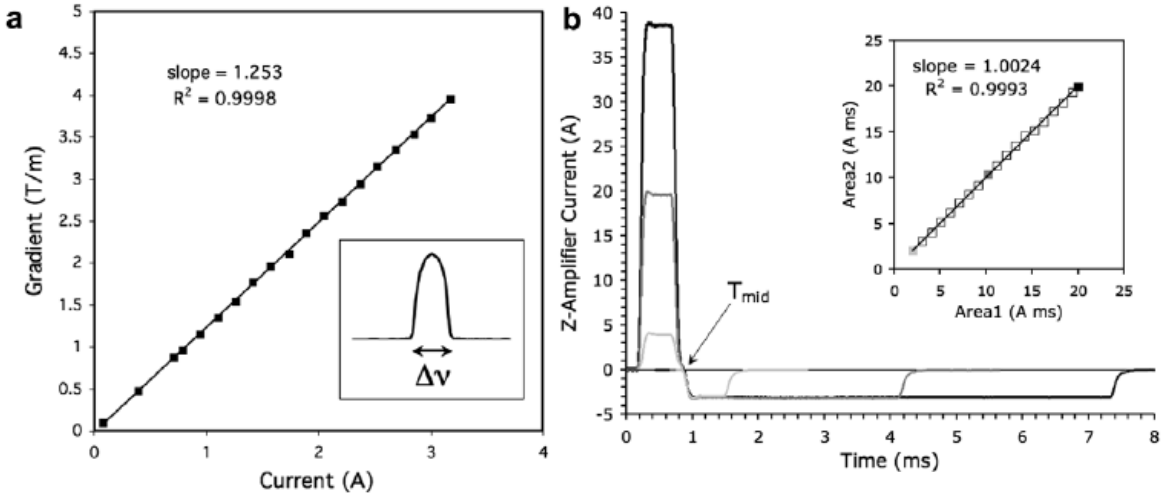

Figure 2.3. (a) Gradient calibration curve measured from Step A. Inset shows a typical 1D projection of the capillary tube and its width, Δν. (b) Measured Micro-Z gradient waveforms for calibration step B showing various G_{z1} and δ_2 values. Note $\Delta = \delta_1$. Inset shows a plot of the area of the first gradient vs. the magnitude of the area of the second gradient after adjusting the duration of the second gradient, δ_2, to maximize the echo intensity. This figure is reproduced from reference (1) with permission from Alexander C. Wright.

In calibration step B, the Micro-Z gradient was applied as a bipolar gradient pair in which one of the gradient pulse amplitudes is known and the other not known. As described below, the known gradient pulse amplitude is then used to infer the unknown amplitude. An important consideration with this approach is the bipolar gradient pair is sensitive to molecular diffusion which causes signal attenuation. As strong gradients up to 50 T/m are used, a NMR sensitive material with very low diffusivity is needed to ensure sufficient signal is detected. A solution of PEG dissolved in D_2O (8kD PEG at 12.5 w% dilution) was used as its diffusivity was measured to be 2.3×10^{-7} cm^2/s (1). This

is two orders of magnitude slower than free water and offered a detectable signal even with maximum gradient strength. From Figure 2.2, after a non-selective 90° pulse, a Micro-Z gradient pulse of duration δ_1 = 0.4 ms and unknown amplitude G_{z1} are applied. To minimize diffusion effects, a second Micro-Z gradient of variable duration δ_2 and known amplitude G_{z2} = 3.8 T/m, is applied using the gradient gain from calibration step A. After a non-selective 180° pulse, the echo amplitude is recorded. For a constant echo time (TE), the maximum echo amplitude occurs when the area of the first gradient pulse is equal to the negative area of second gradient pulse. In other words, the zeroth moment, k_z, of the bipolar gradient waveform is zero:

$$k_z = \frac{\gamma}{2\pi}\left(\int_0^{T_{mid}} G_{z1}(t)dt - \int_{T_{mid}}^{\delta_2} G_{z2}(t)dt \right) = 0 \qquad (2.2)$$

where T_{mid} is defined as the first zero-crossing between the positive first gradient pulse and the negative second gradient pulse (Figure 2.3). The duration of the second gradient pulse, δ_2, is varied until an echo maximum is found and then the bipolar gradient waveform is recorded from an oscilloscope using Labview (National Instruments, Austin, Texas, USA). Sample waveforms at various G_{z1} and δ_2 values are shown in Figure 2.3. Note that the gradient amplitude is not recorded directly, but rather the applied current from the gradient amplifier. Therefore Eq. 2.2 can be expressed as:

$$k_z = \frac{\gamma}{2\pi}\left(g_B \int_0^{T_{mid}} I_{z1}(t)dt - g_A \int_{T_{mid}}^{\delta_2} I_{z2}(t)dt \right) = 0 \qquad (2.3)$$

where g_A and g_B are the gradient gains derived from calibration steps A and B. $I_{z1}(t)$ and $I_{z2}(t)$ are the recorded gradient current waveforms for the first and second gradient pulses. Note that the gradient gain g_A has already been determined in calibration step A and the gradient gain g_B is unknown. Solving for g_B gives:

$$g_B = g_A \frac{\int_{T_{mid}}^{\delta_2} I_{z2}(t)dt}{\int_0^{T_{mid}} I_{z1}(t)dt} = g_A \frac{Area2}{Area1} \tag{2.4}$$

where Area1 and Area2 represent the integrated areas of the current waveforms $I_{z1}(t)$ and $I_{z2}(t)$ recorded with Labview. The gradient gain g_B can now be determine and used to calculate the unknown gradient amplitude G_{z1}. By varying the applied current of the first gradient pulse and repeating the above steps, a series of gradient amplitude vs. applied gradient points can be generated for gradient amplitudes greater than 4 T/m. It is important to note that maximum echo condition results in an Area2/Area1 ratio of one. A plot of Area1 vs. Area2 for the series of G_{z1} values used in calibration step B (Figure 2.3b, inset) shows that this is indeed the case as the slope of the linear regression is 1.0024 (R^2 = 0.9993). Figure 2.4 shows the final gradient calibration curve of gradient amplitude vs applied current from steps A (black squares) and B (white squares). The overall gradient gain determined from the slope of the line of best fit was 1.255 T/m/A. A linear current

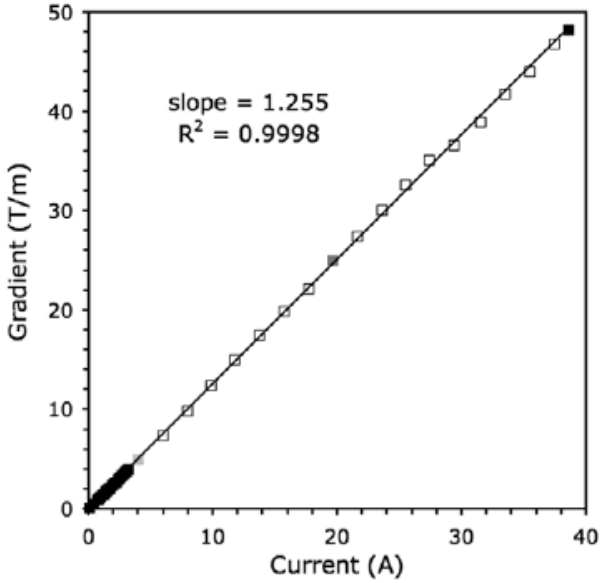

Figure 2.4. Final gradient calibration curve combining steps A (black squares) and B (white squares). Note the linear response over the entire gradient amplitude range. This figure is reproduced from reference (1) with permission from Alexander C. Wright.

response was observed over the entire range of gradient amplitudes ($R^2 = 0.9998$). As the maximum applied current from the gradient amplifier is 40 A, the expected maximum amplitude of the Micro-Z gradient is 50.2 T/m.

To test the Micro-Z gradient/RF coil for use in quantitative spectroscopic experiments, we used the coil to observe q-space echo attenuation diffraction patterns from water surrounding closely packed polystyrene microspheres (4.5 μm diameter) as previously studied (3), where the first maximum occurs at a q-value equal to the inverse of the pore diameter. The results (Figure 2.5a) show a maximum occurring at a q-value corresponding to 1/4.5 μm, as expected. To test the gradient/RF coil for use in quantitative imaging experiments, we used the coil to generate an ADC map for a sample tube of 1.2 mM Gd-DTPA doped water as shown in Figure 2.5b. Using a PGSE imaging sequence (TR = 1s, TE/Δ/δ = 20/15/2 ms) and a maximum b-value of ~15,000 s/cm^2, the calculated water ADC was 1.92×10^{-5} cm^2/s at 19° C, which not only matched literature values (4), but also matched the value calculated from an ADC map generated using the standard vendor z-gradient. These results indicate the accuracy of gradient calibration and show the potential for using the Micro-Z gradient for quantitative applications.

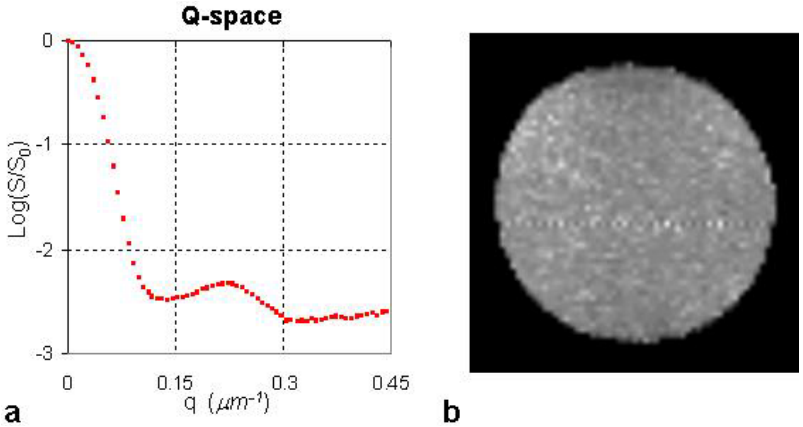

Figure 2.5. (a) Q-space echo attenuation plot for packed polystyrene microspheres (4.5 μm diameter) (b) ADC map of 1.2 mM Gd-DTPA doped water.

As a further demonstration of its micro-imaging capabilities, PGSE diffusion-weighted images of a fixed mouse cervical spinal cord immersed in phosphate-buffered saline (PBS) (see Chapter 2.3) using the Micro-Z gradient for both phase-encoding and diffusion-weighting. Due to the geometry of the Micro-Z gradient, the diffusion-weighting was applied perpendicular to the spinal cord longitudinal axis. Figure 2.6 shows three sample images with b-values of 0.6, 2.5, 9.7×10^5 s/cm^2. The low b-value image (left) shows lower intensity in the WM region relative to GM. This is expected due to the presence of myelin in WM resulting in lower water concentration. The intermediate b-value image (middle) shows iso-intensity in the WM and GM regions. Note that the saline surrounding the spinal cord is almost completely attenuated due to its high diffusivity. The high b-value image shows higher intensity in WM than in GM. This reversal in contrast is the result of water diffusion in WM being restricted while there is no such restriction in GM (5). This leads to a smaller average molecular displacement due to diffusion in WM than in GM, which results in less signal attenuation at high b-values. These images demonstrate the capability of the Micro-Z gradient to image restricted diffusion in biological tissues and provides a proof-of-concept of for regional assessment of restricted diffusion in mouse spinal cords as described in chapters 4-6.

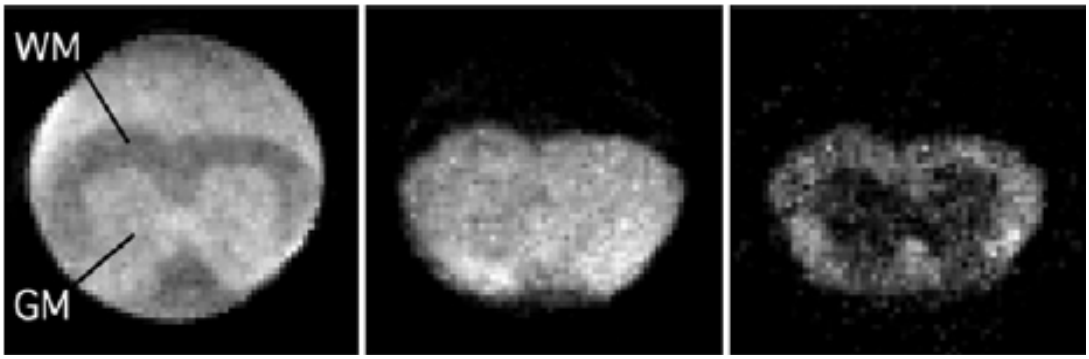

Figure 2.6. Diffusion-weighted images of a fixed mouse cervical spinal cord using the Micro-Z gradients as diffusion and phase-encoding gradients. Three images are shown with increasing b-values from left to right: 0.6, 2.5, and 9.7×10^5 s/cm^2

2.3 Animal specimen preparation

Mouse spinal cords were chosen for QSI experiments because they fit the small size of the sample bore of the Micro-Z gradient. Spinal cords also provide a simple WM tract architecture where the majority of tracts are parallel to the cord longitudinal axis. This simplifies experimental setup, data processing, and interpretation. Five healthy C57 BL6 mice (8-9 months, 25-30 mg, Charles River, Wilmington, MA) were anesthetized with an intraperitoneal injection of 10 mg ketamine/1 mg acepromazine per ml (0.5 mL per mouse; Abbot Laboratories, North Chicago, IL) and perfused through the heart with 20 mL of phosphate buffer solution, followed by 20 mL of fixing solution (4% glutaraldehyde and 2% paraformaldehyde in 10 mM PBS). Following fixation, the entire spinal cord was resected and postfixed for at least two weeks in a 2.5% glutaraldehyde and 2% paraformaldehyde in 0.1 M sodium cacodylate solution. Cervical C6/C7 sections (3-4 mm in length) were then cut from each spinal cord. All spinal cord specimens were stored in the second fixing solution until time of experiment. Before each imaging experiment, each spinal cord specimen was placed in a 3 mm NMR tube filled with PBS, sealed with parafilm, and placed in the Micro-Z gradient. After performing QSI experiments, cervical spinal sections that corresponded to the QSI slice were processed for optical histologic imaging (see below).

2.4 QSI acquisition

All QSI experiments on fixed excised cervical mouse spinal cords were performed with the custom Micro-Z gradient. A QSI single data set was acquired with the

following parameters and was analyzed in different ways depending on the method of interest (see Chapters 4-6).

A diffusion-weighted stimulated-echo imaging sequence was optimized for use with the Micro-Z gradient (Figure 2.7). Additional crusher and spoiling gradients were added to minimize imperfections in the 90° RF pulse and eliminate residual transverse magnetization at the end of TR, respectively. The following imaging parameters were used: 64 × 64 matrix (zero-filled to 256 × 256), spectral width = 25 kHz, TR = 2 s, averages = 6, TE = 17.4 ms, Δ = 10 ms, δ = 0.4 ms, mixing time = 9 ms, FOV = 4 mm, and a slice thickness = 1.0 mm. Experiments were conducted at an ambient temperature of 19 °C. Diffusion gradients were applied along the z-axis, i.e. perpendicular to the spinal cord longitudinal axis, in 63 steps of 0.013 μm^{-1} yielding q_{max} = 0.82 μm^{-1} (48 T/m gradient strength). The q-values were numerically calculated from the actual z-gradient amplifier current output as monitored on an oscilloscope with LabView. When investigating the effects of failing to fulfill the SGP approximation, all above imaging parameters were used except δ = 5 ms and the diffusion gradients were again applied along the z-axis.

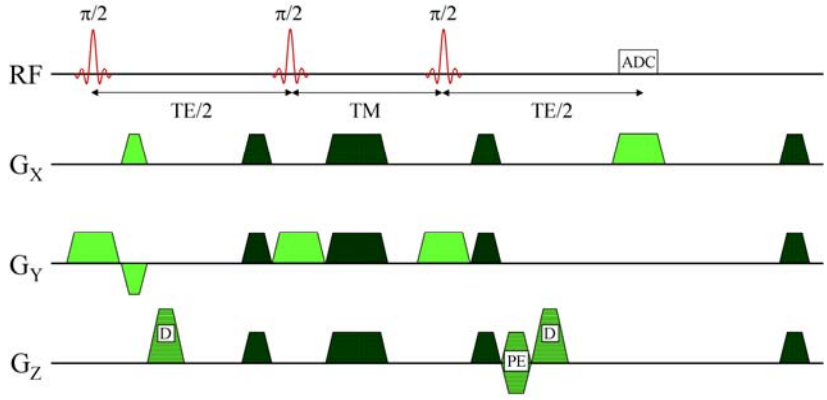

Figure 2.7. Diagram of diffusion-weighted stimulated echo pulse sequence used for QSI experiments. G_Z was applied using the Micro-Z gradient. Labels: D = diffusion gradient, PE = phase-encoding gradient, TE = echo time, TM = mixing time, ADC = analog to digital converter. Darker gradients signify spoiling and crusher gradient moments.

2.5 Histology of Mouse Spinal Cord

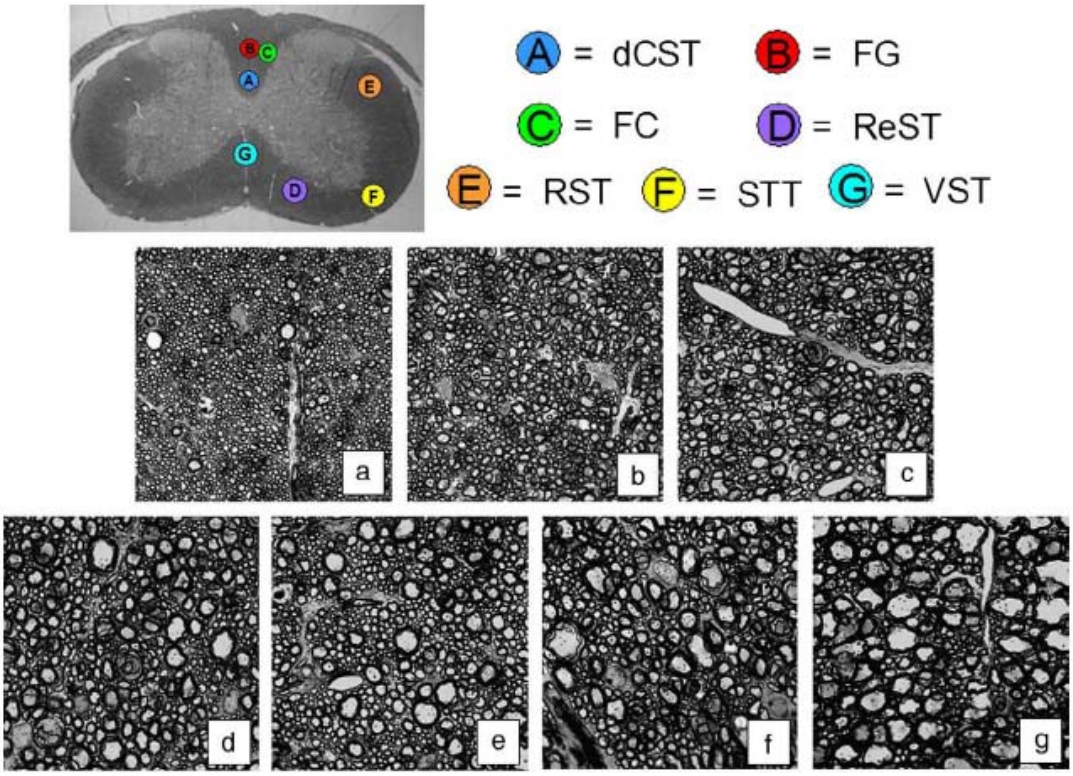

Figure 2.8. Top Image: Optical image of C6/C7 mouse cord section showing WM tract locations: A) dorsal corticospinal (dCST), B) gracilis (FG), C) cuneatus (FC), D) rubrospinal (RST), E) spinothalamic (STT), F) reticulospinal (ReST), G) vestibulospinal (VST). The spinal cord is approximately 3 mm wide. Bottom Images: Optical images of WM tracts from mouse spinal cord C6/C7 section. Each image is 700 × 700 with a pixel resolution of 0.1 × 0.1 μm.

Histologic measurements from light microscopic images of fixed mouse spinal cord sections (from C6-C7) embedded in epoxy were used as gold-standard measurements of axonal architecture and to provide input images for simulations (see Chapter 3). Seven WM tract locations were obtained after staining for myelin with toluidine blue. These locations were defined in reference (6) and are shown in Figure 2.8 along with sample toluidine blue images. WM tracts were selected to reflect a range of MAD, e.g. it can be clearly seen in Figure 2.8 that the dCST tract has the smallest axons

while the VST tract has the largest. Each image was digitized with a CUE-2 image analyzer (Olympus American, Melville, NY), in which a region of interest (ROI) was selected as input to the simulation program. The size of an ROI approximated the pixel size of the experimental data before zero-filling.

Table 2.1. Average regional WM tract histologic measurements

	dCST	FG	RST	ReST	FC	STT	VST
MAD (μm)	0.81 ± 0.06	0.99 ± 0.06	1.16 ± 0.04	1.36 ± 0.09	1.40 ± 0.14	1.44 ± 0.11	1.82 ± 0.26
Axon Diameter Stdev (μm)	0.31 ± 0.08	0.47 ± 0.06	0.71 ± 0.10	0.89 ± 0.10	0.88 ± 0.10	0.98 ± 0.18	1.40 ± 0.13
ICS Area Fraction	0.21 ± 0.04	0.22 ± 0.03	0.25 ± 0.04	0.27 ± 0.04	0.27 ± 0.01	0.23 ± 0.04	0.28 ± 0.06
ECS Area Fraction	0.35 ± 0.10	0.31 ± 0.07	0.31 ± 0.07	0.32 ± 0.06	0.27 ± 0.05	0.35 ± 0.11	0.31 ± 0.12
Myelin Area Fraction	0.45 ± 0.07	0.47 ± 0.05	0.43 ± 0.04	0.41 ± 0.04	0.46 ± 0.06	0.42 ± 0.08	0.41 ± 0.06
Axon Count	1670 ± 267	1101 ±146	791 ± 122	574 ± 79	591 ± 97	436 ± 68	289 ± 78
Axon Density (10^5/mm^2)	3.42 ± 0.55	2.25 ± 0.30	1.62 ± 0.25	1.18 ± 0.16	1.21 ± 0.20	0.89 ± 0.14	0.59 ± 0.16

Microscopic images were segmented into ECS, ICS, and myelin compartments using a program written in Matlab (Mathworks, Natick, MA, USA). Due to the toluidine blue staining, myelin is dark on histology. However, the ECS and ICS spaces have similar signal intensities so ICS must be manually labeled. First, seed points were placed within the axons to initiate a watershed-based segmentation (7, 8) of the ICS. The myelin was then segmented using an interactive profile-based boundary detection algorithm (9). After manual correction, the ECS was determined by subtracting the union of the axon and the myelin regions from the entire image space. The segmented images were then

used to calculate MAD (equating each ICS axon area to a circle, excluding the myelin), axon count, axon density, and fractional areas of the ECS, ICS, and myelin (Table 2.1). In Table 2.1, the WM tracts were organized in order of increasing MAD. The histologic results will be further discussed in later chapters in comparison with experimental results. Finally, the segmented images were down-sampled to 256 × 256 to serve as input for the q-space simulations as discussed in Chapter 3.

As we are comparing experimental QSI data acquired with a slice thickness of 1 mm (to obtain sufficient signal-to-noise ratio) to histology with a slice thickness of 0.5 μm, we investigated how much axon diameter variation occurred through a 1 mm slice. Toward this goal, we obtained from a single specimen six sections spaced 200 μm apart such that they spanned the 1 mm slice thickness used in the imaging experiments. Seven WM tract ROIs (20 pixels each) were imaged from each section, segmented, and the mean axon diameter was calculated. These histologic results as well as further comparisons with experimental QSI data are reported in Chapter 4.

2.6 Summary

The materials and methods common to various analysis approaches have been described in this chapter. The construction and evaluation of a custom high-amplitude gradient, known as the Micro-Z gradient was covered. The Micro-Z gradient was demonstrated to provide a maximum amplitude of 50 T/m, allowing for the high displacement resolution needed for accurate measurement of molecular displacements within axons. Spinal cords were harvested from healthy 8-9 month old C57 BL6 mice after perfusion fixation. After QSI experiments were completed, histology was performed

and myelin was stained with Toluidine blue. MAD and other axon morphology metrics could then be determined from the histologic images after segmentation for comparison with experimental data. The segmented histologic images were used for q-space simulation (Chapter 3). The raw QSI data along with the histologic data described here will be used in validating the displacement PDF (Chapter 4), low q-value (Chapter 5), and VGPD (Chapter 6) methods.

2.7 Literature citations

1. Wright, A.C., et al., *Construction and Calibration of a 50 T/m Z-Gradient Coil for q-Space Microscopy.* Journal of Magnetic Resonance, 2007. **186**: p. 17-25.
2. Callaghan, P.T., M.E. Komlosh, and M. Nyden, *High magnetic field gradient PGSE NMR in the presence of a large polarizing field.* J Magn Reson, 1998. **133**(1): p. 177-82.
3. Coy, A. and P.T. Callaghan, *Pulsed Gradient Spin-Echo NMR "Diffusive Diffraction" Experiments on Water Surrounding Close-Packed Polymer Spheres.* Journal of Colloid and Interface Science, 1994. **168**(2): p. 373-379.
4. Mills, R., *Self-diffusion in normal and heavy water in the range of 1-45 degrees.* J Phys Chem, 1973. **77**: p. 685-688.
5. Beaulieu, C., *The basis of anisotropic water diffusion in the nervous system - a technical review.* NMR Biomed, 2002. **15**(7-8): p. 435-55.
6. Schwartz, E.D., et al., *Ex vivo evaluation of ADC values within spinal cord white matter tracts.* AJNR Am J Neuroradiol, 2005. **26**(2): p. 390-7.
7. Meyer, F. and S. Beucher, *Morphological segmentation.* Journal of Visual Communication and Image Representation, 1990. **1**(1): p. 21--46.
8. Beucher, S. and C. Lantuejoul. *Use of Watersheds In Contour Detection*. in *International Workshop on Image Processing (Real-time Edge and Motion Detection/Estimation)*. 1979. Rennes, France.
9. Pal, N.R. and S.K. Pal, *A review of image segmentation techniques.* Pattern Recognition, 1993. **26**(9, pp. 1277-1294): p. 1277-1294.

Chapter 3: Q-space Simulations

3.1 Introduction

As discussed in Chapter 1, the displacement probability density function (PDF) from q-space imaging (QSI) is an empirical measurement of the average molecular displacement due to diffusion, which is influenced by axon architecture. Various metrics can be used to characterize the displacement PDF and provide insight into this architecture. However, the displacement PDF is also affected by other factors that are difficult to investigate independently.

For example, the displacement PDF reflects molecular displacement in both the intracellular (ICS) and extracellular (ECS) spaces, which may have different signal relaxation rates and restrictions to diffusion (1, 2). The contribution from displacement in each space is not well understood and this complicates the interpretation of the PDF. Furthermore, WM tissue exhibits large variations in axon shape and size, which will influence molecular displacements. How well the displacement PDF represents the mean axon diameter (MAD) under these conditions has not been studied.

These factors which influence the displacement PDF are very difficult to investigate experimentally due to the inability to reliably measure and vary them in a controllable manner. Computer simulations, unlike experiments, provide an environment where these factors can be precisely controlled and used to assess their contributions to the displacement PDF. In this chapter, QSI simulations on both synthetic axons and histologic images are used to investigate the effects of signals from both ECS and ICS, variability of cell size and shape, membrane and myelin permeability, and axon loss on QSI measurements of axonal architecture. The diffusion simulation program and input

images are first described and then simulation results are summarized and discussed. The insights from the simulation results will aid in the understanding and interpretation of experimental results.

3.2 Methods

3.2.1 Diffusion simulation program

Q-space simulations were performed with a program that is based on solving the diffusion equation using a 3D finite-difference model developed by Hwang *et al.* (3). The program, written in C (CodeWarrior, Metrowerks, Austin, TX) computes the signal during execution of a PGSE sequence. Details of the algorithm are described in (3) and thus only a brief summary is given here. Assuming a spatially uniform diffusion coefficient for each specific region, the diffusion equation can be expressed as

$$\frac{\partial c}{\partial t} = D\nabla^2 c \qquad (3.1)$$

where D is the diffusion coefficient, ∇ is the gradient operator with respect to the spatial coordinates and c is the concentration of the diffusing material.

In a forward time-centered space finite difference model, time and space are discretized and the partial derivatives are approximated by finite differences. Each image pixel is assigned to intracellular space, extracellular space or myelin, each with user-defined characteristic T_2, diffusion coefficient, and permeability values. Starting from an initial state, particles are allowed to diffuse between pixels with a calculated probability at each time step, and c is updated accordingly.

To simulate the MR signal, the concentration c in Eq. (3.1) is replaced by the x and y components of the transverse magnetization, which are updated after each time step.

During the application of the diffusion gradient, phase accumulation is added after each time step. The final MR signal is the vector sum of magnetization of each pixel at echo time. In order to avoid artifactually restricted diffusion due to the image boundary, which is modeled as a reflecting boundary, only signal from the central one third of the image is used for analysis. The algorithm has been validated for restricted diffusion bounded by cylindrical pores and for diffusion within hexagonal array of cylinders, where the simulated data agreed well with existing analytical solutions (3).

3.2.2 Input images

Synthetic axons

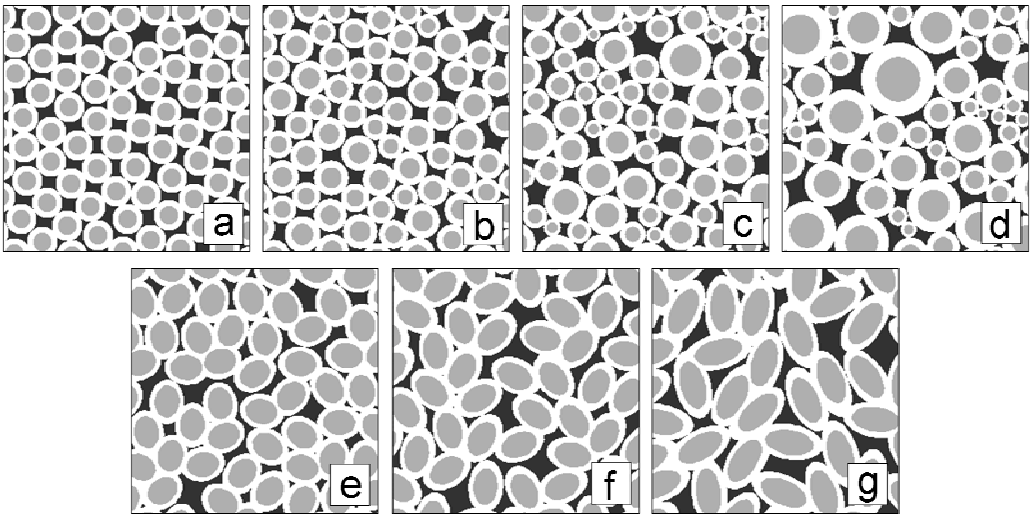

Figure 3.1. Synthetic circular axon images generated with a Gaussian distribution of diameters (mean and standard deviation are μ and σ respectively): (a) $\sigma/\mu = 0.0$, (b) $\sigma/\mu = 0.1$, (c) $\sigma/\mu = 0.25$, (d) $\sigma/\mu = 0.5$. The white rings signify myelin. The mean axon diameter (excluding myelin) was held constant at 14.48 μm. Synthetic ellipsoidal axon images generated with different ratios (R) of major axis over minor axis lengths (e) R=1.25, (f) R=1.5, (g) R=2.0. The mean axon diameter (excluding myelin) was held constant at ~25 μm.

In order to investigate the effect of axon size distribution on QSI derived parameters such as displacement PDF FWHM, zero-displacement probability (ZDP), and

kurtosis, several images of randomly packed circular axons (256 × 256 matrix, pixel size 0.75 × 0.75 μm^2) with a Gaussian distribution of diameters were generated using a custom IDL program (Interactive Data Language, Research Systems, Boulder, CO) as input for the q-space simulation program (Figure 3.1a-d). In order to investigate the effect of axon shape distribution on QSI derived parameters, images of packed ellipsoidally shaped axons (256 × 256 matrix, pixel size 0.75 × 0.75 μm^2) were drawn in Powerpoint (Microsoft Office, Microsoft, Seattle, WA) with varying major axis over minor axis lengths ratios as input for the q-space simulation program (Figure 3.1e-g).

Histologic images

As described in Chapter 2, light microscopic images were obtained from all the fixed mouse cervical spinal cord specimens at seven WM tract locations after staining for myelin with toluidine blue. These images were segmented into ECS, ICS, and myelin compartments using a program written in Matlab (Mathworks, Natick, MA) and use to quantify metrics of axon morphology such as mean axon diameter and ICS/ECS volume fractions. The segmented images were subsequently down-sampled to 256 × 256 pixels to serve as input for the q-space simulations (Figure 3.2).

3.2.3 Diffusion simulation experiments and analysis

Two sets of q-space simulations were run: first on the previously described synthetic axon images and subsequently on the segmented histologic images of WM tracts. For the former, the PGSE sequence parameters were: TR = 1 s, TE = 65 ms, Δ = 60 ms, δ = 2 ms, and the diffusion gradients were applied in 63 increments in steps of

0.009 μm^{-1} yielding $q_{max} = 0.54\ \mu m^{-1}$. The ECS and ICS T_2 were both assigned to be 300 ms and the corresponding diffusion coefficients were both assigned to be $2.5 \times 10^{-5}\ cm^2/s$. Simulations did not include signal from myelin. The T_2 values were chosen to match the long T_2 component of neural tissues reported in literature (4). The diffusion coefficients were chosen to match those of water at room temperature as it was assumed to be an upper limit for the diffusion coefficients found in axonal tissue. Simulations on the circular axons with permeability $p = 0$ (i.e. perfectly reflecting boundaries) were run with signal occupying only the ICS or only the ECS. Simulations on the ellipsoidal axons were performed with signal occupying only the ICS and with $p = 0$.

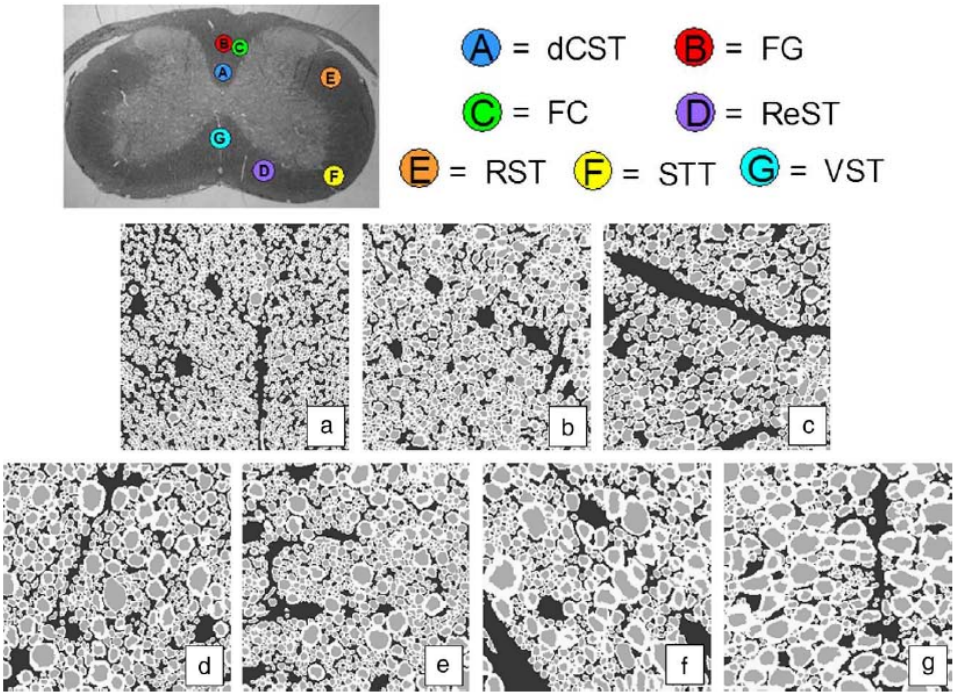

Figure 3.2. Top Image: Optical image of C6/C7 mouse cord section showing WM tract locations: A) dorsal corticospinal (dCST), B) gracilis (FG), C) cuneatus (FC), D) rubrospinal (RST), E) spinothalamic (STT), F) reticulospinal (ReST), G) vestibulospinal (VST). The spinal cord is approximately 3 mm wide. Bottom Images: Segmented down-sampled images of WM tracts from mouse spinal cord C6/C7 section. They white areas signify myelin. Each image is 256 × 256 pixels with a resolution of 0.27 × 0.27 μm.

For the segmented histologic images, the PGSE sequence parameters were: TR = 2 s, TE = 17.4 ms, Δ = 10 ms, δ = 0.4 ms, and the diffusion gradients were applied in 63 increments in steps of 0.013 μm^{-1} yielding q_{max} = 0.82 μm^{-1} along the dorsal-ventral axis to approximate the direction of the applied diffusion gradients in our experiments. The following T_2, permeability and diffusion coefficients were chosen from literature values (4). The ECS, ICS and myelin diffusion coefficients were assigned values of 1.65, 1.12 and 1.12 $\mu m^2/s$, respectively. The myelin T_2 was set to 19 ms and the myelin water concentration to 15%. Due to the uncertainties in ECS and ICS T_2 values (2), i.e. whether ECS or ICS had the longer T_2 value, both cases were simulated: the ECS-weighted case where ECS and ICS T_2s were 300 and 78 ms, respectively, and the ICS-weighted case where ECS and ICS T_2s were 78 and 300 ms respectively; the ECS and ICS water concentrations were both set to 85% and the myelin/membrane permeability to 0.01 $\mu m/ms$.

All data analysis was performed in IDL (Interactive Data Language, Research Systems, Boulder, CO). Each simulation outputs the echo attenuation as a function of q-value, which is then normalized to the maximum value at zero q-value. In order to compute a purely real Fourier transform in accordance with Fourier transform theory, the echo attenuation plot was reflected about the origin (q = 0) to fill in the *negative* q-values, resulting in 127 total q-values (1 zero q-value, 63 positive, and 63 negative q-values). A displacement PDF was computed by applying a 1D Fourier transform of the modified echo attenuation plot. After calculating the displacement PDFs, FWHM, ZDP, and kurtosis values were recorded.

3.3 Results

3.3.1 Synthetic axons

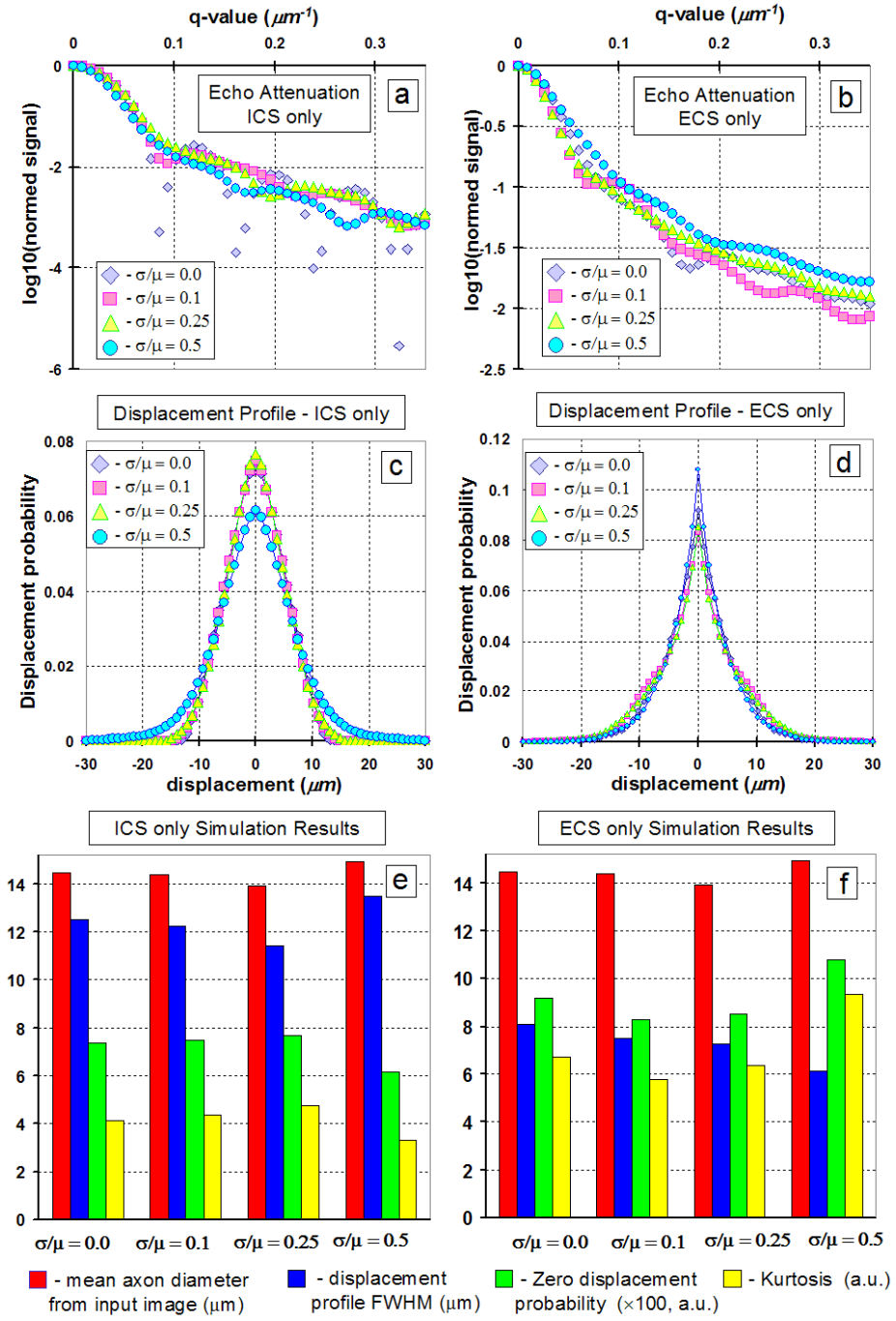

Figure 3.3. Summary of simulation results for synthetic circular axons of varying diameter mean and standard deviation ratios (μ and σ respectively). (a) Echo attenuation for signal from ICS only. (b) Echo attenuation for signal from ECS only. (c) Displacement PDF for signal from ICS only. (d) Displacement PDF for signal from ECS only. Mean axon diameter, FWHM, zero-displacement probability, and kurtosis for (e) signal from ICS only and (f) signal from ECS only.

Figure 3.3 summarizes the simulation results of the synthetic circular axons. For circles of constant diameter and impermeable walls, the ICS-only simulations showed the expected diffraction minima for cylindrical pores (5) located at $q \cdot a \sim 1.22$, where a is the axon mean diameter, which attests to the accuracy of the simulation program. The diffraction minimum is gradually smeared out with increasing diameter variance. Diffraction minima correspond to the situation of maximal phase dispersion, which occurs at a specific q-value that depends on pore size and shape. The ECS-only simulations never showed any diffraction pattern.

Figure 3.4 summarizes the simulation results of the synthetic ellipsoidal axons. A weak q-space diffraction pattern is visible as the ellipsoidal axon shape and area is constant in each input image. However, due to the random orientation of the ellipse axes, the diffraction pattern is not as pronounced as compared to the circular axons shown in Figure 3.3.

As expected, with increasing axon size and shape distribution, the q-space diffraction pattern was smeared out. The axon geometry information seems to be exclusively captured by the ICS signal. Only the ICS-only displacement PDF metrics correlated with the expected mean axon diameter (FWHM: $R^2 = 0.99$, $p = 0.0047$, slope = 2.08; and kurtosis: $R^2 = 0.95$, $p = 0.027$, slope = -2.89).

3.3.2 Histologic images

Figure 3.5 summarizes the simulations results on the histologic images with axon diameters derived from histology. The FWHM increases, and ZDP and kurtosis decrease with increasing mean axon diameter in all plots. Note that simulated FWHM showed the

expected positive (R^2 = 0.88, p = 0.0019, slope = 0.60, and R^2 = 0.84, p = 0.0036, slope = 0.66 for ECS and ICS weighted simulations, respectively) and the simulated zero-displacement probability and kurtosis values showed the expected negative correlations (zero-displacement probability: R^2 = 0.73, p = 0.0132, slope = -0.19 and R^2 = 0.76, p = 0.01, slope = -0.23, for ECS and ICS weighted simulations, respectively; Kurtosis: R^2 = 0.79, p = 0.0079, slope = -46 and R^2 = 0.83, p = 0.0042, slope = -58, for ECS and ICS weighted simulations, respectively) with the average axon diameters calculated histology. Note further that simulated FWHM, zero-displacement probability (ZDP) and kurtosis showed high correlation between ICS weighted and ECS weighted simulations (FWHM: R^2 = 0.99, p < 0.0001, slope = 0.89, ZDP: R^2 = 0.996, p < 0.0001, slope = 0.84, and Kurtosis: R^2 = 0.99, p < 0.0001, slope = 0.81, respectively).

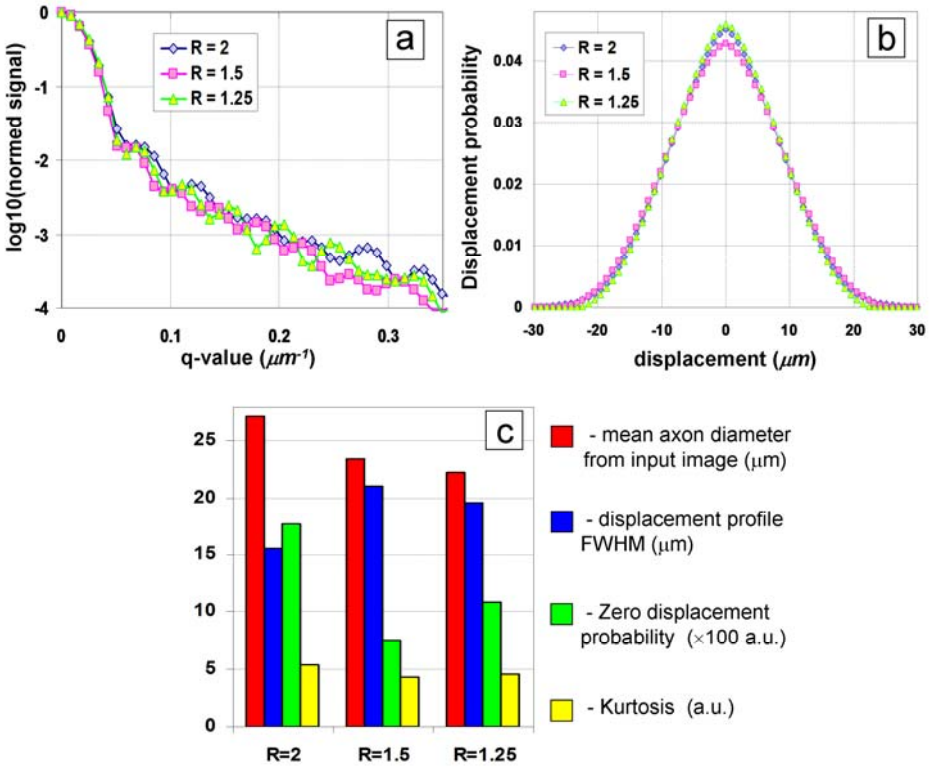

Figure 3.4. Summary of simulation results for synthetic ellipsoidal axons of varying major and minor axis diameter ratios (*R*). (a) q-space echo attenuations (b) displacement PDF. (c) Mean axon diameter, FWHM, zero-displacement probability, and kurtosis values.

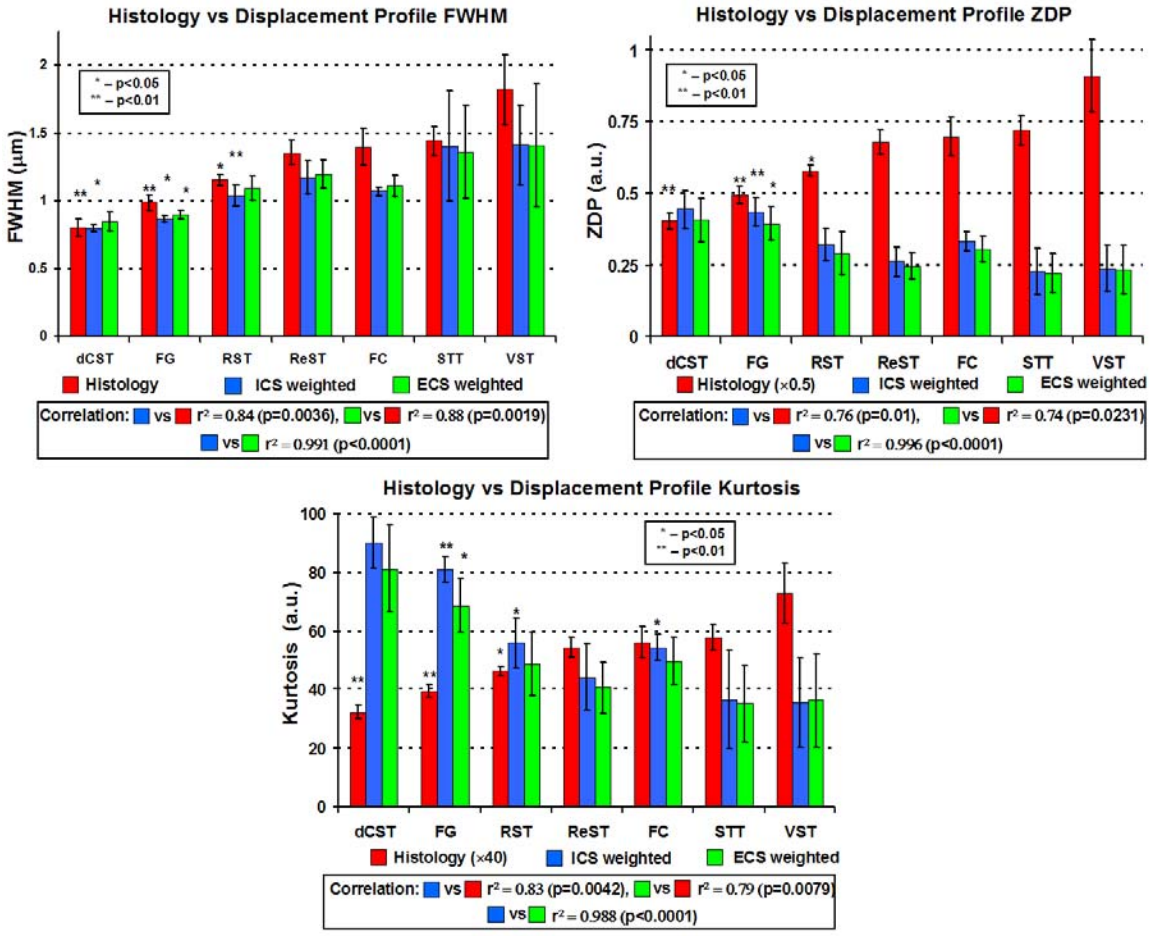

Figure 3.5. Summary of q-space simulations based on histologic images showing mean axon diameter, FWHM, zero-displacement probability (ZDP),and kurtosis values for each WM tract averaged over all five specimens under simulation conditions of ICS-weighted signal and ICS-weighted signal. Each asterisk represents the p-value of a paired t-test comparison with the next similar colored bar to the right: * = $p<0.05$, ** = $p<0.01$.

3.4 Discussion

3.4.1 Synthetic axons

It is important to note that most of the simulations run with the synthetic circular axons were performed with the signal either in the ECS or ICS in order to remove complications due to mixing of the ECS and ICS signal. The results reported here support the idea that with increasing variation in cell size and shape, the diffraction pattern observed in the echo attenuation is reduced in intensity and is eventually removed when

μ/σ was larger than 0.1. Nevertheless, the displacement PDF showed the same basic shape across all ratios of μ/σ. In particular, the ICS-only simulations did not show much change in FWHM, ZDP, or kurtosis as axon size distribution and shape were varied.

The axon geometry information seems to be exclusively captured by the ICS signal as the ECS only simulations did not show any correspondence with mean axon diameter (Figure 3.3 e-f). This observation supports the theory that diffusion in ECS and ICS is hindered and restricted, respectively (1). As long as the diffusion gradients are orthogonal to the WM tracts, QSI displacement PDFs containing both ICS and ECS signals may still retain information on axonal architecture. Although this information may be obscured if both signals are present, it should be recoverable if the ECS and ICS displacement PDFs could somehow be separated.

3.4.2 Histologic images

Unlike the synthetic axon simulations, the histologic image simulations were only run with signal from both ECS and ICS. What was being investigated was the effect of ECS and ICS T_2 on the QSI experiment as the precise T_2 values are not known. ECS-weighted or ICS-weighted simulations were run simply by setting the ECS or ICS T_2 to be significantly longer (300 ms vs. 72 ms). Displacement PDF metrics from both ECS-weighted and ICS-weighted simulations correlated with each other and showed virtually no difference. This result suggests that the QSI displacement characteristics is dominated by the ICS signal not because it has a longer T_2, but rather because the ICS is more restricted than the ECS as it is believed (1). The histologic mean axon diameter was consistently larger than the simulated displacement PDF FWHM. It would be expected

that the simulated displacement PDF FWHM would be larger than the histologic mean axon diameter as it contains both ECS and ICS displacements. This discrepancy is probably due to uncertainties in the simulation parameters such as the ECS and ICS T_2 and permeability values.

3.4.3 Implications for QSI to assess axon morphology

Q-space simulations were used here to investigate several issues concerning the accuracy of QSI experiments to assess axon morphology. As axons are known to exhibit great variability in shape and size, it was not clear if the FWHM of the displacement PDF would still reflect MAD. Furthermore, given that there is signal in the ECS as well as the ICS, it was not clear if the ECS would contribute any axon morphology information in the displacement PDF. Simulations on synthetic axons helped address these questions and showed that despite variations in size and shape, the FWHM of the displacement PDF still correspond well with MAD. Additionally, the simulations demonstrated that the axon geometry information predominantly resides in the ICS signal – only the ICS displacement PDF FWHMs showed correspondence with MAD while the ECS displacement PDF FWHMs were much lower than MAD. This result suggests the need to separate the ICS and ECS signals to properly assess axon morphology.

The simulations on histologic images were used to investigate the implications of performing QSI on tissues with both ICS and ECS signals. The simulation parameters were carefully chosen to mimic actual experimental parameters (see Chapter 2). The diffusion time was relatively short (10 ms), the TE was short (17.4 ms) and the diffusion gradient duration was varied between 0.4 and 5 ms. One major question involves the

precise T_2 values for the ECS and ICS signals. Different literature sources can report longer T_2 values for ICS than ECS or vice versa (2). Simulations with ICS-weighted and ECS-weighted parameters helped study this question and showed that the displacement PDF did not change in either case most likely due to the short TE used. The simulations also showed that despite mixing ECS and ICS signals, the overall displacement PDF FWHM, ZDP and kurtosis showed excellent correlation with MAD calculated from histology. This suggests that, under the current experimental parameters, the ECS signal does not change appreciably with normal variances in axon morphology.

The main implication of these simulation results is that, under the current experimental parameters, in spite of variations in axon size and shape, the mixing of ECS and ICS signals, and variable T_2 and QSI may still provide measures of axon morphology that correlate well with the underlying architecture.

3.5 Conclusion

In this chapter, QSI simulations on both synthetic axons and histologic images were used to investigate the effects of having signal from both ECS and ICS and variability in cell size and shape on QSI measurements of axonal architecture. Each of these effects has important implications on the viability of QSI to assess axon morphology, but would have been difficult to study experimentally. Simulations provided a controllable environment to investigate each effect individually. The simulation results showed that despite all the variable and unknown effects, QSI may still provide accurate measures of axon morphology. The insights from these results support the potential of QSI to indirectly assess axonal architecture and will aid the understanding and

interpretation of the experimental results to be discussed in the following chapters. In particular, the simulations support the motivation to separate the ECS and ICS signals, perhaps using a two-compartment model, in order to remove the confounding effects of ECS diffusion.

3.6 Literature citations

1. Assaf, Y., et al., *New modeling and experimental framework to characterize hindered and restricted water diffusion in brain white matter.* Magn Reson Med, 2004. **52**(5): p. 965-78.
2. Peled, S., et al., *Water diffusion, T(2), and compartmentation in frog sciatic nerve.* Magn Reson Med, 1999. **42**(5): p. 911-8.
3. Hwang, S.N., et al., *An image-based finite difference model for simulating restricted diffusion.* Magn Reson Med, 2003. **50**(2): p. 373-82.
4. Chin, C.L., et al., *Assessment of axonal fiber tract architecture in excised rat spinal cord by localized NMR q-space imaging: simulations and experimental studies.* Magn Reson Med, 2004. **52**(4): p. 733-40.
5. Callaghan, P.T., *Pulsed-Gradient Spin-Echo NMR for Planar, Cylindrical, and Spherical Pores under Conditions of Wall Relaxation.* Journal of Magnetic Resonance, Series A, 1995. **113**(1): p. 53-59.

Chapter 4: Displacement PDF Method

4.1 Introduction

The displacement probability density function (PDF) method is the application of the basic q-space imaging (QSI) theory as outlined in Chapter 1. Due to the need for high displacement resolution while fulfilling the SGP approximation, a custom 50 T/m gradient coil was used for diffusion encoding. All data acquisition details were covered in Chapter 2. The displacement PDF method includes both one- and two-compartment approaches. The one-compartment method is just the standard QSI experiment. The two-compartment method is used to account for signal from extracellular (ECS) and intracellular (ICS) spaces. This allows for measurement of mean axon diameter (MAD) as well as ICS volume fraction and axon diameter distribution (ADD).

4.2 Methods

4.2.1 One-compartment displacement PDF method

All data analysis was performed in IDL (Interactive Data Language, Research Systems, Boulder, CO). As each image corresponded to a specific q-value, QSI data set can be thought of as a 3D matrix with two spatial and one q-value dimension. An echo attenuation plot for one pixel can be generated by selecting one location in the spatial dimensions and then recording the echo attenuation along the q-value dimension.

Once the single pixel echo attenuation plot was recorded, it was normalized to the maximum value at the zero q-value. In order to compute a purely real Fourier transform in accordance with Fourier transform theory, the echo attenuation plot was reflected about the origin (q = 0) to fill in the *negative* q-value, resulting in 127 total q-values (1

zero q-value, 63 positive, and 63 negative q-values). A displacement PDF was computed by applying a 1D Fourier transform to the modified echo attenuation plot. FWHM was measured with linear interpolation. After calculating the displacement PDFs for each pixel, FWHM, zero-displacement probability (ZDP), and kurtosis maps are generated.

In order to compare differences between WM tracts, a region-of-interest (ROI) analysis was performed on the FWHM, ZDP, and kurtosis maps. ROIs of 20 pixels were manually drawn in each of the seven WM tracts. ROI locations were chosen to match the histologic ROI location (as discussed below) as closely as possible. For each ROI, average q-space attenuation plots, displacement PDFs, FWHM, ZDP, and kurtosis values were recorded.

To investigate the effects of low displacement resolution, we took the existing experimental data, truncated the q-space dimension by retaining the first 16 q-values and setting the remaining 48 q-values to zero, and performed the same data processing described above. We chose to retain the first 16 q-values, because that seemed to be the limit below which we could no longer differentiate between WM tracts. Using only 16 q-values increased the displacement resolution from 0.6 to 2.4 μm.

4.2.2 Two-compartment displacement PDF method

Since the displacement PDF contains signal from both the ECS and ICS, separation of these signals may lead to a more accurate MAD estimate as well as provide a means to estimate the ECS and ICS volume fractions. In this method, as developed independently by Nossin-Manor *et al.* (1), the displacement PDFs were fit to a two-compartment model. As ECS and ICS diffusion is expected to be hindered and restricted,

respectively (2), their displacement PDFs would be a Gaussian and an autocorrelation of the axon geometry (see Chapter 1), respectively. MAD was then estimated from the ICS displacement PDF FWHM. ECS and ICS volume fractions were estimated by normalizing each displacement PDF area by the overall fit area (ECS plus ICS).

Fitting was done with a non-negative nonlinear minimization algorithm in Matlab (Mathworks, Natwick, MA, USA). To find the exact ICS displacement PDF shape, an image-based finite difference diffusion simulation program (3) was used to simulate the QSI echo attenuation based on WM tract histologic images as described in Chapter 3 (4). PDFs were simulated with signal only from the ICS (excluding myelin). The simulated PDFs were then fit to various peak shapes such as Gaussian, Lorentzian and others, and the goodness of fit was determined by the R^2 value.

4.2.3 Axon diameter distribution assessment with two-compartment displacement PDF method

Measuring the ADD with the displacement PDF method starts with calculating the displacement PDF from a single axon with radius r, $PDF(r)$, which, in the long diffusion time limit, is the auto-correlation function of the spin density (5) , $\rho_r(x)$:

$$PDF(r): PDF(R \mid \Delta \to \infty) = \int \rho_r(x - R)\rho_r(x)dx \tag{4.1}$$

By assuming the axon cross-section to be circular, $\rho_r(x)$, and thus $PDF(r)$, can be analytically computed by assuming constant spin concentration across the pore

$$\rho_r(x) = 2\sqrt{r^2 - x^2} \tag{4.2}$$

where r is the axon radius. ICS displacement PDF, PDF_{ICS}, can then be represented as

$$PDF_{ICS} = \sum_{r} P_{ADD}(r) \times PDF(r) \tag{4.3}$$

where the summation is over all axon radii, and $P_{ADD}(r)$ is the probability of having a axon with radius, r. $P_{ADD}(r)$ is just the normalized ADD. $PDF(r)$ can be computed for a circular axon with any radius. In order to calculate the ICS displacement PDF from Eq. 4.3, $P_{ADD}(r)$ must first be calculated from the ADD. Based on empirical observation (4, 6, 7), the ADD can be modeled as a gamma distribution:

$$P_{ADD}(r|\alpha,\beta) = \frac{r^{\alpha-1} e^{\frac{-r}{\beta}}}{\beta^{\alpha}\Gamma(\alpha)} \tag{4.4}$$

where $\Gamma(\alpha)$ is the gamma function

$$\Gamma(\alpha) = \int_{0}^{\infty} e^{-t} t^{\alpha-1} dt \tag{4.5}$$

Eq. 4.4 is incorporated into Eq. 4.3 and the α and β parameters of the gamma distribution are fitted to the ICS displacement PDF using a nonlinear least-squares Matlab algorithm. The α and β parameters were then optimized so the calculated ADD had the same MAD as measured from the FWHM of the ICS displacement PDF as described in Chapter 4.2.2 using an unconstrained nonlinear optimization Matlab algorithm. Finally, any value of the fitted ADD that was less than 0.0001 was set to zero. This was done as the ADD from histology sometimes had zero values beyond a given axon diameter whereas the gamma distribution only asymptotically approaches zero with increasing axon diameter.

In order to investigate the validity of modeling the ADD as a gamma distribution, several ADDs measured with histology from different WM tracts were directly fit with a gamma distribution again using a nonlinear least-squares Matlab algorithm. Again, any

value of the fitted ADD that was less than 0.00001 was set to zero. The coefficient of determination (R^2) was calculated to assess the goodness of fit. Furthermore, in order to statistically compare the fitted gamma distribution and the histologic ADD, a two-sample Kolmogorov-Smirnov test (8), implemented in Matlab, was used. The null hypothesis here is that the two distributions are from the same continuous distribution. This test calculates the empirical cumulative distribution function (CDF) of each distribution and uses the greatest difference between the two CDFs as its test statistic to determine whether or not to reject the null hypothesis. The Kolmogorov-Smirnov test and coefficient of determination were also used to compare the ADDs fit from Eq. 4.3 and 4.4 with the ADD measured from histology.

4.3 Results

4.3.1 One-compartment Displacement PDF method

Figure 4.1 shows typical magnitude images acquired with different q-values. Note the inversion in contrast between WM and GM due to the restriction of water diffusion in WM at the higher q-value. SNR values, calculated as the ratio of the mean value of an ROI in the dorsal column divided by the mean value of an ROI in the background, were 60 and 2 for q = 0 μm^{-1} q_{max} = 0.82 μm^{-1}, respectively.

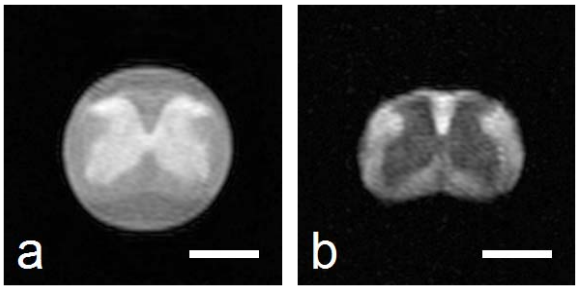

Figure 4.1. Sample magnitude images at two different q-values with Δ/δ = 10/0.4 ms: 0 and 0.12μm^{-1}. The white bar represents 1 mm. Note the fluid surrounding the spinal cord, which exhibits free diffusion, is attenuated to background intensity in (b).

In the following images, the same color scale was used to highlight differences observed under different experimental conditions. Figure 4.2 shows typical q-space echo attenuations and displacement PDFs for various WM tract ROIs, displacement PDF FWHM, ZDP, and kurtosis maps for one specimen for varying experimental parameters. Note the clear discrimination of WM tracts on the FWHM, ZDP, and kurtosis maps under conditions of high displacement resolution and fulfilling the SGA approximation (Figure 4.2a). However, failure to fulfill the SGA approximation (Figure 4.2b), increased ZDP and kurtosis while decreasing FWHM, as predicted. When simulating low displacement resolution (Figure 4.2c), the displacement PDFs exhibited severe ringing due to zero-filling.

As discussed in Chapter 2, Figure 4.3 illustrates the variation in MAD that occurred across a 1 mm slice. Figure 4.3a shows, for one specimen, the calculated MAD of seven WM tract ROIs from six equally spaced sections spanning 1 mm. Figure 4.3b compares the MADs for each WM tract averaged over all six sections with parameters derived from QSI and histology. There was significant correlation between the average axon diameters calculated from all six sections and displacement PDF FWHM (R^2 = 0.86, p = 0.0025, slope = 0.86), average axon diameters calculated from one section and

---

Figure 4.2 (next page). Sample q-space echo attenuation plots and displacement PDFs for seven WM tract ROIs, alongside with sample FWHM, ZDP, and kurtosis maps under experimental parameters with (a) high displacement resolution (q_{max}=0.82μm^{-1}) and fulfilling the narrow gradient pulse condition (Δ/δ=10/0.4 ms), (b) high displacement resolution (q_{max}=0.82μm^{-1}) and failing to fulfill the narrow gradient pulse condition (Δ/δ=10/5 ms), and (c) low displacement resolution (q_{max}=0.21μm^{-1}) and failing to fulfill the narrow gradient pulse condition (Δ/δ=10/5 ms). The fourth case of low displacement resolution (q_{max}=0.21μm^{-1}) and fulfilling the narrow gradient pulse condition (Δ/δ=10/0.4 ms) was excluded to its similarity with (c).

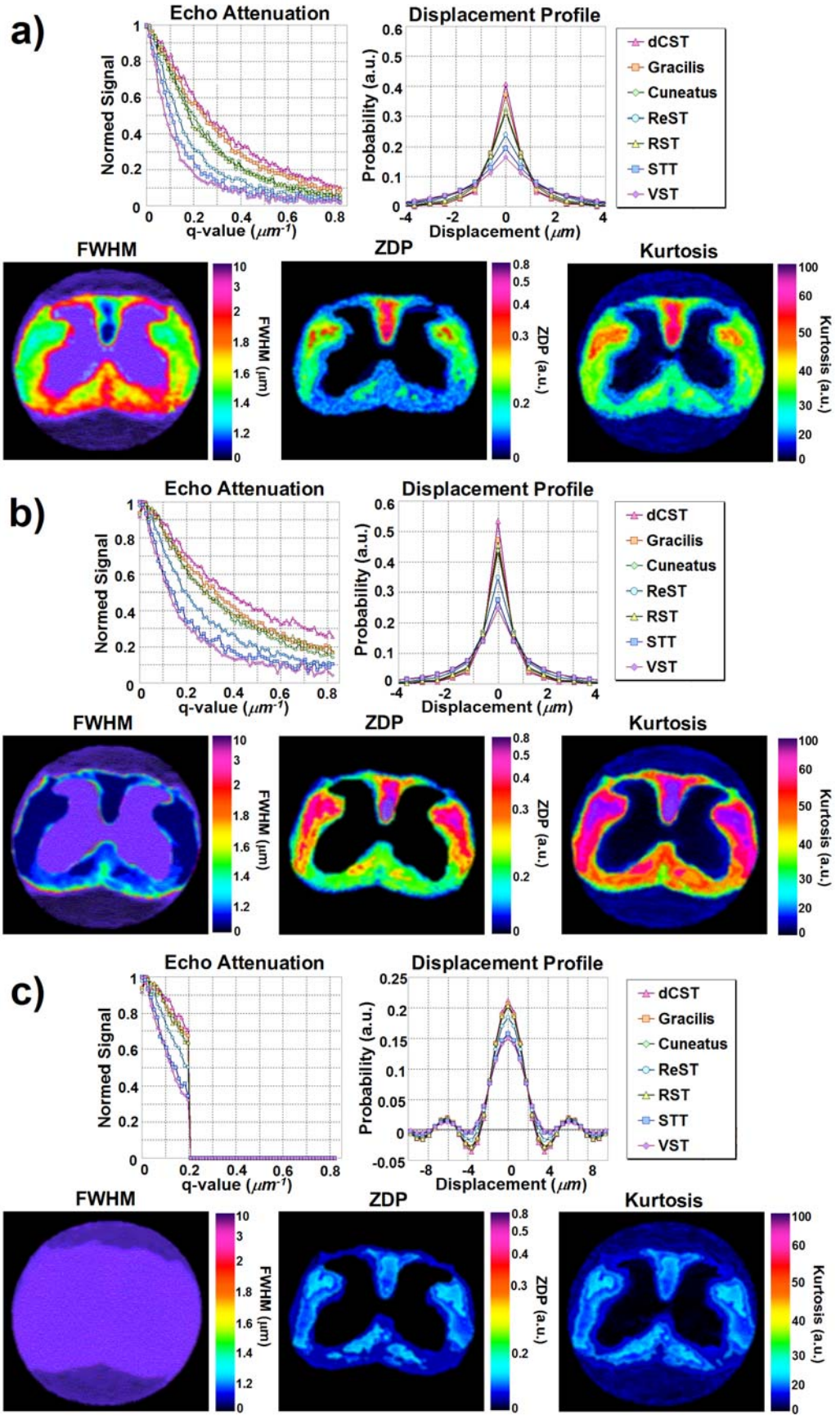
a)
Echo Attenuation
Normed Signal
q-value (μm⁻¹)
Displacement Profile
Probability (a.u.)
Displacement (μm)
dCST
Gracilis
Cuneatus
ReST
RST
STT
VST
FWHM
FWHM (μm)
ZDP
ZDP (a.u.)
Kurtosis
Kurtosis (a.u.)
b)
Echo Attenuation
Normed Signal
q-value (μm⁻¹)
Displacement Profile
Probability (a.u.)
Displacement (μm)
dCST
Gracilis
Cuneatus
ReST
RST
STT
VST
FWHM
FWHM (μm)
ZDP
ZDP (a.u.)
Kurtosis
Kurtosis (a.u.)
c)
Echo Attenuation
Normed Signal
q-value (μm⁻¹)
Displacement Profile
Probability (a.u.)
Displacement (μm)
dCST
Gracilis
Cuneatus
ReST
RST
STT
VST
FWHM
FWHM (μm)
ZDP
ZDP (a.u.)
Kurtosis
Kurtosis (a.u.)

displacement PDF FWHM (R^2 = 0.95, p = 0.0002, slope = 0.76), and the average axon diameters calculated from all six sections and average axon diameters calculated from one section (R^2 = 0.92, p = 0.0006, slope = 0.81). The data therefore shows that the axonal structure is maintained over our imaging slice thickness and that a histologic section is representative of the average structure.

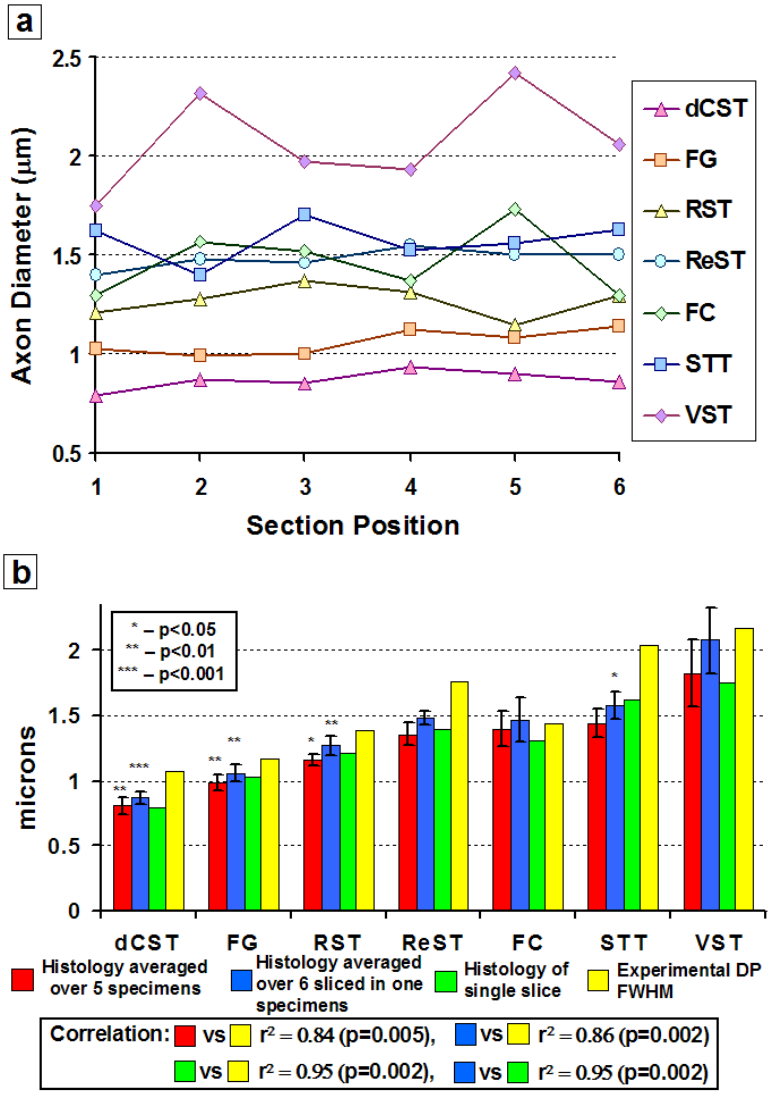

Figure 4.3. (a) Calculated MAD from 7 WM tract ROIs from 6 equally spaced sections spanning 1 mm. (b) WM tract MAD calculated from 5 specimens, the WM tract MAD calculated from all six sections in one specimen, the WM tract MAD calculated from one section from the same specimen, and the measured FHWM of the displacement PDF (DP) from the same specimen. Each asterisk represents the p-value of a paired t-test comparison with the next similar colored bar to the right.

Figure 4.4 shows experimental data for each WM tract averaged over all five specimens under experimental conditions fulfilling and not fulfilling the SGA approximation, as a function of displacement resolution. Note again that FWHM increases, and ZDP and kurtosis decrease with increasing mean axon diameter in all plots. Under conditions fulfilling the SGA approximation and high displacement resolution, there was positive correlation between MAD calculated from histology and FWHM ($R^2 = 0.95$, $p = 0.0002$, slope = 1.02). Negative correlations were found between MAD and ZDP ($R^2 = 0.89$, $p = 0.0015$, slope = -0.22) and kurtosis ($R^2 = 0.91$, $p = 0.0009$, slope = -38). The correlations remained significant, albeit less strong, under conditions not fulfilling the SGA approximation and low displacement resolution.

To the best of our knowledge, our QSI results are the first with a displacement resolution low enough to resolve axon diameters while fulfilling the SGA approximation. The displacement PDF metrics correlated well with the axon diameters measured from histology, suggesting that the echo attenuation is dominated by the ICS signal. It is noted that the displacement PDF FWHMs were generally larger than the measured axon diameters (0.27±0.07 μm under ideal conditions of high displacement resolution and fulfilling the SGA approximation), which may be a consequence of several factors (see Discussion).

4.3.2 Two-compartment displacement PDF method

Figure 4.5a shows a simulated PDF from only the histologic ICS region used for the displacement PDF method. The peak shape of the ICS displacement PDF was determined empirically by fitting the simulated PDFs from above to various peak shapes

(e.g. Gaussian, Lorentzian, etc.). As shown in Figure 4.5a, the peak shape that gave the best fit as determined by the R^2 value was a decaying exponential reflected about the

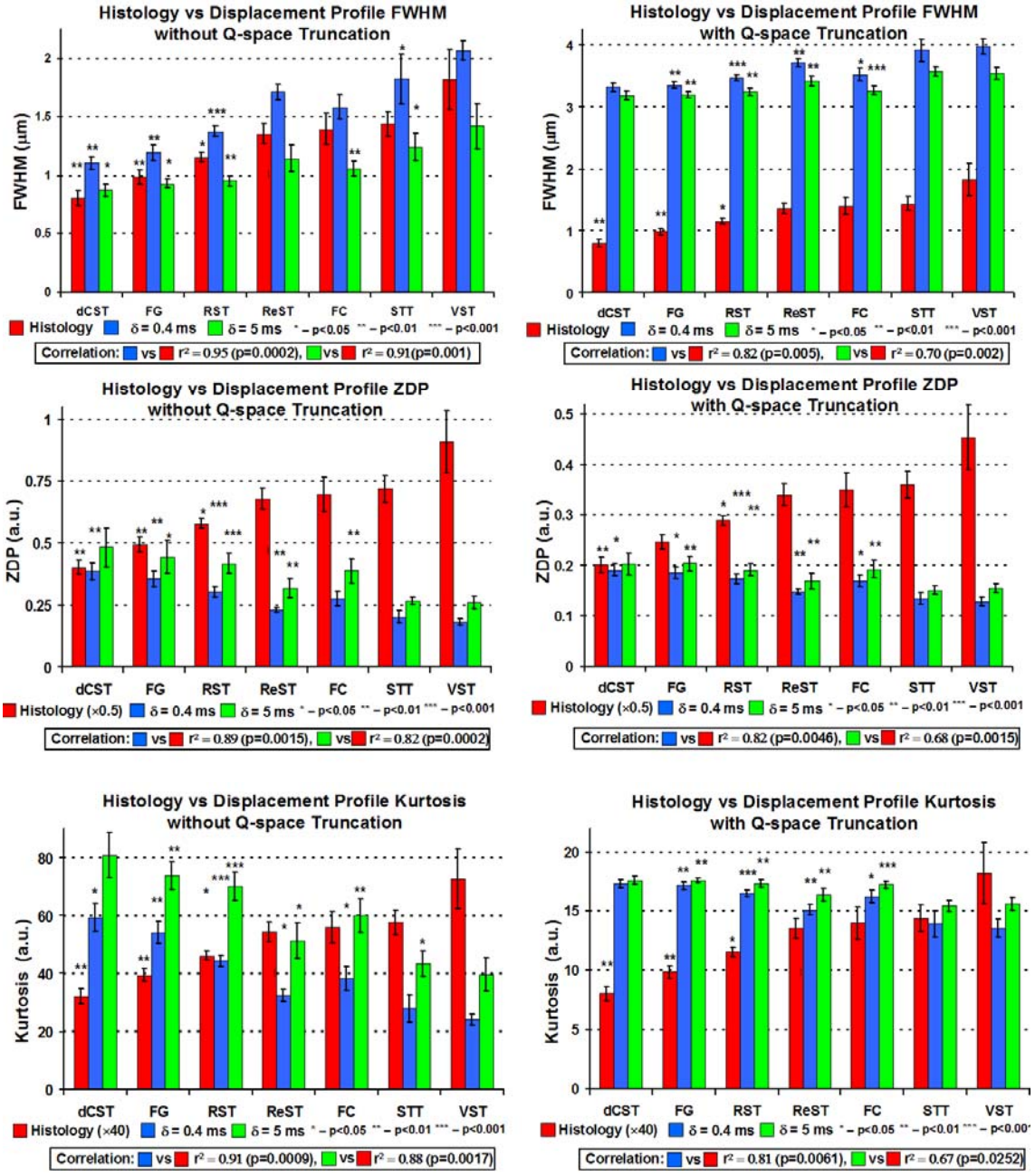

Figure 4.4. Summary plots of q-space experiments showing MAD calculated from histology, FHWM, ZDP, and kurtosis values for each WM tract averaged over all five specimens under experimental conditions fulfilling and not fulfilling the SPG approximation and with and without q-space truncation (to simulate low displacement resolution). Each asterisk represents the p-value of a paired t-test comparison with the next similar colored bar to the right.

origin (R^2>0.99). Figure 4.5b shows sample experimental displacement PDFs fitted to a weighted sum of Gaussian and decaying exponential. Figure 4.5c shows a plot of average WM tract MAD calculated from histology versus average experimental FWHM of ICS displacement PDFs. A Bland-Altman plot (not shown) yielded a 95% confidence interval from –0.07 to 0.03 μm. Also shown in Figure 4.5c is the ICS volume fraction calculated from both histology and experiments averaged over all specimens. An ANOVA analysis determined that there was no significant difference in histologic ICS volume fraction among WM tracts. Therefore, a single ICS volume fraction was calculated for each specimen by averaging over each WM tract. There was no correlation between ICS volume fractions measured from histology and the displacement PDF method. No significant correlation was found between the ECS displacement PDF FWHM and histologic MAD, and the average FWHM of the ECS displacement PDF was 4.5±2.1 μm.

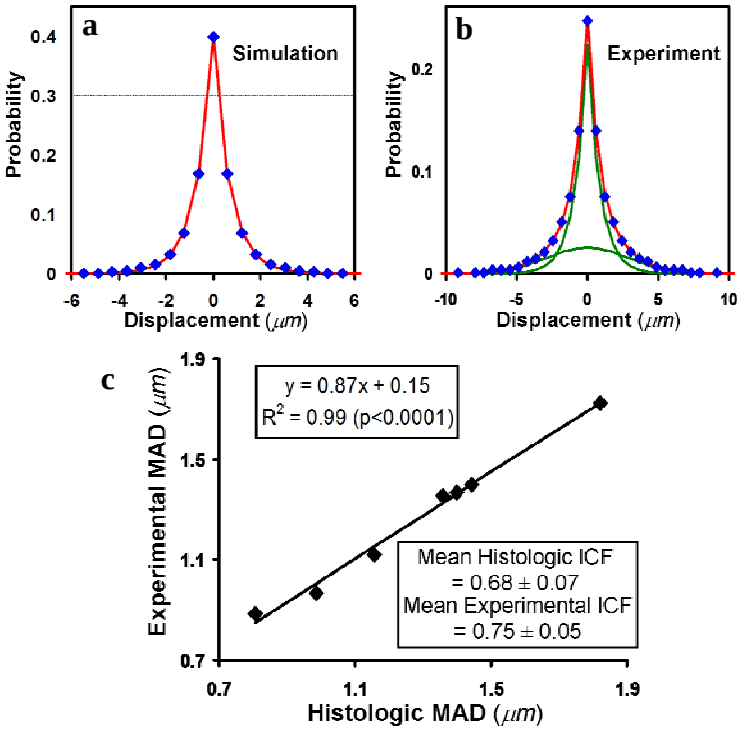

Figure 4.5. (a) Sample simulated PDF on histologic ICS region only (blue points) with exponential decay peak fit (red line) to determine ICS displacement PDF shape. All fits had R^2>0.99. (b) Sample experimental PDF (blue points) with overall fit (red line) and ECS and ICS displacement PDF fit (green lines). All fits had R^2>0.99. (c) Plot of WM tract histologic vs. experimental MADs with equation of the line of best fit and mean ICS volume fraction values.

4.3.3 Axon diameter distribution assessment with two-compartment displacement PDF method

Figure 4.6 shows ADDs measured with histology selected from seven WM tracts directly fit with a gamma distribution. The WM tract ADDs are ordered from smallest MAD (dCST, 0.81±0.06 μm) to largest (VST, 1.73±0.21 μm). The fitted gamma distribution plots show excellent correspondence with the histologic ADDs from the calculated coefficient of determination, R^2 >0.95. Only the VST tract had a lower R^2 of 0.76. The two-sample Kolmogorov-Smirnov test p-values calculated between each histologic ADD and fitted gamma distributions are also show in Figure 4.6. All p-values are greater than 0.05, which suggests that the fitted gamma distributions and histologic ADDs are not statistically distinct. These results indicate that the underlying ADD in healthy WM tracts is well modeled by a gamma distribution.

Figure 4.7 shows ADDs measured from histology and QSI averaged over 5 mice for all WM tracts. Again, the WM tract ADDs are ordered from smallest to largest MAD (dCST, 0.81±0.06 μm) to largest (VST, 1.73±0.21 μm). The QSI-derived ADDs all have MADs matching values measured with the two-compartment displacement PDF method (see 4.3.2). From the histologic ADDs, it is clear that there is a gradual trend of increasing variation in axon diameter with increasing MAD. The QSI-derived ADDs show good agreement with histologic ADDs with R^2 values greater than 0.8. Again, the VST tract had the lowest R^2 of 0.77. The two-sample Kolmogorov-Smirnov test p-values calculated between each histologic ADD and fitted gamma distributions are also show in Figure 4.7. All p-values are greater than 0.05, which suggests that the QSI-derived and histologic ADDs are from the same distribution.

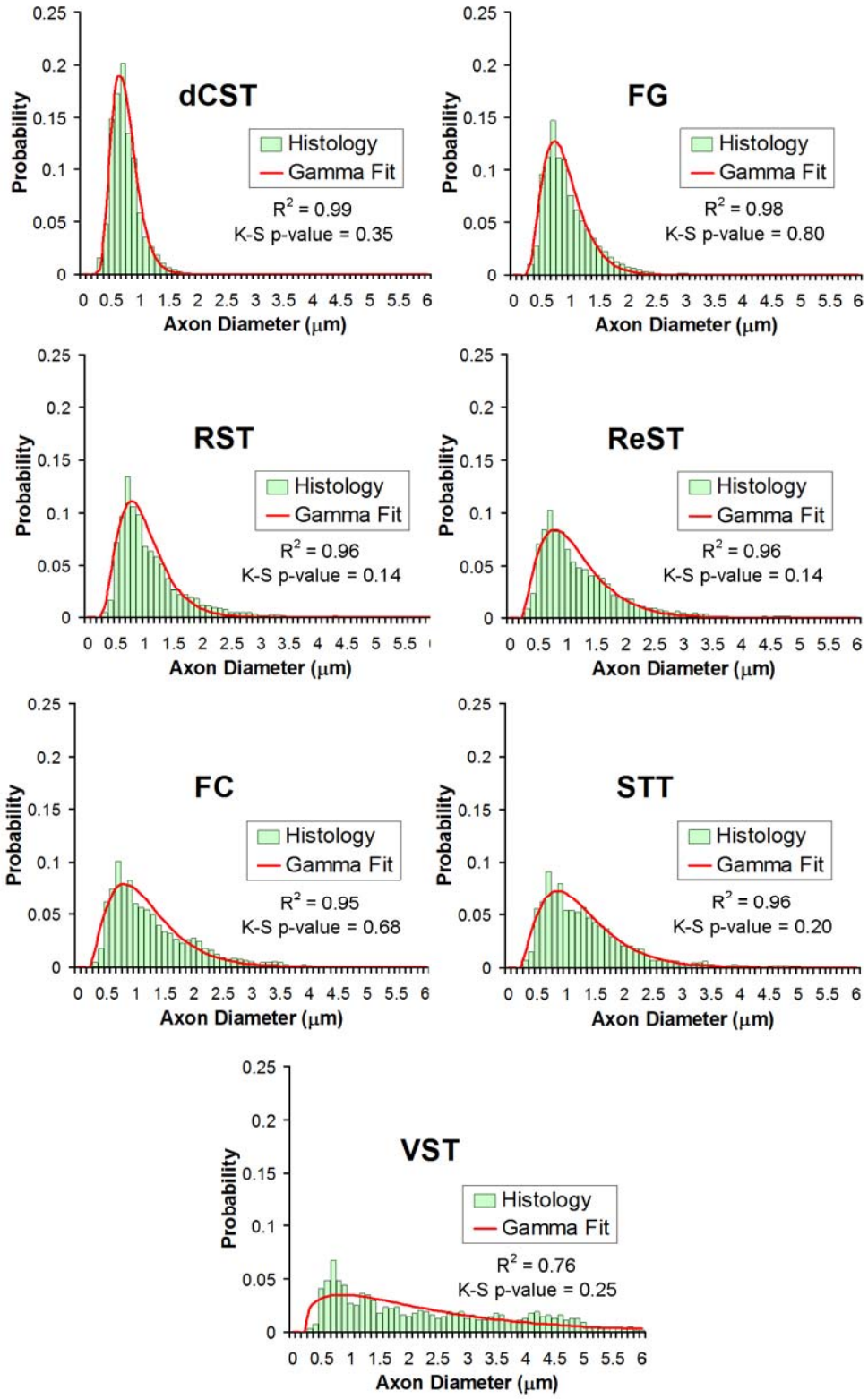

Figure 4.6. Plots of ADD measured with histology (green bars) from select individual WM tracts fit directly with a gamma distribution (red line). R^2 and Kolmogorov-Smirnov test p-values are shown for each WM tract.

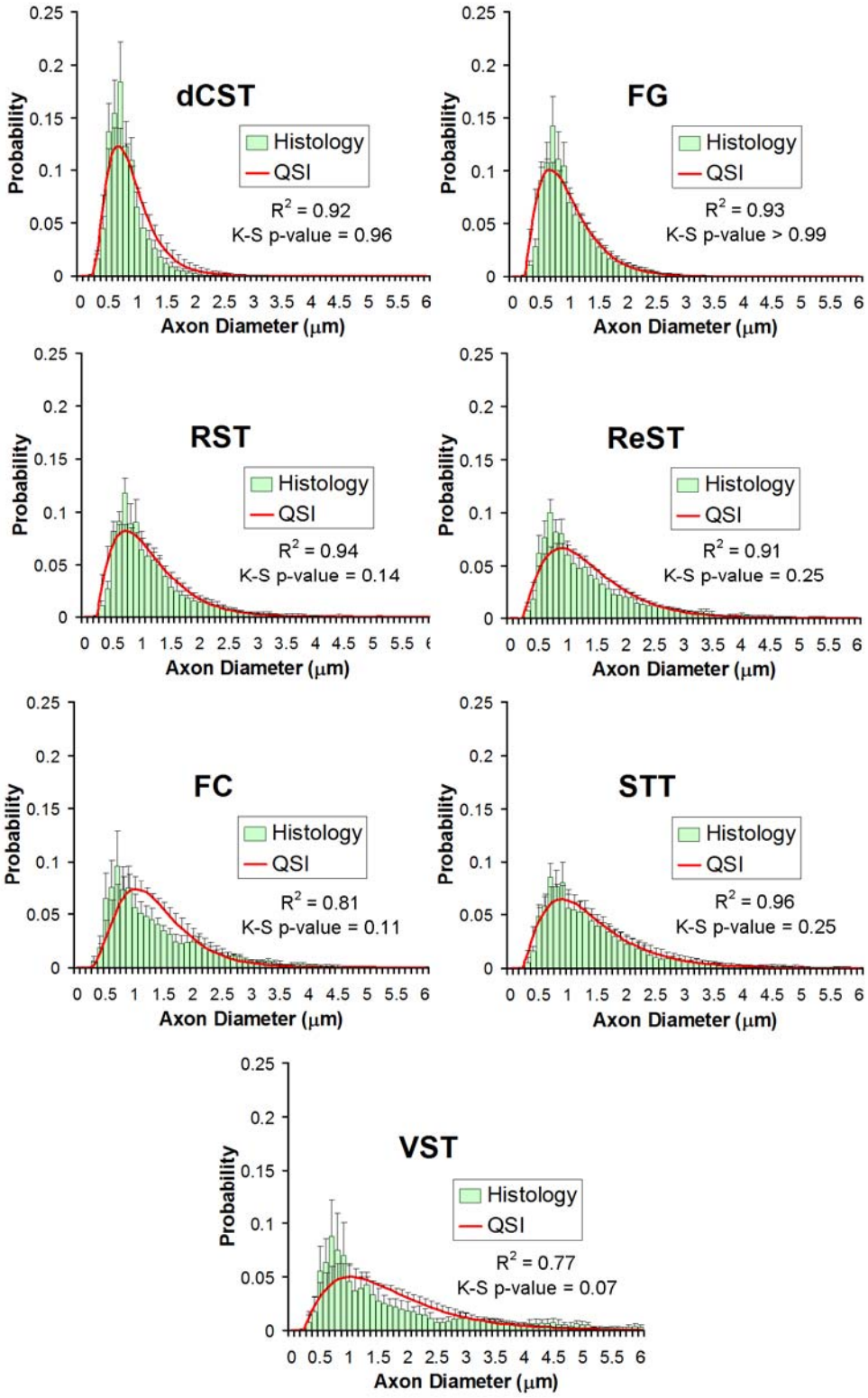

Figure 4.7. Plots of ADD measured with histology (green bars) and QSI (red line) for all WM tracts. All ADDs were averaged over 5 mice and the standard deviation bars are shown. R^2 and Kolmogorov-Smirnov test p-values are shown for each WM tract.

4.4 Discussion

4.4.1 One-compartment displacement PDF method

In highly regular porous structures, such as packed beads, the echo attenuation will exhibit diffraction peaks and pore geometry information can be directly read from the peaks (9). However, diffraction patterns in biological systems have only been observed in packed erythrocytes and not in tissues such as multi-axonal systems, possibly due to structural heterogeneity as our simulations suggest. Nevertheless, the displacement PDF has provided insight into axonal architecture (10-12). It is important to consider that the displacement PDF is an empirical measurement. In order to interpret the features of the displacement PDF, one must compare it with the underlying tissue structure as seen with histology in order to understand how the structure impedes water diffusion.

Even though the one-compartment approach did not separate ECS and ICS signals, our results showed excellent agreement with MAD calculated from histology. The displacement PDF FWHMs overestimated the MADs by about 20% under optimal experimental conditions with respect to histology, except for the case of failing to fulfill the SGA approximation with high displacement resolution in which the FWHM is artifactually narrowed. Such an overestimation may result from insufficient displacement resolution. Our displacement resolution was 0.6 μm compared to axon diameters of 0.81-1.82 μm.

Examination of the displacement PDFs with high displacement resolution and fulfilling the SGA approximation shows that the central peak is, in most WM tracts, described by about five points and the true displacement PDF shape may be hidden. The linear interpolation used to calculate the FWHM may not represent the true FWHM.

Another possibility is that ECS diffusion, which is assumed to be Gaussian (2), may broaden the displacement PDFs as it is a superposition of both the ECS and ICS displacement PDFs due to the linearity of the Fourier transform (10). Furthermore, while membrane and myelin permeability will lead to a broader FWHM, there is evidence to suggest that exchange between the ECS and ICS compartments is virtually non-existent at the diffusion time of 10 ms (13, 14). Our previous simulations on histologic images (15) indicated that the displacement PDF FWHM remained stable over the range of permeability values reported for lipid bilayers (16).

Other investigators have used the root-mean-squared (RMS) displacement instead of the displacement PDF FWHM to estimate MAD (12, 17, 18). The RMS displacement is calculated easily from the displacement PDF FWHM by multiplying it by a factor of 0.425 (19). However, this calculation is only valid under Gaussian diffusion. Following from our previous work (10), we use only the FWHM to estimate the mean axon diameter because the ICS water should be restricted (i.e. non-Gaussian) at our diffusion time.

4.4.2 Two-compartment displacement PDF method

The excellent correlation between histologic and experimental MAD (Figure 4.5c) and the Bland-Altman results suggest good agreement between MAD measured with histology and the displacement PDF method. Compared with the one-compartment results where ECS and ICS signals were not separated, MAD estimates from the displacement PDF method better match those measured by histology. In addition, while there was no correlation between histologic and experimental ICS volume fractions, both values averaged across specimens fall within the range of 60-80% reported for the rat

corpus callosum (20). Furthermore, MAD estimates from the displacement PDF method were within 4% of histologic MAD. Finally, the average ECS displacement PDF FWHM is below the expected RMS displacement of free water with a diffusion time of 10 ms.

It should be noted that there is an apparent inconsistency in how the ICS volume fraction and MAD were calculated from histology; the myelin area was included in the calculation of ICS volume fraction, but not for MAD. The decision to include or exclude myelin was motivated by differences in the distance between diffusion barriers in the ICS and myelin spaces.

In ICS, the distance between diffusion barriers would be the diameter of the axon, excluding myelin. In myelin, the distance between diffusion barriers would be the spacing between the lipid bilayers (<0.1μm). At sufficiently long diffusion times, both ICS and myelin are expected to exhibit restricted diffusion. Since the ICS displacement PDF results from molecules exhibiting restricted diffusion in the proposed model, it should reflect contributions from water diffusion in myelin. Therefore, for accurate comparison with the displacement PDF results, the ICS volume fraction measured from histology was defined as the sum of the ICS and myelin areas.

However, as the spacing between the lipid bilayers in myelin is <0.1μm, our displacement PDF resolution is not high enough to resolve the restricted diffusion in the myelin and the FWHM may primarily reflect ICS. Therefore, for proper comparison with the results from the displacement PDF method, histology-derived MAD was computed by excluding the myelin region. The inadequate displacement resolution may also explain the discrepancies between the ICS volume fraction measured with the displacement PDF method and histology.

As previously mentioned, Nossin-Manor *et al.* (1) also used a two-compartment model to analyze QSI data. Displacement PDFs measured from excised rat spinal cords were fitted to a bi-Gaussian model to characterize fast and slow diffusion components. When the diffusion gradients were applied perpendicular to the long axis of the spinal cord, the mean displacements measured from both the slow component of the bi-Gaussian model and the basic single-component QSI analysis exhibited restricted diffusion behavior and were in good agreement with each other. The authors concluded that the basic single-component QSI experiment described water diffusion perpendicular to the WM tract nearly as well as the two-compartment model, which conflicts with the results reported here. Several factors can help explain this discrepancy. First, the displacement resolution was only 3.9 μm in Nossin-Manor et al compared with 0.6 μm in the work reported here. Since axon diameters are on the order of 1-2 μm, the low displacement resolution found in Nossin-Manor may have blurred the discrimination between diffusion in the ECS and ICS. Second, the diffusion time in Nossin-Manor *et al.* is much longer than the one used here (50-250 versus 10 ms). Thus, the longer diffusion time may emphasize the ICS signal through the greater attenuation of the ECS signal due to unrestricted diffusion. Third, Nossin-Manor *et al.* assumed a bi-Gaussian model, whereas only the ECS displacement PDF was modeled as a Gaussian in the work here. The ICS displacement PDF is the auto-correlation function of the pore geometry that, as our simulations suggest, is not Gaussian. While Nossin-Manor *et al.* reached different conclusions, differences in data acquisition and analysis do not make their results inconsistent with those reported here.

4.4.3 Axon diameter distribution assessment with two-compartment displacement PDF method

The QSI-derived ADD assessment is a direct extension of the two-compartment displacement PDF method discussed above. The two-compartment displacement PDF method is first used to separate the ICS and ECS displacement PDFs and to estimate MAD from the FWHM of the ICS displacement PDF. Only by isolating the ICS displacement PDF can the effect of axon diameter variation be properly taken into account. The MAD constraint in the fitting algorithm was necessary to obtain good agreement between QSI-derive and histologic ADDs. Without it, the algorithm produced ADDs that consistently overestimated the probability of axons with larger diameters, which broadened the distribution. As a result, the calculated ADD would have a larger MAD. By fixing the MAD of the distribution to be the measured MAD from the two-compartment displacement PDF method, the algorithm produced a narrower ADD that better matched the ADDs measured from histology. This was viewed as a reasonable constraint as it was demonstrated above (see 4.3.2) that the two-compartment displacement PDF method accurately measured MAD as compared with histology (21).

The approach to assessing ADD shown here stands in contrast to the AxCaliber method (6), but there are several similarities. Both methods require separation of the ECS and ICS signals and assume circular axon cross-section geometry and an underlying gamma distributed ADD. Assuming a simple geometry for the axon cross-section allows one to directly calculate the contribution to the overall signal or PDF by an axon with a given diameter. Note that AxCaliber simultaneously extracts MAD and ADD, while the QSI method first measures MAD and then computes ADD using the measured MAD as a

constraint. Furthermore, while the AxCaliber method operates in q-space, the QSI method presented here operates in displacement space. As q-space and displacement space are Fourier transforms of one another, it is perhaps not surprising that both methods produce ADDs that agree well with histology, which highlights the potential for q-space diffusion MRI to indirectly assess axon morphology.

The QSI-derived ADDs showed excellent agreement with histology and were shown not to be statistically different from histologic ADDs, which indicates the potential for quantitative assessment of ADD. Moreover, QSI-derived ADDs consistently show the relative differences in ADD between WM tracts. The fact that this method was sensitive to the subtle increase in the spread of ADD with increasing MAD suggests that detecting changes in ADD may be possible. Nevertheless, the QSI-derived ADDs still show systematic differences with histologic ADDs, which primarily is the underestimation of the probability of axon with diameters less than 1 μm. This may be the result of errors in the assumptions of this method, namely circular axon geometry and a gamma distributed ADD.

The validity of assuming an underlying gamma distributed ADD was, for the first time, investigated in this work. It was shown that a gamma distribution describes the shape of the histologic ADD accurately and that the two distributions were statistically indistinguishable. This suggests that any discrepancies between the QSI-derived and histologic ADDs were likely from errors in the circular axon geometry assumption. Certainly histology shows that axons do not have a simple circular geometry. This may explain the need to constrain MAD in the fitting algorithm, because the PDF from a circular axon does not accurately represent the true PDF from an axon. While circular

axon geometry has been used successfully in other models such as AxCaliber and CHARMED (2, 6), the role of axon shape in assessment of ADD requires further investigation beyond the scope of this dissertation. It should be noted that these results are limited to healthy WM tracts. There is no expectation that the ADD will remain gamma distributed under pathologic conditions. This suggests the need for a non-parametric approach for estimating ADD, which is under current investigation.

4.5 Conclusions

The work presented here demonstrates the advantage of having sufficient displacement resolution for QSI experiments. The one-compartment method approach was able to differentiate between WM tracts based only on MAD, although MAD was overestimated by approximately 20%. The two-compartment method separated the ECS and ICS displacement PDF and was able to measure MAD as accurately as compared to histology. It also allowed for measurement of ICS volume fraction and ADD, which provide additional information on axon morphology. The accuracy of these measurements is dependent on fulfilling the SGP approximation. Results from increasing the diffusion gradient duration show a narrowing of the displacement PDF as predicted from theory.

4.6 Literature citations

1. Nossin-Manor, R., R. Duvdevani, and Y. Cohen, *Effect of experimental parameters on high b-value q-space MR images of excised rat spinal cord.* Magn Reson Med, 2005. **54**(1): p. 96-104.
2. Assaf, Y., et al., *New modeling and experimental framework to characterize hindered and restricted water diffusion in brain white matter.* Magn Reson Med, 2004. **52**(5): p. 965-78.
3. Hwang, S.N., et al., *An image-based finite difference model for simulating restricted diffusion.* Magn Reson Med, 2003. **50**(2): p. 373-82.
4. Ong, H.H., et al., *Indirect measurement of regional axon diameter in excised mouse spinal cord with q-space imaging: simulation and experimental studies.* Neuroimage, 2008. **40**(4): p. 1619-32.
5. Callaghan, P., *Principles of Nuclear Magnetic Resonance Microscopy*. 1993, New York: Oxford University Press.
6. Assaf, Y., et al., *AxCaliber: a method for measuring axon diameter distribution from diffusion MRI.* Magn Reson Med, 2008. **59**(6): p. 1347-54.
7. Barazany, D., P.J. Basser, and Y. Assaf, *In vivo measurement of axon diameter distribution in the corpus callosum of rat brain.* Brain, 2009. **132**(Pt 5): p. 1210-20.
8. Hollander, M. and D.A. Wolfe, *Nonparametric Statistical Methods.* 1999, Wiley-Interscience: New York.
9. Callaghan, P.T., et al., *Diffraction-like effects in NMR diffusion studies of fluids in porous solids.* Nature, 1991. **351**: p. 467-469.

10. Chin, C.L., et al., *Assessment of axonal fiber tract architecture in excised rat spinal cord by localized NMR q-space imaging: simulations and experimental studies.* Magn Reson Med, 2004. **52**(4): p. 733-40.

11. King, M.D., et al., *Localized q-space imaging of the mouse brain.* Magn Reson Med, 1997. **38**(6): p. 930-7.

12. Assaf, Y., A. Mayk, and Y. Cohen, *Displacement imaging of spinal cord using q-space diffusion-weighted MRI.* Magn Reson Med, 2000. **44**(5): p. 713-22.

13. Meier, C., W. Dreher, and D. Leibfritz, *Diffusion in compartmental systems. II. Diffusion-weighted measurements of rat brain tissue in vivo and postmortem at very large b-values.* Magn Reson Med, 2003. **50**(3): p. 510-4.

14. Sehy, J.V., et al., *Importance of intracellular water apparent diffusion to the measurement of membrane permeability.* Biophys J, 2002. **83**(5): p. 2856-63.

15. Ong, H.H., et al. *Q-Space Simulations on Mouse Spinal Cord White Matter Tract Histologic Images*. in *Proceedings of ISMRM 14th Scientific Meeting*. 2006. Seattle, USA.

16. Disalvo, E.A., *Permeability and Stability of Lipid Bilayers*. 1995, London: CRC Press.

17. Assaf, Y., et al., *High b-value q-space analyzed diffusion-weighted MRI: application to multiple sclerosis.* Magn Reson Med, 2002. **47**(1): p. 115-26.

18. Biton, I.E., et al., *Improved detectability of experimental allergic encephalomyelitis in excised swine spinal cords by high b-value q-space DWI.* Exp Neurol, 2005. **195**(2): p. 437-46.

19. Cory, D.G. and A.N. Garroway, *Measurement of translational displacement probabilities by NMR: an indicator of compartmentation.* Magn Reson Med, 1990. **14**(3): p. 435-44.

20. Sykova, E. and C. Nicholson, *Diffusion in brain extracellular space.* Physiol Rev, 2008. **88**(4): p. 1277-340.

21. Ong, H.H. and F.W. Wehrli, *Quantifying axon diameter and intra-cellular volume fraction in excised mouse spinal cord with q-space imaging.* Neuroimage, 2010. **51**(4): p. 1360-6.

Chapter 5: Low q-value Method

5.1 Introduction

The low q-value method was developed to address the need for q-space imaging (QSI) to have sufficient displacement resolution for accurate measurements of axon morphology like mean axon diameter (MAD) as demonstrated in Chapter 4. The need for high resolution coupled with the need to fulfill the short gradient pulse (SGP) approximation necessitates the use of large gradient amplitudes that are not commercially available. The method presented here attempts to characterize axon morphology from the echo attenuation, E(q), at low q-values instead of from the displacement probability density function (PDF). By only acquiring data at low q-values, the need for large gradient amplitudes can be avoided. Similar to the displacement method, a two-compartment model is applied to account for diffusion in both the extracellular (ECS) and intracellular (ICS) spaces. All acquisition parameters are described in Chapter 2 and only details related to this method specifically are described here.

5.2 Methods

As mentioned in Chapter 1, architecture information of pore systems can also be obtained from diffraction patterns in the echo attenuation. Although WM is too heterogeneous to observe diffraction patterns in q-space (1), the MAD can be estimated from the initial decay of the echo attenuation. From a series expansion of the Fourier transform relationship, the initial echo attenuation at low q-values at a given diffusion time, Δ, where $q << MAD^{-1}$, can be expressed as

$$E(q,\Delta) = \exp\left(-2\pi^2 q^2 Z_{RMS}^2\right) \tag{5.1}$$

where Z_{RMS} is the root-mean-squared (RMS) displacement during the diffusion time, i.e. the width of the displacement PDF (2-4). As long as the SGP approximation ($\delta << \Delta$) is fulfilled, Z_{RMS} may be used as an estimate of MAD by fitting the initial echo attenuation decay to Eq. 1. However, the q-space echo attenuation is comprised of both ECS and ICS signals. Similar to the displacement PDF method, a two-compartment version of Eq. 5.1 could be used to account for the ECS and ICS signals:

$$E(q,\Delta) = f_{ECS} \exp\left(-2\pi^2 q^2 Z_{ECS}^2\right) + f_{ICS} \exp\left(-2\pi^2 q^2 Z_{ICS}^2\right) \quad (5.2)$$

where f_{ECS} and f_{ICS} are the relaxation-weighted ECS and ICS volume fractions and Z_{ECS} and Z_{ICS} are the RMS displacements of diffusing molecules in the ECS and ICS.

Echo attenuations were fit to both Eq. 5.1 and 5.2 with a nonlinear minimization algorithm in Matlab (Mathworks, Natwick, MA, USA). Two sets of echo attenuations were processed. One was acquired with a diffusion gradient duration of 0.4 ms in order to fulfill the SGP approximation. The other was acquired with a diffusion gradient duration of 5 ms in order to investigate the effects of not fulfilling the SGP approximation on the low q-value method. When fitting to Eq. 5.2, the following parameter constraints were applied: $f_{ECS} + f_{ICS} = 1$ and $Z_{ECS} < 8\mu m$ (as RMS displacement in ECS cannot be larger than that of free water). WM tract MAD previously estimated from histology (Chapter 2) were used to identify the low q-value regime by only fitting E(q) at $q < (MAD^{-1})/10$ (the first 11 to 5 q-values for the smallest to largest WM tract MAD, respectively). MAD, and ECS and ICS volume fractions were then estimated from Z_{ICS}, f_{ECS} and f_{ICS}, respectively.

5.3 Results

Figure 5.1 shows data acquired with a diffusion gradient duration of 0.4 ms. Figure 5.1a shows sample fits of experimental data with Eq. 5.1 and 5.2 using the low q-value method. Figure 5.1b shows a plot of experimental MAD estimated from one- and two-compartment fits (Z_{RMS} and Z_{ICS}, respectively) vs. histologic MAD averaged for each WM tract. An outlier Z_{ICS} value for the FC WM tract was removed as its value was less than the smallest MAD observed histologically. A Bland-Altman plot between the Z_{RMS} from the one-compartment fit and histology was generated (not shown) and the 95% confidence interval was from 0.26 to 0.75 μm. A Bland-Altman plot between the Z_{ICS} and histology was generated (not shown) and the 95% confidence interval was from –0.11 to 0.24 μm.

As defined in Eq. 2, f_{ICS} is used to estimate the ICS volume fraction. Similar to the displacement PDF method, a single ICS volume fraction estimate was obtained for each specimen by averaging over the WM tracts, because an ANOVA test indicated that there was no significant difference in ICS volume fractions calculated from histology among WM tracts. There was no correlation observed between f_{ICS} and histologic ICS volume fraction. The average f_{ICS} was 0.89±0.01, which is higher than the average histologic ICS volume fraction of 0.68±0.07. In addition, a Bland-Altman plot between the f_{ICS} and histologic ICS volume fraction was generated (not shown) and the 95% confidence interval was from 0.15 to 0.27. No significant correlation was found between Z_{ECS}, the RMS displacement of water molecules in the ECS, and histologic MAD, and average Z_{ECS} was $6.8\pm1.2\mu m$.

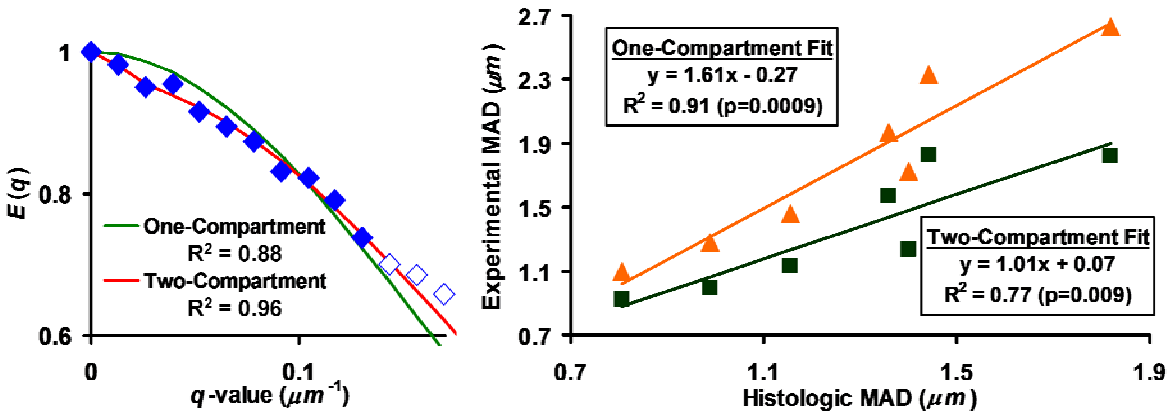

Figure 5.1. Low q-value method with short diffusion gradient (δ=0.4 ms): (a) Sample fits of a normalized signal decay curve from dCST WM tract (diamonds). Only the first 11 points were used for fitting (solid diamonds) in order to fulfill the low q-value condition. (b) Plot of average WM tract histologic vs. experimental MADs (upper curve (orange triangles): one-compartment model; lower curve (green squares): two-compartment model) with equation of line of best fit.

Figure 5.2 shows data acquired with a diffusion gradient duration of 5 ms. Figure 5.2a shows a plot of experimental MAD estimated from one- and two-compartment fits (Z_{RMS} and Z_{ICS}, respectively) vs. histologic MAD averaged for each WM tract. An outlier Z_{ICS} value for the FC WM tract was removed as its value was less than the smallest MAD observed histologically. A Bland-Altman plot between the Z_{RMS} from the one-compartment fit and histology was generated (not shown) and the 95% confidence interval was from 0.01 to 0.43 μm. A Bland-Altman plot between the Z_{ICS} and histology was generated (not shown) and the 95% confidence interval was from –0.32 to 0.06 μm. Unlike the data acquired with the shorter diffusion gradient duration, a significant correlation was found between Z_{ECS}, the RMS displacement of water molecules in ECS, and histologic MAD, as shown in Figure 5.2b. The average Z_{ECS} was 5.13±0.71 μm.

A single ICS volume fraction estimate was again obtained for each specimen by averaging over the WM tracts. In this case, there was significant correlation between f_{ICS}

and histologic ICS volume fraction (Figure 5.2c). The average f_{ICS} was 0.91±0.02, which is higher than the average histologic ICS volume fraction of 0.68±0.07. A Bland-Altman plot between the f_{ICS} and histologic ICS volume fraction was generated (not shown) and the 95% confidence interval was from 0.17 to 0.28.

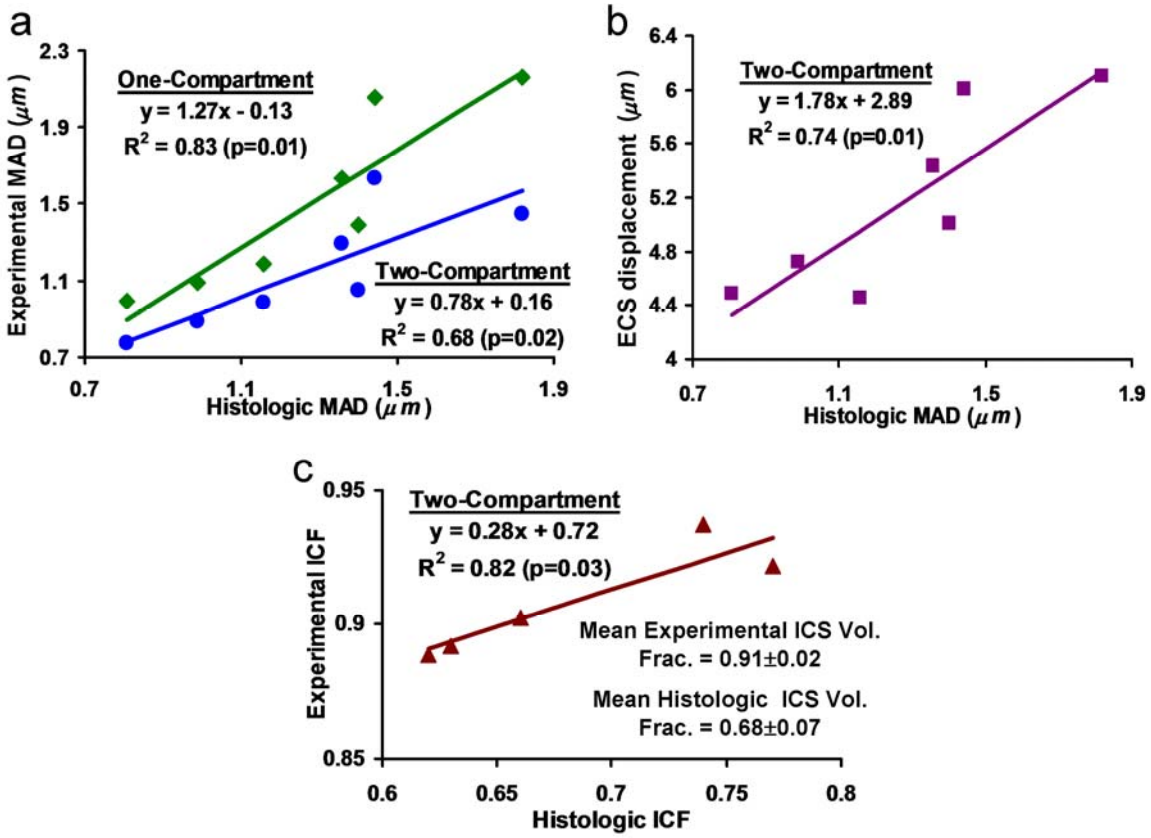

Figure 5.2. Low q-value method with long diffusion gradient (δ=5 ms): (a) Plot of average WM tract histologic vs. experimental MADs (upper curve (green diamonds): one-compartment model; lower curve (blue circles): two-compartment model) with equation of line of best fit. (b) Plot of Z_{ECS}, i.e. RMS displacement in ECS, vs. histologic MAD with equation of line of best fit. (c) Plot of experimental vs. histologic ICS volume fraction (ICF) with line of best fit and mean values.

5.4 Discussion

For the data acquired while fulfilling the SGA approximation, histology derived MAD correlated with corresponding values from both one- and two-compartment low q-

value methods (Figure 5.1b). The two-compartment fit of the echo attenuation has a higher average R^2 (0.96 versus 0.88) suggesting that it may be a better model for the echo attenuation at low q-values (Figure 5.1a). The MAD estimate from the two-compartment fit, Z_{ICS}, does show closer correspondence with histology as evidenced by the linear regression slope close to one and y-intercept close to zero. The Bland-Altman results between Z_{RMS} and histology suggest that Z_{RMS} consistently overestimates MAD. This is congruent with the fact that the diffusion in the ECS is broadening the Z_{RMS}. The Bland-Altman results suggest good agreement between MAD measured with histology and the two-compartment low q-value method.

The lack of correlation between f_{ICS} and histologic ICS volume fraction coupled with an average f_{ICS} that is higher than the average histologic ICS volume fraction suggests that f_{ICS} does not accurately measure ICS volume fraction. The Bland-Altman results also suggest that f_{ICS} systematically overestimates ICS volume fraction. Furthermore, according to our model that water molecules in the ECS experience hindered diffusion, Z_{ECS} should have a value less than the RMS displacement of freely diffusing water molecules. The average Z_{ECS} was within expected range of the RMS displacement of free water at a diffusion time of 10 ms.

For the data acquired while violating the SGA approximation, the results for one- and two-compartment low q-value methods appear similar to the results while fulfilling the SGA approximation. While both the Z_{RMS} and Z_{ICS} showed significant correlation with histologic MAD, the Bland-Altman results between Z_{RMS} and histology again suggest that Z_{RMS} consistently overestimates MAD. On the other hand, the Bland-Altman results suggest good agreement between Z_{ICS} and histology. Therefore, despite violating the SGP

approximation, the two-compartment low q-value method appears to still accurately measure MAD. Further investigation is required to confirm this observation. This may be an important quality as any implementation of this method on commercial gradient hardware will most likely necessitate violation of the SGP approximation. The effect of increasing the gradient duration further is explored in Chapter 8.

Unlike the data acquired while fulfilling the SGP approximation, this data showed significant correlation between histology and experimental ICS volume fraction and Z_{ECS}. The Bland-Altman results still suggest that f_{ICS} systematically overestimates ICS volume fraction. Perhaps due to the longer gradient duration, discrimination between ECS and ICS signals is more robust. As will be discussed further in Chapter 6, the diffusion in ECS is expected to be hindered and in ICS it is expected to be restricted. Therefore ECS and ICS signals are expected to display a different dependence on the diffusion gradient duration – namely, the ECS signal is unaffected while the ICS signal will attenuate less with increasing duration. The increased discrimination between ECS and ICS signals may allow the two-compartment low q-value method to be sensitive to inter-specimen variations in ICS volume fraction as well as provide a more accurate Z_{ECS} estimate.

A positive correlation between Z_{ECS}, the RMS displacement in ECS, and MAD is not wholly unexpected. As reported in Chapter 2, there is a negative correlation between axon density and MAD. Schwartz *et al.* (5) showed that ADC measured transversely to the axon long axis was negatively correlated with axon density. This is related to the decrease in tortuosity of the ECS as increases in axon diameter lead to larger inter-axonal spacing. At the low b-values (<2500 s/mm^2) used by Schwartz *et al.*, the authors only observed a mono-exponential decay. It is therefore reasonable to assume that the

measured ADC primarily reflected diffusion in ECS only (6). Indeed, the authors did not report any significant correlation between ADC and MAD or ICS volume fraction. The RMS displacement in ECS, therefore, could negatively correlate with axon density as axon density decreases with increasing MAD as observed here.

It should be emphasized that the experimental protocol used here was not optimized for fitting the echo attenuation at low q-values as the data was initially collected to maximize the displacement resolution. As a result, only the first 5-11 points of the q-space echo attenuation fulfilled the low q-value condition, $q << MAD^{-1}$, depending on the WM tract. Using a relatively small number of data points significantly limits the degrees of freedom for fitting, especially for the two-component fit. This may explain the higher estimate of ICS volume fraction, ECS RMS displacement and lower R^2. In an experimental protocol optimized for the low q-value method, q-values greater than ~0.1 μm^{-1} would not be necessary to fulfill the low q-value condition. The time saved could be used to improve the fitting by sampling more low q-value points or averaging the signal. Finally, the data shown here was only intended to demonstrate feasibility and is limited by its small sample size. Further investigations are needed to confirm the reported results.

5.5 Conclusions

The results reported here suggest that the low q-value method has potential to indirectly assess axonal architecture without the need for strong gradients as with the displacement PDF method. The one-compartment method shows good correlation with histology, but the two-compartment method may provide accurate estimates of MAD as

compared with histology. However, the ICS volume fraction was consistently overestimated by this method. The low q-value method also seems robust to experimental conditions violating the SGP approximation. In particular, the two-compartment method may be better at separating the ECS and ICS signals under such conditions. While further investigation is needed, the low q-value method shows potential to be implemented on commercial hardware and this will be studied further in Chapter 7.

5.6 Literature citations

1. Chin, C.L., et al., *Assessment of axonal fiber tract architecture in excised rat spinal cord by localized NMR q-space imaging: simulations and experimental studies.* Magn Reson Med, 2004. **52**(4): p. 733-40.
2. Basser, P.J., *Relationships between diffusion tensor and q-space MRI.* Magn Reson Med, 2002. **47**(2): p. 392-7.
3. Callaghan, P., *Principles of Nuclear Magnetic Resonance Microscopy*. 1993, New York: Oxford University Press.
4. Malmborg, C., et al., *Mapping the intracellular fraction of water by varying the gradient pulse length in q-space diffusion MRI.* J Magn Reson, 2006. **180**(2): p. 280-5.
5. Schwartz, E.D., et al., *MRI diffusion coefficients in spinal cord correlate with axon morphometry*. Neuroreport, 2005. **16**(1): p. 73-6.
6. Assaf, Y., et al., *New modeling and experimental framework to characterize hindered and restricted water diffusion in brain white matter.* Magn Reson Med, 2004. **52**(5): p. 965-78.

Chapter 6: Varying Gradient Pulse Duration (VGPD) Method

6.1 Introduction

As shown in previous chapters, the separation of the extracellular space (ECS) and intracellular space (ICS) signals is important for accurate measurements of axon morphology as the hindered diffusion in ECS masks ICS displacement and broadens the measured mean axon diameter (MAD). The varying gradient pulse duration (VGPD) method is an empirical approach to separating the ECS and ICS signals based on their diffusion properties. This stands in contrast to the displacement PDF (Chapter 5) and low q-value (Chapter 6) methods covered earlier which use a two-compartment model to separate the ECS and ICS signals. The displacement PDF method models the overall displacement PDF as a sum of two ECS and ICS PDFs. The low q-value method models echo attenuation at low q-values as a sum of two Gaussian ECS and ICS echo attenuations.

The accuracy of these two-compartment models depends on their *a priori* assumptions, including the shape of the ECS and ICS displacement PDFs and echo attenuations at low q-value, which may not hold true in every sample especially in the presence of pathology. Furthermore, introducing models to account for the ECS and ICS signals negates the very property that makes QSI attractive in the first place, which is that it empirically measures displacement PDF and does not assume any model for diffusion. By not making any assumptions on underlying diffusion properties the way conventional diffusion MRI does, QSI has the potential to provide new information on axonal architecture. Therefore an empirical method to separate ECS and ICS signals in QSI

would be of interest. The VGPD method is one such potential approach and is described in this chapter.

6.2 Methods

6.2.1 General theory

The general theory behind the VGPD method is based on the work by Malmborg *et al.* (1) who proposed a method to empirically measure ICS volume fraction. This method exploits the different behavior of the echo attenuation for restricted and free diffusion with respect to the diffusion gradient duration, δ, as described by Mitra & Halperin (2). Under conditions of restricted diffusion, increasing δ for a given q-value and at constant diffusion time Δ, causes the echo to attenuate less, whereas for free diffusion the echo attenuation is not dependent on δ. The reason for this is illustrated in Figure 6.1.

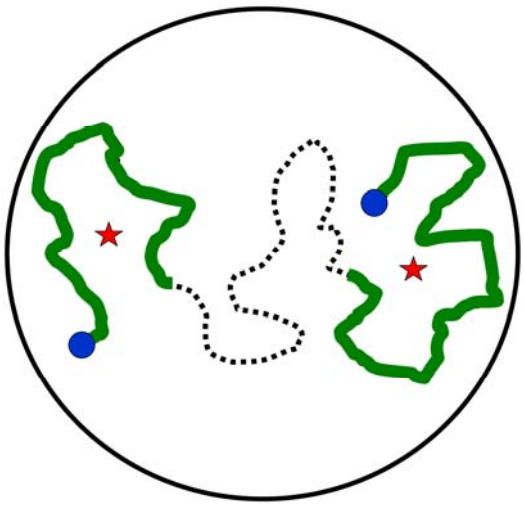

Figure 6.1. Trajectory of a diffusing particle confined in pore with a reflecting wall. Starting and ending positions are shown as blue circles. The thickened green lines correspond to the trajectory during the diffusion gradient pulses. The dotted line corresponds to the trajectory in between the gradient pulses. The center of masses of the trajectory segments during the pulses are marked by the red stars.

As described by Mitra & Haplerin, the position of the particle is given by the center-of-mass average of the trajectory segment during the application of the diffusion gradient. With infinitesimally short pulses, the particle can be labeled at any position within the pore, even next to the pore wall. As the gradient duration increases, the probability of labeling the position close to the pore wall decreases. At the limit of long gradient pulses, the position of the particle will be labeled as the center of the pore as the entire pore space will have been sampled with equal probability during the pulse. Therefore with increasing gradient duration, the apparent displacement of the center-of-mass position during the diffusion period will decrease leading to an increase in echo intensity. On the other hand, if the particle is not confined to a pore, there is no such limitation on the displacement of the center-of-mass position and the echo attenuation is not dependent on the gradient duration.

Since diffusion in the ICS is restricted whereas in the ECS it is hindered (3), the echo amplitude from spins in each compartment should exhibit a different dependence on the gradient duration. From a comparison of echo attenuations obtained at the same q-values but with varying δ (Figure 6.6), the initial decay does not vary with δ and should represent signal from ECS (3). However, at increasing q-values, the decay represents signal attenuation arising primarily from ICS and will exhibit less attenuation with increasing δ. A relaxation-weighted estimate of ICS volume fraction can then be inferred from the point at which the echo attenuations obtained at varying δ begin to diverge.

6.2.2. Empirically separating ECS and ICS signals

A natural continuation of the theory described above provides a method to empirically separate the ECS and ICS signals and allow for characterizations of diffusion in both spaces. Assuming that the point of deviation, P_d, is an accurate estimate of ICS volume fraction, then the ECS signal must have decayed significantly by the time the echo attenuation has reached P_d. Therefore, the echo attenuation after P_d must predominantly arise from ICS signal. Likewise, the echo attenuation before P_d must predominantly arise from ECS signal. P_d can then be used to empirically divide the echo attenuation into ECS and ICS parts.

The Fourier transform of the subdivided echo attenuations would give the ECS and ICS displacement PDFs without any modeling or assumptions of the peak shape. The PDFs can then be characterized in different ways to assess axonal architecture as described in Chapter 1. The FWHM can be used to characterize the average molecular displacement in ECS and ICS, which should correlate with ECS tortuosity and cellularity (4, 5) and MAD (6-8), respectively. The zero-displacement probability (ZDP) is inversely related to FWHM and reflects the fraction of molecules that experience zero-displacement. The kurtosis of the PDF is a measure of the degree of restriction to diffusion and may correlate with axon density (9, 10).

Due to the finite maximum q-value possible in experiments, the subdivision of the echo attenuation will reduce the displacement resolution of the ECS and ICS displacement PDFs. Depending on the precise location of the point of deviation, P_d, this may lead to artifacts such as observing an ECS displacement PDF with a FWHM greater than the RMS displacement expected for freely diffusing water. Another artifact could be

an ICS displacement PDF with a larger FWHM and the overall displacement PDF calculated from the full echo attenuation, which is erroneous as the overall PDF is the sum of the ECS and ICS PDFs. In order to correct these artifacts, an interpolation method is needed to improve the reduced displacement resolution. The approach chosen here is a non-linear interpolation method based on subvoxel processing and is described in the following section.

6.2.3. QSI subvoxel processing

Subvoxel processing was proposed by Hwang & Wehrli (11) and applied to MR images of trabecular bone. It is a non-linear post-processing interpolation method to increase the apparent resolution of an image while minimizing blurring due to partial voluming and can be applied to images containing two discrete intensities. The subvoxel processing algorithm is empirical rather than derived from mathematical theory, and is based on two axioms: 1) smaller voxels are more likely to have higher signal, and 2) voxels containing signal are generally in close proximity with other signal containing voxels. These principles drive the basic strategy of subvoxel processing, which is to subdivide the original voxels and assign new intensities to each subvoxel on the basis of neighboring voxel intensities and conservation of mass criteria.

The application of subvoxel processing to displacement PDFs is best described by looking at the specific example in Figure 6.2, which shows an example of a displacement PDF measured from an ROI within the ReST tract of a mouse spinal cord as described in Chapter 2. The PDF was calculated by first averaging the echo attenuation over the ROI and then performing the Fourier transform. The averaged echo attenuation had 64 q-

values. It was then truncated to 32, 16 and 8 q-values to simulate reduced displacement resolution by factors of 2, 4 and 8. The resulting PDFs are shown in Figure 6.2. The PDF with full resolution, i.e. with 64 q- values, is treated as the gold standard. The PDFs at 1/2, 1/4, and 1/8 resolution can then be compared to it.

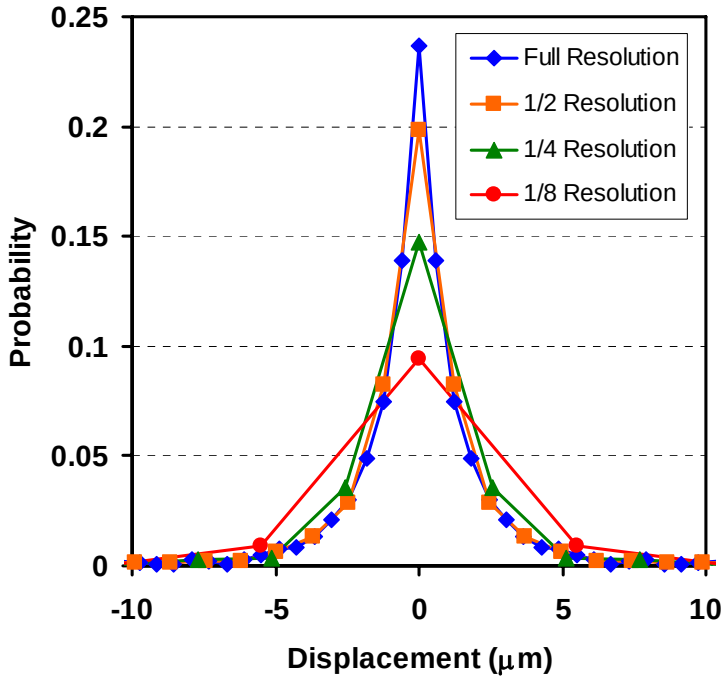

Figure 6.2. Sample displacement PDF from the ReST tract of a mouse cervical spinal cord. PDFs are shown for full, 1/2, 1/4, and 1/8 displacement resolution. No zero-filling was applied. Markers are used to identify calculated PDF points and linear interpolation was used to fill in missing values.

Decreasing displacement resolution lowers the ZDP and broadens the PDF, which leads to a higher FWHM. It is important to note that the linear interpolation as shown in Figure 6.2 would not reduce the measured FWHM of the PDFs with lower resolution. Therefore any interpolation method designed to infer what the PDF would be at higher resolution must increase ZDP and decrease FWHM.

In order to investigate whether subvoxel processing would be an appropriate interpolation method, its basic principles as applied to displacement PDFs must be

examined. First, it is clear that the displacement PDF is not a made up of two discrete intensities, but rather a continuum of intensities. This invalidates the condition for conservation of mass and can be observed in the PDFs with reduced resolutions where the point values are not simply the average of the neighboring point values of the PDF with full resolution. Second, it is evident that higher displacement resolution, which results in smaller pixels, lead to higher values of the PDF, which fulfils the first axiom of subvoxel processing. Third, it is also apparent that non-zero point values of the displacement PDF are in close proximity to other non-zero point values, which fulfills the second axiom of subvoxel processing. This suggests that using neighboring voxel intensities to assign new subvoxel intensities without the need for conservation-of-mass may be the appropriate approach.

A final consideration is how to calculate the interpolated value of ZDP. Subvoxel processing alone will not interpolate it properly. As the PDF is symmetric about zero-displacement, subvoxel processing will assign the original ZDP to the zero-displacement subvoxels. Instead, linear extrapolation is used to estimate the zero-displacement probability of the subvoxel.

With the above background covered, the algorithm for application of subvoxel processing to displacement PDF, hereafter known as QSI subvoxel processing, can now be described. All programming was done in Matlab (The Mathworks, Natick, MA). As the displacement PDF is symmetric about zero-displacement, only the left half is processed, which is then copied into the right half. To illustrate the process, imagine there are three pixels $i–1$, i, and $i+1$ from the displacement PDF at displacements x_{i-1}, x_i, and x_{i+1} each with probabilities P_{i-1}, P_i, and P_{i+1} as shown in Figure 6.3a.

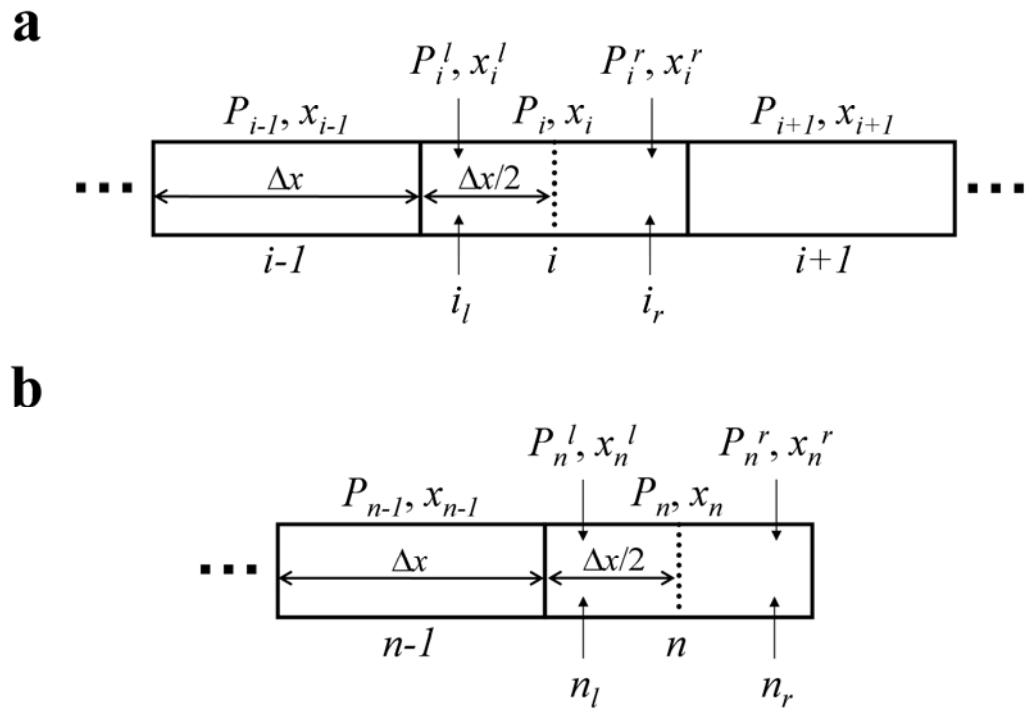

Figure 6.3. Schematic of displacement PDF pixels to illustrate the QSI subvoxel processing algorithm. See text for details. (a) General case for processing. (b) The case for interpolating the zero-displacement probability.

The original width of each pixel is Δx. Note that pixel $i+1$ is closer to the zero-displacement pixel by definition. To process pixel i, it is first divided into two subpixels labeled i_l and i_r. The width of each subpixel is $\Delta x/2$. By defining the displacement to be located at the center of the pixel, the subpixel displacements can be defined as

$$x_i^l = x_i - \frac{\Delta x}{4} \qquad (6.1a) \qquad\qquad x_i^r = x_i + \frac{\Delta x}{4} \qquad (6.1b)$$

The probabilities of the subpixels, P_i^l and P_i^r, are calculated by multiplying the original pixel probability, P_i, by normalized weights for the i_l and i_r subpixels. These weights, w_i^l and w_i^r, are expressed as

$$w_i^l = \frac{2P_{i-1}}{P_{i-1} + P_{i+1}} \qquad (6.2a) \qquad\qquad w_i^r = \frac{P_{i+1}}{P_{i-1} + P_{i+1}} \qquad (6.2b)$$

These weights are identical to the weights defined by Hwang & Wehrli (11) except the left subvoxel weight, w_i^l, is multiplied by an extra factor of 2. This was done to further compact the interpolated displacement PDF. While these weightings do not fulfill the conservation of mass condition, it was argued earlier that this condition does not apply to displacement PDFs. The subvoxel probabilities, P_i^l and P_i^r, can now be expressed as

$$P_i^l = w_i^l \times P_i = \frac{2P_{i-1}}{P_{i-1} + P_{i+1}} \times P_i \quad (6.3a) \qquad P_i^r = w_i^r \times P_i = \frac{P_{i+1}}{P_{i-1} + P_{i+1}} \times P_i \quad (6.3b)$$

Figure 6.3b depicts the situation for calculating the new ZDP. As only the left side of the displacement PDF is being processed, the zero-displacement pixel will be labeled *n* with probability P_n. In this case, the displacement for pixel *n*, x_n, is zero. Note that, for the purposes of this algorithm, there is effectively no pixel after *n* since at the end of the process all the subpixel values from the left side will be copied to the right side. To process the zero-displacement pixel *n*, it is divided into two subpixels labeled n_l and n_r. The width of each subpixel is $\Delta x/2$ and the subpixel displacements can be defined as

$$x_n^l = x_n - \frac{\Delta x}{4} = -\frac{\Delta x}{4} \quad (6.4a) \qquad x_i^r = x_n = 0 \quad (6.4b)$$

The subpixel probabilities are $P_n{}^l$ and $P_n{}^r$. The probability $P_n{}^r$ is calculated first by linear extrapolation from displacement values and probabilities of the *n-1* and n_l pixels where P_n is used as an estimate for $P_n{}^l$. After $P_n{}^r$ is calculated, $P_n{}^l$ is calculated as describe above by multiplying the original pixel probability, P_n, by a normalized weight. The weight for the subpixel n_l can then be defined as

$$w_i^l = \frac{2P_{n-1}}{P_{n-1} + P_n^r} \quad (6.5)$$

The subvoxel probability P_n^l can then be calculated as

$$P_n^r = w_i^l \times P_n = \frac{2P_{n-1}}{P_{n-1} + P_n^r} \times P_n \tag{6.6}$$

The subpixel n_r is the new zero-displacement pixel and all of the subpixels up to and including n_l are copied to the right side. This ensures that there always are an odd number of points in the interpolated PDF to match the original PDF, which centers the PDF about the zero-displacement. A two-point moving average window was used to make sure that the interpolated PDF was smooth. The interpolated displacement resolution is always half of the original resolution. It is possible to repeat the above procedure to further enhance the resolution and compact the PDF. In this case, the interpolated resolution can only be increased by multiples of two.

6.2.4. Data analysis protocol

All data acquisition details are given in Chapter 2. Using the ROIs drawn for the displacement PDF method (Chapter 4), average echo attenuations within each WM tract were obtained by averaging all the individual pixel echo attenuations within each ROI. As there were five spinal cord each with seven WM tract ROIs, there were 35 possible echo attenuations. Data acquired with both diffusion gradient durations (0.4 and 5 ms) were analyzed which meant there were 70 averaged echo attenuations overall.

QSI subvoxel processing validation

In order test the accuracy of QSI subvoxel processing, the averaged echo attenuations acquired with δ = 0.4 ms was used as a test data set. By truncating the echo attenuations, displacement PDFs with reduced resolution were generated. As QSI

subvoxel processing can only increased displacement resolution by factors of two, the echo attenuations were truncated by factors of two and four. This produced PDFs with resolutions that were 1/2 and 1/4 of the original. By applying the QSI subvoxel once, i.e. single-pass, to the 1/2 resolution PDFs, in theory, the original resolution should be recovered. Similarly, the original resolution should be recovered by applying the QSI subvoxel twice, i.e. double-pass, to the 1/4 resolution PDFs. The accuracy of QSI subvoxel processing was then tested by comparing FWHM and ZDP of the subvoxel processed PDFs with the original PDFs at full resolution.

VGPD method

The VGPD method requires both sets of averaged echo attenuations acquired with δ = 0.4 and 5 ms (E(δ=0.4ms) and E(δ=5ms), respectively). For the same WM tract and specimen, the echo attenuation value at which E(δ=0.4ms) and E(δ=5ms) begin to deviate from each other, P_d, (as observed by Malmborg *et al*. (1) when E(δ=5ms)/E(δ=0.4ms)>1.2) provides a relaxation-weighted estimate of ICS volume fraction. However, unlike Malmborg *et al*., P_d was taken as the value of E(δ=5ms) immediately prior to where the ratio E(δ=5ms)/E(δ=0.4ms) >1.2. This was done because we observed that the echo attenuation curves had already deviated when E(δ=5ms)/E(δ=0.4ms) >1.2. The VGPD measured ICS volume fraction was then compared with fractions measured from histology to assess accuracy.

The following protocol to empirically separate the ECS and ICS signals was applied to both sets of average echo attenuations acquired with δ = 0.4 and 5 ms in order to investigate the effect of violating the SGP approximation. The point of deviation, P_d,

was used to empirically divide the echo attenuation into ECS and ICS parts, as previous discussed. ECS and ICS displacement PDFs were then calculated and FWHM, ZDP, and kurtosis measurements were recorded. For comparison, the full echo attenuation was used to generate overall PDFs and the same measurements were recorded. The ECS PDF was scaled relative to the ICS PDF so that the sum of their ZDPs would equal to that of the overall PDF. Note that scaling does not affect FWHM as the entire PDF is simply multiplied by a constant value.

The overall PDFs were also used to decide when to use QSI subvoxel processing on the ICS displacement PDFs. If the FWHM of the ICS PDF were smaller than 90% of the overall PDF FWHM, then it would be inferred that the ICS displacement resolution was sufficient and no further processing was done. On the other hand, if the FWHM of the ICS displacement PDF were larger than 90% of the overall PDF, then it would be inferred that the ICS displacement resolution was too low and a single-pass QSI subvoxel processing algorithm was then run. For the dCST tract data, a double-pass QSI subvoxel processing algorithm was used. This was done because the dCST tract had the smallest MADs and the interpolated displacement resolution after single-pass QSI subvoxel processing was still large in comparison.

The criterion for deciding when to use QSI subvoxel processing on the ECS displacement PDFs was based on the belief that water in ECS cannot displace farther than the RMS displacement of free water. Given the diffusion time of 10 ms, this RMS displacement is approximately 7 μm. If the FWHM of the ECS PDF were smaller than 7 μm, then it would be inferred that the ECS displacement resolution was sufficient and no further processing was done. On the other hand, if the FWHM of the ECS PDF were

larger than 7 μm, then it would be inferred that the ECS displacement resolution was not sufficient and a single-pass QSI subvoxel processing algorithm was then run. If the single-pass FWHM of the ECS PDF were still larger than 7 μm, then a double-pass QSI subvoxel processing algorithm would be used. For the δ = 0.4 ms dataset, about 60% of the ICS and 30% of the ECS PDFs needed QSI subvoxel processing. For the δ = 5 ms dataset, 100% of the ICS and 25% of the ECS PDFs needed QSI subvoxel processing.

6.3 Results

6.3.1 QSI subvoxel processing validation

Figure 6.4a shows sample full resolution, 1/2 resolution, and single-pass QSI subvoxel processed displacement PDFs. Figure 6.4b shows sample full resolution, 1/4 resolution, and double-pass QSI subvoxel processed displacement PDFs. Note the close correspondence between the full resolution PDFs (blue diamonds) and QSI subvoxel processed PDFs (green squares).

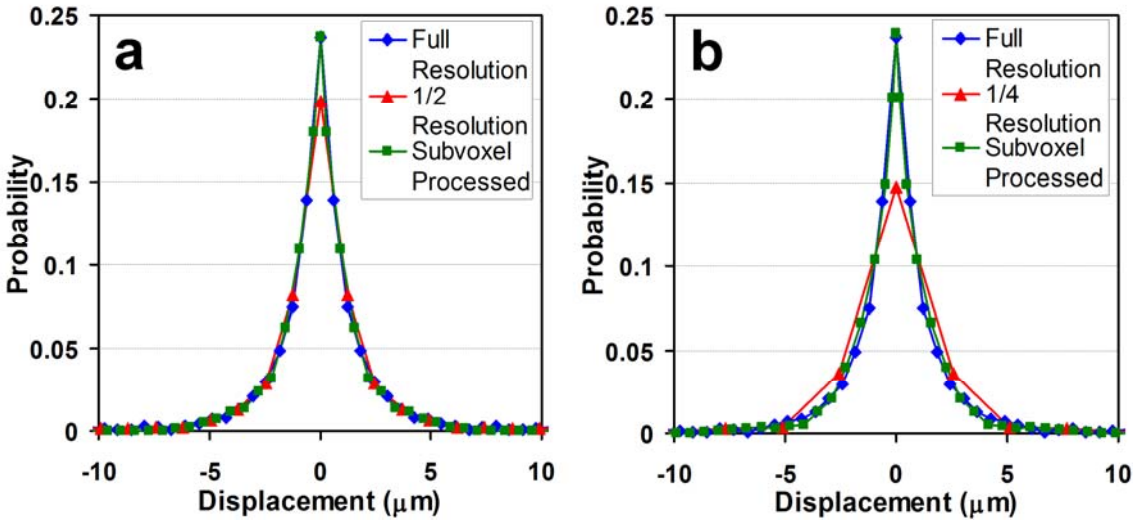

Figure 6.4. Sample PDFs from the ReST tract in a single specimen. (a) Full resolution, 1/2 resolution, and single-pass QSI subvoxel processed displacement PDFs (b) Full resolution, 1/4 resolution, and single-pass QSI subvoxel processed displacement PDFs.

Figure 6.5a shows a plot of FWHM of lower resolution and subvoxel processed PDFs vs. the original full resolution PDF with equations for lines of best fit, R^2 and p values. Each point is a mean value for a specific WM tract that was averaged over all five specimens. All processed FWHMs show excellent correlation with FWHMs from the original full resolution PDFs. Lines of best fit for 1/2 and 1/4 resolution FWHMs have slopes close to unity, but have large y-intercepts. This suggests that reducing displacement resolution increases measured FWHM as expected. Lines of best fit for QSI subvoxel processed FWHMs still have slopes close to unity, but the y-intercepts are greatly reduced. This suggests that the QSI subvoxel processed FWHMs have better agreement with the original FWHMs.

Figure 6.5b shows a plot of ZDP values of lower resolution and subvoxel processed PDFs vs. the original full resolution PDF with equations for lines of best fit, R^2 and p values. Each point is a mean value for a specific WM tract that was averaged over all five specimens. All processed ZDPs show excellent correlation with ZDPs from the original full resolution PDFs. Lines of best fit for 1/2 and 1/4 resolution ZDPs have slopes less than unity, which suggests that reducing displacement resolution decreases measured ZDP as expected. Lines of best fit for QSI subvoxel processed ZDPs have increased slopes, which suggests that the QSI subvoxel processed ZDPs are in better agreement with the original ZDPs.

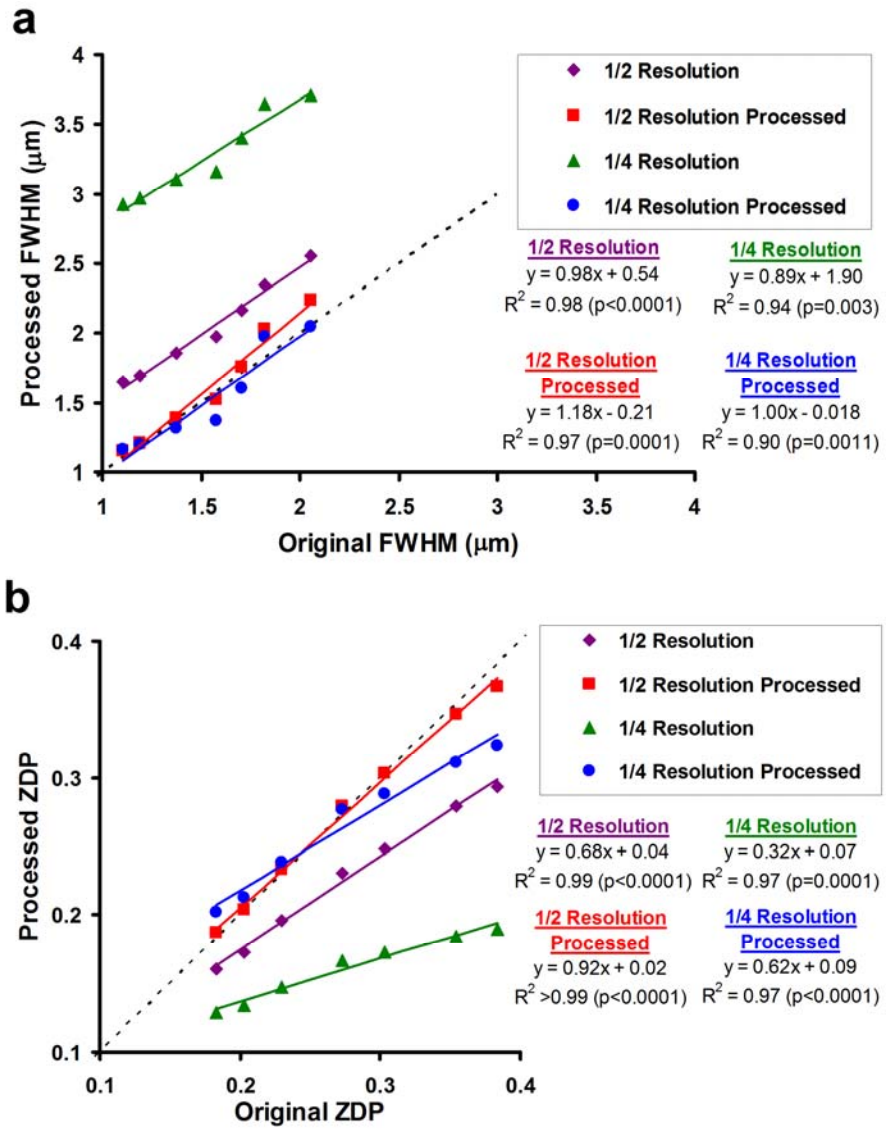

Figure 6.5. (a) Plot of FWHM of lower resolution and subvoxel processed PDFs vs the original full resolution PDF with lines of best fit. (b) Plot of ZDP of lower resolution and subvoxel processed PDFs vs. the original full resolution PDF with lines of best fit. The dotted line is line of identity.

In order to properly compare the agreement between measurements from full resolution PDFs and processed PDFs, Bland-Altman plots were generated and the 95% confidence interval limits were recorded. Table 6.1 shows the results for comparisons between various measurements with measurements from full resolution PDFs. Note that

only QSI subvoxel processed measurements displayed 95% confidence intervals which span zero.

Table 6.1. Processed vs. full res. Bland-Altman plot 95% confidence interval limits

FWHM measurement[1]	Bland-Altman plot confidence limits (μm)		ZDP measurement[1]	Bland-Altman plot confidence limits (a.u.)	
	+95%	–95%		+95%	–95%
1/2 Resolution	0.54	0.44	1/2 Resolution	–0.03	–0.07
1/2 Resolution QSI Subvoxel Processed	0.16	–0.03	1/2 Resolution QSI Subvoxel Processed	0.01	–0.01
1/4 Resolution	1.81	1.64	1/4 Resolution	–0.06	–0.17
1/4 Resolution QSI Subvoxel Processed	0.09	–0.13	1/4 Resolution QSI Subvoxel Processed	0.02	–0.04

[1] All measurements are compared with measurements from full resolution PDFs

6.3.2 VGPD method

Figure 6.6a shows sample echo attenuations (E(δ=0.4ms) and E(δ=5ms)) from the VST WM tract of a single specimen used for the VGPD method and how the ratio E(δ=5ms)/E(δ=0.4ms) is used to determine ICS volume fraction from the point of deviation, P_d. Note how P_d is defined as the point before E(δ=5ms)/E(δ=0.4ms) > 1.2. Figure 6.6b shows a plot of histologic vs. experimental ICS volume fractions. For each specimen, in both experiments and histology, a single ICS volume fraction was calculated by averaging all WM tract ICS volume fractions as an ANOVA test determined there was no significant difference in ICS volume fraction among the WM tracts. A Bland-Altman plot between the experimental and histologic ICS volume fractions (not shown) indicates the 95% confidence interval to fall in the range from –0.01 to –0.06.

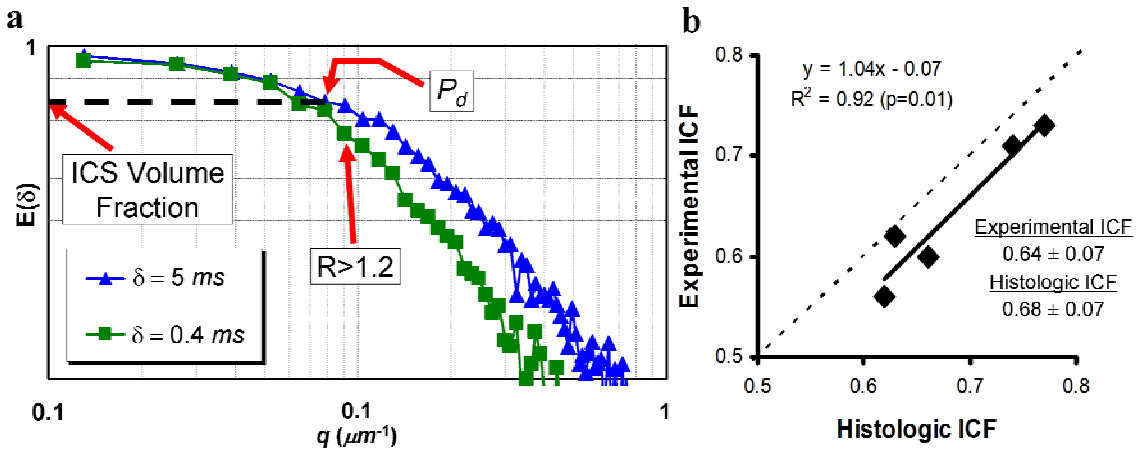

Figure 6.6. (a) Sample E(δ=0.4ms) and E(δ=5ms) curves on logarithmic axes for the VST tract in a single specimen. R = E(δ=0.4ms)/E(δ=5ms). Left arrow indicates the E(δ=5ms) value used to estimate ICF. (b) Plot of individual specimen histologic vs. experimental ICFs with line of best fit and mean values. Dotted line is line of identity.

All of the echo attenuation points before P_d are used to generate the ECS displacement PDF, while all the points afterwards, including P_d, are used to generate the ICS displacement PDF. Figure 6.7 shows examples of the overall (blue diamonds), ECS (red squares), and ICS (green triangles) PDFs from a FG tract in a single specimen. Single-pass QSI subvoxel processing was performed on the ICS PDF. This can be seen in the increased number of points in the ICS PDF. No processing was needed for the ECS PDF. Note the few number of points that describe the peak due to the larger displacement resolution.

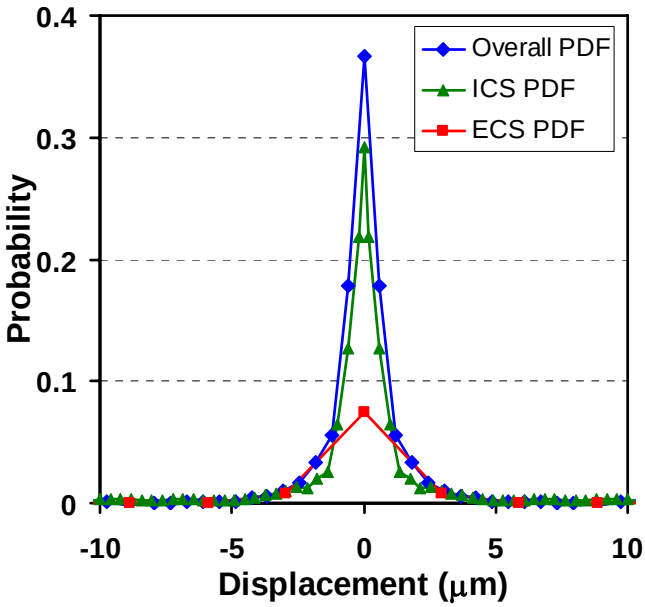

Figure 6.7. Examples of overall (blue diamonds), ECS (red squares), and ICS (green triangles) PDFs from a FG tract in a single specimen.

Figure 6.8 shows a plot of FWHM of the overall and ICS displacement PDFs vs. histologic MAD with equations for lines of best fit, R^2 and p values. Each point is a mean value for a specific WM tract that was averaged over all five specimens. The FWHMs of the overall and ICS PDF show excellent correlation with histologic MAD. For the short gradient experiments, the lines of best fit slopes close to unity, but have different y-intercepts. The overall PDF has a y-intercept of 0.25, which is in agreement with the observation that the overall PDF FWHM overestimated MAD by ~20% (see Chapter 4). The ICS PDF has a reduced y-intercept that suggests that the separation of the ECS and ICS signals improved the estimate of MAD. The long gradient experiments showed similar behavior: similar slopes of the lines of best fit but with the overall PDF having a larger y-intercept than the ICS PDF. However, the slopes were both less than one, which suggests that FWHMs of both PDFs underestimated MAD.

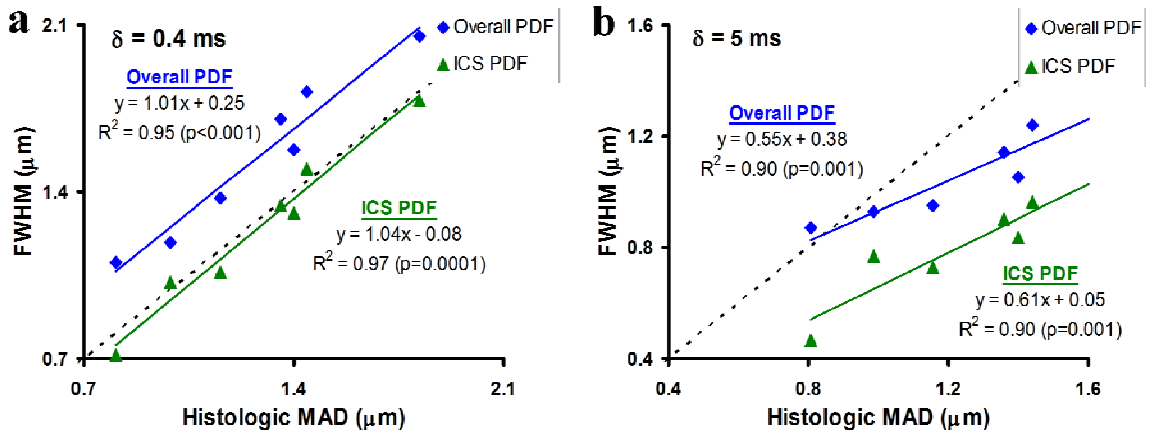

Figure 6.8. Plots of FWHM of overall and ICS displacement PDFs vs histologic MAD with lines of best fit for different gradient duration. (a) δ = 0.4 ms and (b) δ = 5 ms. The dotted line is the line of identity.

Table 6.2 summarizes the Pearson correlation coefficients between various VGPD measurements with histologic MAD under both short and long diffusion gradient durations. Significant correlations were defined as $p<0.05$. As reported earlier (Chapter 4), there were significant positive correlations between the FWHM of the overall PDF for δ = 0.4 and 5 ms and histologic MAD. There significant negative correlations between the ZDP and kurtosis of the overall PDF for δ = 0.4 and 5 ms and histologic MAD. The ICS PDF displayed similar behavior. The ECS PDF showed significant positive correlation between FWHM and histologic MAD for both δ = 0.4 and 5 ms. No significant correlation was found for ECS ZDP. There was significant negative correlation between ECS kurtosis and histologic MAD for both δ = 0.4 and 5 ms.

Table 6.2. Pearson correlations between VGPD measurements and histologic MAD

FWHM Measurement	**r, p-value**	
	δ = 0.4 ms	**δ = 5 ms**
Overall PDF	0.97, p=0.0002	0.95, p=0.001
ICS PDF	0.98, p=0.0001	0.95, p=0.001
ECS PDF	0.83, p=0.0202	0.94, p=0.0019
ZDP Measurement	**r, p-value**	
	δ = 0.4 ms	**δ = 5 ms**
Overall PDF	–0.95, p=0.0013	–0.91, p=0.0042
ICS PDF	–0.89, p=0.0072	–0.88, p=0.0091
ECS PDF	0.04, p=0.9339	0.59, p=0.1642
Kurtosis Measurement	**r, p-value**	
	δ = 0.4 ms	**δ = 5 ms**
Overall PDF	–0.95, p=0.0009	–0.94, p=0.0017
ICS PDF	–0.93, p=0.0023	–0.92, p=0.003
ECS PDF	–0.94, p=0.0015	–0.94, p=0.0017

Table 6.3 summarized the Bland-Altman plot 95% confidence intervals for the FWHM of the overall and ICS PDFs vs. histologic MAD. This was done to investigate the accuracy of the FWHM as an estimate for MAD. As previously reported (Chapter 4), the FWHM of the overall PDF overestimated MAD at short gradient duration and underestimated MAD at long gradient duration. Similar to the two-compartment displacement method, the FWHM of the ICS PDF accurately estimated MAD compared with histology at short gradient duration. At long gradient duration, the ICS FWHM still underestimated MAD.

Table 6.3. FWHM vs. histologic MAD Bland-Altman plot 95% confidence interval

δ = 0.4 ms	**Bland-Altman plot confidence limits (μm)**		**δ = 5 ms**	**Bland-Altman plot confidence limits (μm)**	
	+95%	**–95%**		**+95%**	**–95%**
Overall PDF	0.34	0.19	**Overall PDF**	–0.04	–0.35
ICS PDF	0.028	–0.09	**ICS PDF**	–0.31	–0.59

6.4 Discussion

6.4.1 QSI subvoxel processing validation

By using data from biological tissue acquired under ideal QSI experimental conditions, a standard test data set can be created to investigate the validity of the QSI subvoxel processing algorithm. Reduced displacement resolution can be generated by systematically truncating the echo attenuations and the original PDF at full resolution can serve as the control comparison. Examples of single-pass and double pass QSI subvoxel processed 1/2 and 1/4 resolution displacement PDFs show good agreement with full resolution displacement PDFs (Figure 6.4).

All processed FWHM and ZDP values showed excellent correlation with values from the original full resolution PDFs (Figure 6.5). As processed PDFs are being compared with unprocessed PDFs, it is expected that if QSI subvoxel processing truly corrects low resolution, the lines of best fit of this processed data would have a slope of unity and zero y-intercept. This is most clearly observed with the FWHM plots (Figure 6.5a). The ZDP plots also show this behavior, but the QSI subvoxel processed 1/4 resolution ZDP line of best fit had a slope less than unity. However, the slope did increase compared without QSI subvoxel processing.

Bland-Altman plot analysis determines if two measurement methods are identical. If QSI subvoxel processing truly corrects low resolution, it is expected that the Bland-Altman analysis will show that the subvoxel of processed and full resolution PDF measurements are identical. Indeed, the results shown in Table 6.1 indicate that lower displacement resolution alone increases FWHM and decreased ZDP, as expected. After

QSI subvoxel processing, FWHM and ZDP measurements are identical to measurements from the original full resolution PDFs.

Taken as a whole, these results suggest that the QSI subvoxel processing algorithm accurately corrects for low displacement resolution and may be used to interpolate displacement PDFs to improve resolution. Only a specific range of low displacement resolutions were studied and further investigation with a broader range is needed. Nevertheless, the displacement resolution values used in the VGPD method fall within the tested range, which suggests that QSI subvoxel processing is valid to use here.

6.4.2 VGPD Method

The first step of the VGPD method is to define the point of deviation, P_d, to estimate ICS volume fraction. Histologic and experimental ICS volume fractions are well correlated (Figure 6.6b). Furthermore, all experimental ICS volume fractions fall within the expected range of 60-80% (12). The Bland-Altman results suggest that the volume fraction method slightly underestimates the histologic ICS volume fraction. Nevertheless, the data indicates that this method may provide ICS volume fraction estimates in WM in fair agreement with those observed histologically, thereby validating the prior results by Malmborg *et al*. (1).

It should be noted that this method only provides a relaxation-weighted ICS volume fraction estimate from P_d. The exact relaxation weighting effect on P_d is unclear. Nevertheless, as a result of the short TE used here, ECS and ICS signals did not decay significantly, errors from different T_2 relaxation times in the two compartments should be small (ECS and ICS T_2s have been reported as 78 and 300 ms, respectively (13)). Further,

as the technique only differentiates between restricted and free diffusion, histologic ICS volume fraction included both the ICS and myelin regions since the myelin water is restricted by the myelin sheaths as discussed earlier. Unlike the displacement PDF method, there is no need for sufficient displacement resolution to resolve the restricted diffusion in myelin as the volume fraction method uses the echo attenuation in q-space. This may explain why the ICS volume fraction measured with this method, and not the displacement PDF method, showed correlation with histology.

Finally, due to the cylindrical geometry of axons, the observed fraction of restricted diffusion, and hence ICS volume fraction, depends on the orientation of the applied diffusion gradients as discussed by Malmborg *et al*. For example, if the gradients were applied parallel to the axon direction, then the ICS signal would not be restricted. True ICS volume fraction requires the diffusion gradients to be applied orthogonal to the axon. While the choice of spinal cord tissue allowed the diffusion gradients to be oriented orthogonal to the WM tracts, the VGPD method may be applied to tortuous WM tracts in the brain with a tensor analysis (14) so that the q-space echo attenuation from diffusion orthogonal to the WM tract can always be computed.

The ICS volume fraction results suggest that P_d can be used as the boundary between the ECS and ICS echo attenuations. It is important to note that as P_d changes for every data set, q_{max} will change for the ECS and ICS echo attenuations. Therefore, there is not a common displacement resolution for the ECS and ICS PDFs. This was not an issue for the ICS PDFs as the resolution was generally under 1 μm after truncation. Corrections were still necessary with QSI subvoxel processing, but the initial resolution was still quite high. As a consequence of the observed P_d, the ECS displacement

resolution was much lower than the ICS displacement resolution. As it can be seen in Figure 6.7, there are few points to describe the ECS PDF. Therefore, the measured FWHM may be inaccurate and likely overestimated due to the low resolution.

For the short gradient duration data, the FWHM, ZDP, and kurtosis values of the ICS PDF showed the expected correlations with MAD. Again, according to the Bland-Altman results, the FWHM of the overall PDF overestimates MAD, while the FWHM of the ICS PDF accurately measures MAD as compared with histology. These results suggest that the ICS displacement PDF represents diffusion within the axon. The FWHM, and kurtosis values of the ECS PDF also showed significant positive and negative correlations with MAD, respectively. As reported in Chapter 2, there is a negative correlation between axon density and MAD. The positive FWHM correlation suggests that the ECS displacement decreases with higher axon density, while the negative kurtosis correlation suggests that the ECS diffusion is less hindered with decreased axon density. These results suggest that ECS FWHM is sensitive to the tortuosity in ECS. As axon density increases, axons are crowded together and ECS water molecules will not displace as far. This behavior as been observed in WM tissue (5) and in cancerous tumors where hypercellularity reduces the RMS displacement of water molecules in ECS (4).

It is important to note that no correlations between ECS FWHM or RMS displacement were observed with the two-compartment displacement PDF (Chapter 4) or low q-value (Chapter 5) methods. The major difference between these methods is that they required a two-compartment model to separate the ECS and ICS signals while the VGPD method empirically separates the two. Inaccuracies in the model assumptions may have distorted the observed ECS displacement behavior. As it is reasonable to expect that

the ECS diffusion to be sensitive to axon density as described above, the results support the use of an empirical approach to better study diffusion in ECS and ICS.

In order to investigate the effects of violating the SGP approximation, the VGPD method was applied to data with long diffusion gradient duration (δ = 5 ms). As expected, the FWHM of the overall and ICS PDFs are decreased (2), and, unlike the short gradient results, the Bland-Altman analysis shows that both underestimate MAD. Nevertheless, the same correlation behavior between FWHM, ZDP, and kurtosis values and histologic MAD was observed. This suggests that while violating the SGP approximation may no longer allow the VGPD method to accurately estimate MAD, it may still be sensitive to variations in MAD and axon density. The VGPD method may therefore still be useful for detecting changes in axon morphology even under conditions violating the SGP approximation.

6.5 Conclusions

The results reported here suggest that the VGPD method has potential to indirectly assess axon morphology and separate the ECS and ICS signals without the need for modeling. A QSI subvoxel processing algorithm was developed to increase the apparent displacement resolution and validated with experimental data. Experimental ICS volume fractions showed good correlation with histology. The FWHM, ZDP, and kurtosis of the ICS PDF showed good correlation with histology and the FWHM may provide accurate estimates of MAD as compared with histology. However, the ICS volume fraction was underestimated by this method. The FWHM, and kurtosis of the ECS PDF showed good correlation with histology and may provide a measurement of

ECS tortuosity. Violating the SGP approximation may reduce the accuracy of the VGPD method and underestimate MAD. However, the method may still be sensitive to relative changes in MAD and axon density.

6.6 Literature citations

1. Malmborg, C., et al., *Mapping the intracellular fraction of water by varying the gradient pulse length in q-space diffusion MRI.* J Magn Reson, 2006. **180**(2): p. 280-5.
2. Mitra, P. and B. Halperin, *Effect of finite gradient pulse width in pulsed gradient diffusion measurements.* Journal of Magnetic Resonance, Series A, 1995. **113**(1): p. 94-101.
3. Assaf, Y., et al., *New modeling and experimental framework to characterize hindered and restricted water diffusion in brain white matter.* Magn Reson Med, 2004. **52**(5): p. 965-78.
4. Charles-Edwards, E.M. and N.M. deSouza, *Diffusion-weighted magnetic resonance imaging and its application to cancer.* Cancer Imaging, 2006. **6**: p. 135-43.
5. Schwartz, E.D., et al., *MRI diffusion coefficients in spinal cord correlate with axon morphometry.* Neuroreport, 2005. **16**(1): p. 73-6.
6. Cory, D.G. and A.N. Garroway, *Measurement of translational displacement probabilities by NMR: an indicator of compartmentation.* Magn Reson Med, 1990. **14**(3): p. 435-44.
7. Ong, H.H. and F.W. Wehrli, *Quantifying axon diameter and intra-cellular volume fraction in excised mouse spinal cord with q-space imaging.* Neuroimage, 2010. **51**(4): p. 1360-6.

8. Ong, H.H., et al., *Indirect measurement of regional axon diameter in excised mouse spinal cord with q-space imaging: simulation and experimental studies.* Neuroimage, 2008. **40**(4): p. 1619-32.

9. Chin, C.L., et al., *Assessment of axonal fiber tract architecture in excised rat spinal cord by localized NMR q-space imaging: simulations and experimental studies.* Magn Reson Med, 2004. **52**(4): p. 733-40.

10. Jensen, J.H., et al., *Diffusional kurtosis imaging: the quantification of non-gaussian water diffusion by means of magnetic resonance imaging.* Magn Reson Med, 2005. **53**(6): p. 1432-40.

11. Hwang, S.N. and F.W. Wehrli, *Subvoxel processing: a method for reducing partial volume blurring with application to in vivo MR images of trabecular bone.* Magn Reson Med, 2002. **47**(5): p. 948-57.

12. Sykova, E. and C. Nicholson, *Diffusion in brain extracellular space.* Physiol Rev, 2008. **88**(4): p. 1277-340.

13. Peled, S., et al., *Water diffusion, T(2), and compartmentation in frog sciatic nerve.* Magn Reson Med, 1999. **42**(5): p. 911-8.

14. Assaf, Y., et al., *High b-value q-space analyzed diffusion-weighted MRI: application to multiple sclerosis.* Magn Reson Med, 2002. **47**(1): p. 115-26.

Chapter 7: Feasibility of Implementation on a Clinical Scanner

7.1 Introduction

In previous chapters, several different QSI-based methods (displacement PDF, low q-value, and VGPD) have been shown to have the potential to indirectly assess axon morphology and make accurate measurements of mean axon diameter (MAD) and intracellular space (ICS) volume fraction. In this chapter, preliminary data is presented to investigate the feasibility of implementing these methods on a clinical scanner for potential *in vivo* studies. The data reported here only investigates the major hardware limitation with a clinical scanner, i.e. maximum gradient strength, and not issues relating to *in vivo* imaging itself, which are numerous and varied. Issues relating to feasibility of *in vivo* imaging will be briefly discussed in the Discussion section.

As discussed in Chapter 2, maximum gradient strength is a major concern as it imposes an inherent limitation on QSI – the achievable displacement resolution. The resolution is determined by q_{max}, which is proportional to the area of the gradient pulse at maximum gradient strength. The maximum gradient strength of the Micro-Z gradient was 5000 G/cm, while the maximum gradient strength of the clinical scanner used here is only 4 G/cm. Even with violating the SGP approximation, the factor of 1000 decrease in gradient strength severely limits the maximum achievable displacement resolution.

The preliminary data presented here therefore investigates what type of indirect measurements of axon morphology using the previously described methods are possible with the limitation in gradient strength and displacement resolution in mind. Data collected on fixed pig spinal cord is analyzed with each of the displacement PDF, low q-value and VGPD methods.

7.2 Methods

7.2.1 Material and methods

Animal specimens

Fixed cervical spinal cord specimens were harvested from five skeletally mature Yucatan mini-pigs (70-90 kg, ~18 months old). The pigs were obtained from Dr. Schaer in the Comparative Orthopaedic Research Laboratory (CORL) at the New Bolton Center, Veterinary Medicine, University of Pennsylvania. Within 1 hr of euthanasia, the whole cervical spinal cord was immediately harvested (~15 cm long) and the dura mater was punctured before immersing in 10% neutral buffered formalin (Sigma-Aldrich, St. Louis, MO, USA). The spinal cords were immersed in fixing solution for a period of 3-14 days. Afterwards, excess meninges were removed and the cords were placed in storage tubes with PBS. Before experiments, the cords were trimmed and placed in 14 ml screw top conical tubes filled with Fomblin (Sigma-Aldrich, St. Louis, MO, USA), a fluorinated oil, to keep the specimens hydrated and to remove any background signal. All five tubes containing cervical cord specimens were taped together for simultaneous imaging.

Imaging hardware

All experiments were performed on a 1.5T Siemens Sonata MRI scanner (Erlangen, Germany) with 40 mT/m gradients (slew rate- 200 T/m/s). The body coil was used for transmit and a custom-built 4-channel phased array coil (Insight MRI, Worchester, MA, USA) was used for receive. No parallel imaging was employed and the four channels were used to improve SNR. The five tubes taped together containing spinal

cord specimens immersed in Fomblin were placed within the coil. Sandbags and a plastic buckle were used to secure the RF coil.

Pulse sequence

All pulse sequence development was done in Sequence Tree (www.thesouthpoles.com/sequencetree), which is an open source MRI pulse sequence programming environment developed by Jeremy F. Magland. To reduce scan time, a 2D single-slice PGSE with multi-shot echo-planar-imaging (EPI) readout sequence (1) was used (Figure 7.1). To simplify reconstruction, k-space lines were acquired in a non-alternating fashion, i.e. only equal polarity echoes were used. The echo time (TE) in the PGSE portion was chosen so that the echo formed in the center of the EPI acquisition window. The EPI imaging parameters were as follows: reconstructed matrix size = 128×128, FOV = 64×64 mm, slice thickness = 10 mm, number of shots = 8, number of echoes = 16, dummy scans = 16, NA = 36, TR = 2 s, echo spacing = 4 ms, readout BW = 100 kHz. The PGSE parameters were diffusion time = 98.7 ms and TE = 257 ms. Two combinations of diffusion gradient duration (δ) and maximum gradient strength (G) were run and chosen to have identical q-values: δ/G = 55 ms/34 mT/m and 90 ms/20.778 mT/m. For both sets of parameters, 16 equally spaced q-values were acquired with identical q_{max} = 0.08 μm^{-1}, which gave a displacement resolution of 6.3 μm. The total scan time was ~2.5 hours. For the shorter gradient duration parameters, an additional data set was acquired with 32 equally spaced q-values for low q-value fitting with a total scan time ~5 hours. The experimental data acquired with the above parameters was analyzed in different ways depending on the method applied as described below.

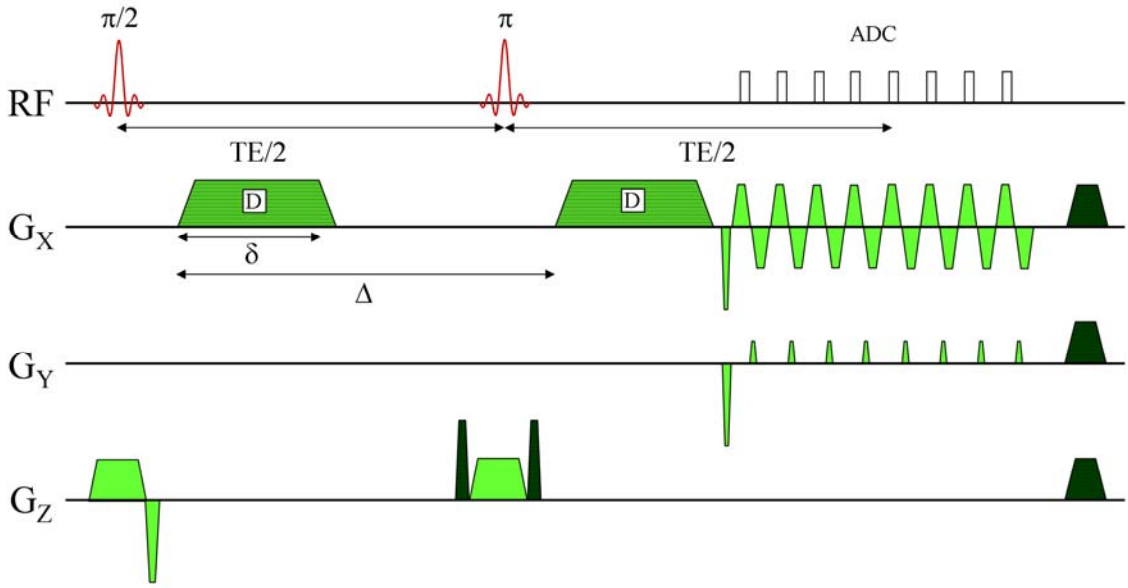

Figure 7.1. Diagram of PGSE with multi-shot EPI readout sequence. Labels: D = diffusion gradient, Δ = diffusion time, δ = diffusion gradient duration, ADC = analog to digital converter. Darker gradients signify spoiling and crusher gradient moments. Number of echoes was reduced for display purposes only.

7.2.2 Data analysis

After Fourier transform of the k-space data with a factor of two zero-filling using Matlab (Mathworks, Natwick, MA, USA), a 3D matrix of 16 or 32 2D images at various q-values was obtained. Using ImageJ (NIH, Bethesda, USA), ROIs were drawn in the dorsal, ventral, and lateral columns of the spinal cords (Figure 7.2). Average echo attenuations were calculated for each ROI for further processing depending on the method applied. The basic processing for the displacement PDF, low q-value and VGPD methods have been described in previous chapters. Specific processing steps for each method used here are described below.

For the displacement PDF method, only the one-compartment protocol was applied as the displacement resolution was so low (6.3 μm) that the two-compartment model would not have significantly improved MAD estimation. Furthermore, the shape

of ICS displacement PDF may not be the exponential decay peak used in Chapter 4 as the diffusion gradient duration is much longer here. Mitra & Halperin (2) predicted that at very long gradient durations, the displacement PDF of molecules restricted within a pore approximates a Gaussian. The average echo attenuations were reflected about q = 0, and a Fourier transform was done to produce a purely real displacement PDF. The FWHM, ZDP, and kurtosis values were then measured.

For the low q-value method, the data set with δ = 55 ms and 32 q-values was analyzed. As the echo attenuations were to be fit to a model, a data with 32 q-values was preferred to 16 q-values. Since q_{max} = 0.08 μm^{-1}, it was reasonable to assume that all the q-values fulfilled the low q-value requirement of $q << MAD^{-1}$ for MAD of 1-2 μm. Therefore the full echo attenuations were fit with the one and two-compartment low q-value method as described in Chapter 5 (Eq. 5.1 and 5.2). The only major difference between the fitting protocol use here and in Chapter 5 was that Z_{ECS} (RMS displacement in ECS) was not constrained to be less than 8 μm.

For the VGPD method, the major concern for feasibility on a clinical scanner is the much longer gradient durations required. As described in Mitra & Halperin (2), with increasing gradient duration, for restricted diffusion, the echo attenuation will be attenuated less. With changes in very long gradient durations, i.e. 55 vs. 90 ms, the differences in echo attenuations become smaller as the center-of-mass displacement differences are also smaller (see Chapter 6 and (2)). It is not clear whether or not the gradient durations used here would still show differences in echo attenuation due to restricted diffusion. Furthermore, due to the lower gradient strengths, it is not apparent whether the achievable q_{max} (0.08 μm^{-1}) is sufficient to observe the differences between

hindered and restricted diffusion in the echo attenuations. Note that in Chapter 6, the point of deviation was observed between 0.1–0.3 μm^{-1}. However, the diffusion time is much larger here (10 vs. 98.7 ms) and differences between hindered and restricted diffusion may be accentuated. Finally, as with the displacement PDF method, the displacement resolution is so low that there is not sufficient resolution to properly resolve ECS and ICS PDFs. While QSI subvoxel processing can be used to improve resolution, it has not been validated for use with such low resolutions. Due to these concerns, the full VGPD method is not applied here. Only a comparison between echo attenuations with δ = 55 and 90 ms was performed to investigate the feasibility of differentiating hindered and restricted diffusion based on a different dependence on diffusion gradient duration.

Statistical Analysis

All statistical analysis was performed with Excel (Microsoft, Redmond, WA, USA). ANOVA was used to evaluate differences in FWHM, ZDP, and kurtosis values between ROIs (dorsal, lateral, and ventral columns), and, if significant, paired t-tests were used *post hoc* to evaluate how the ROIs specifically differed. Paired t-tests were used as the comparison was between ROIs in the same specimen. A correction for multiple-comparisons was not used here.

7.3 Results

In order to test that the pulse sequence program runs properly, it was used to measure ADC of a bottle of 1mM Gd doped water. All the imaging parameters were the same except that the gradient duration and strength were set to 11 ms and 34 mT/m so

that b-values ranged from 0 to ~1000 s/mm^2. The calculated ADC was 1.98×10^{-3} mm^2/s which matches literature values (3). This result suggested that the PGSE diffusion-weighted multi-shot EPI pulse sequence was working properly.

Figure 7.2 shows sample diffusion-weighted 8-shot EPI magnitude images at q = 0 μm^{-1} and q_{max} = 0.08 μm^{-1}. Sample ROI locations are shown for the dorsal (red), lateral (green) and ventral (blue) WM columns. Note the clear discrimination between GM and WM at q = 0 μm^{-1}. This distinction is lost at q_{max} = 0.08 μm^{-1}. In comparison with images acquired with the Micro-Z gradient (Chapter 4), it appears that q_{max} is not high enough to reverse the GM and WM contrast (4). The SNR at q = 0 μm^{-1} ranged from 10-25. The SNR at q_{max} ranged from 3-15. The dorsal column consistently exhibited the lowest SNR while the lateral columns exhibited the highest SNR. There is a hyper-intense region outside one of the spinal cords due to residual PBS. This generates a ghosting artifact due to insufficient spoiling. The artifact did not affect the QSI results and was not corrected.

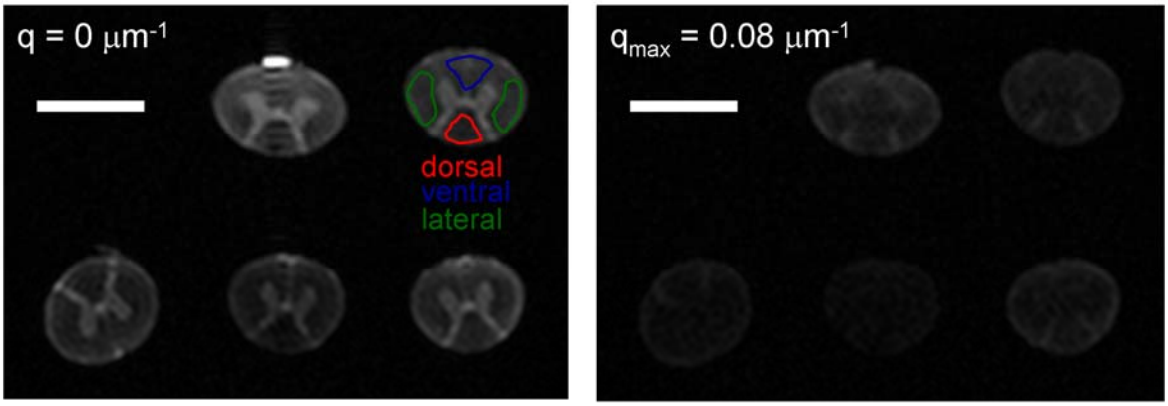

Figure 7.2. Sample diffusion-weighted 8-shot EPI magnitude images at q = 0 μm^{-1} and q_{max} = 0.08 μm^{-1}. The white bar represents a length of 10 mm. ROI locations are shown for the dorsal, ventral and lateral WM columns. The bright spot in above the center top cord in the q = 0 μm^{-1} image is due to residual surface PBS.

7.3.1 Displacement PDF method

Figure 7.3 shows sample echo attenuations and displacement PDFs for dorsal, lateral, and ventral WM columns for δ = 55 ms. Note that only five points describe the PDF peaks due to the very low displacement resolution. The data suggests that all three PDFs have similar shape and the dorsal column PDF has the highest ZDP. Regional differences in the echo attenuations are apparent. The dorsal echo attenuation is attenuated less than the lateral and ventral echoes, which implies that the dorsal displacement PDF should also have a smaller FWHM.

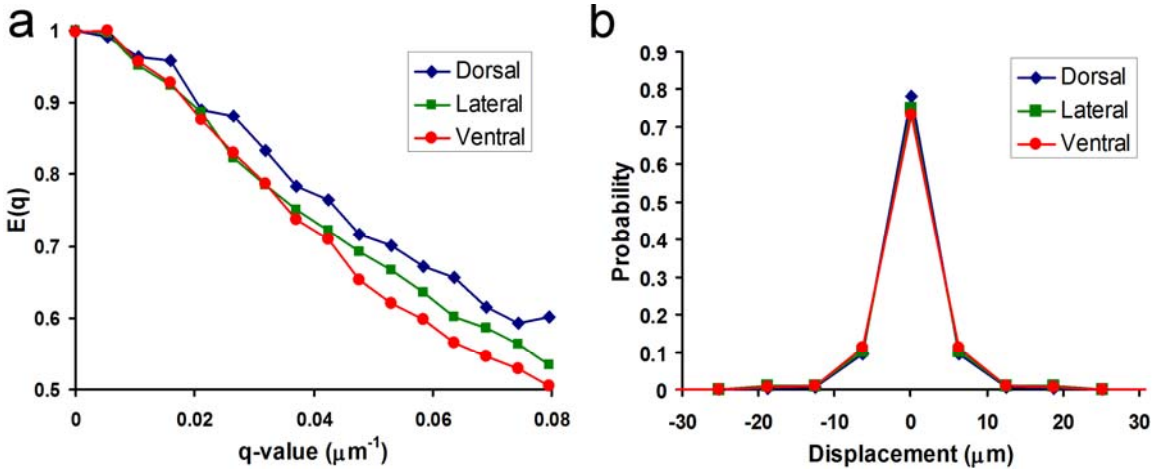

Figure 7.3. Sample echo attenuation, E(q) (a) and displacement PDFs (b) from dorsal, lateral and ventral column ROIs for δ = 55 ms.

Figure 7.4 shows bar graphs of FWHM, ZDP, and kurtosis values for each ROI average over all five specimens for δ = 55 ms. ANOVA analysis indicated there were significant differences in the measured values between the ROIs. Therefore, paired t-tests were used to compare specific values between ROIs. Significant p-values (<0.05) between different ROIs are indicated in Figure 7.4. There is a trend of increasing FWHM and decreasing ZDP and kurtosis from dorsal to lateral to ventral ROIs. This suggests that the dorsal column contains smaller axons than the other two ROIs. Figure 7.5 shows bar

graphs of FWHM, ZDP, and kurtosis values for each ROI average over all five specimens for δ = 90 ms. The data for δ = 90 ms is similar to that for δ = 55 ms except that paired t-tests indicated significant differences in FWHM, ZDP and kurtosis between the lateral and ventral columns. There is again a trend of increasing FWHM and decreasing ZDP and kurtosis from dorsal to lateral to ventral ROIs.

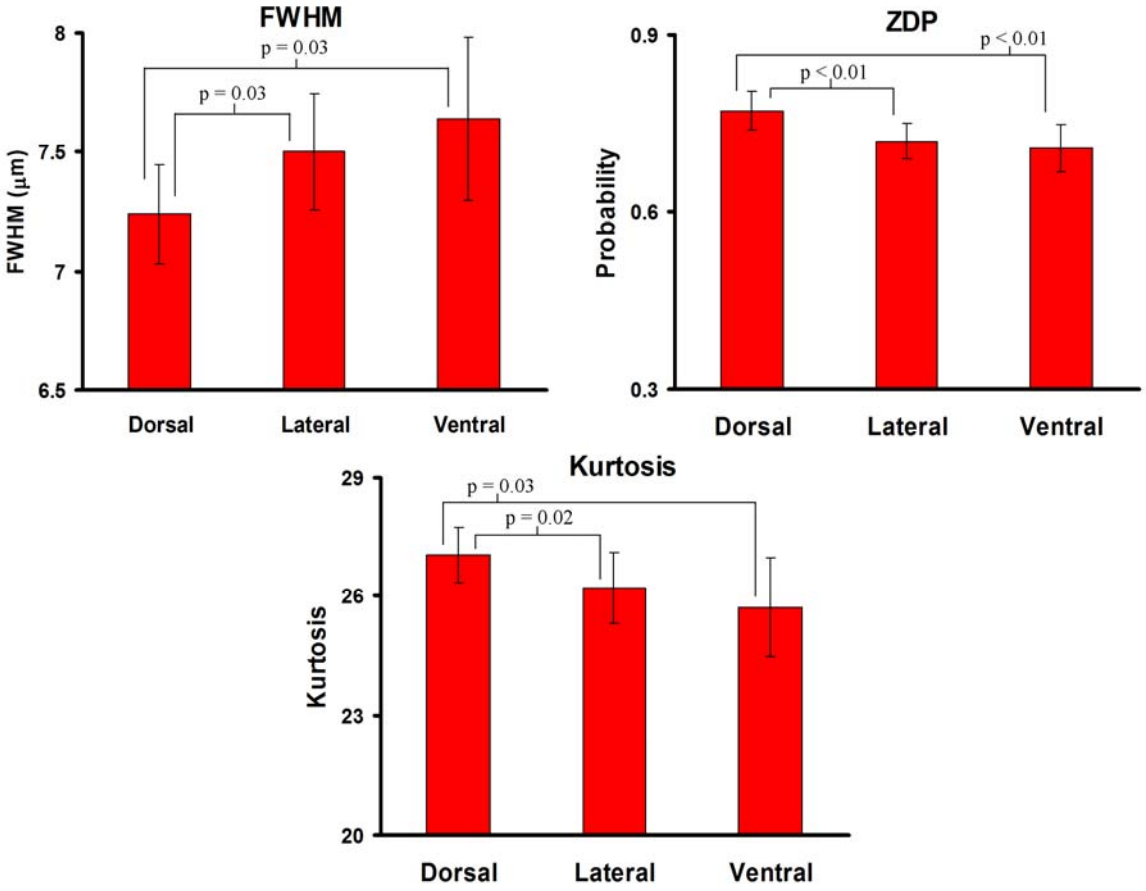

Figure 7.4. Bar graphs of mean FWHM, ZDP, and kurtosis values for each ROI average over all five specimens for δ = 55 ms. Standard deviation bars are shown. Significant p-values (<0.05) of paired t-tests between the different ROIs are shown.

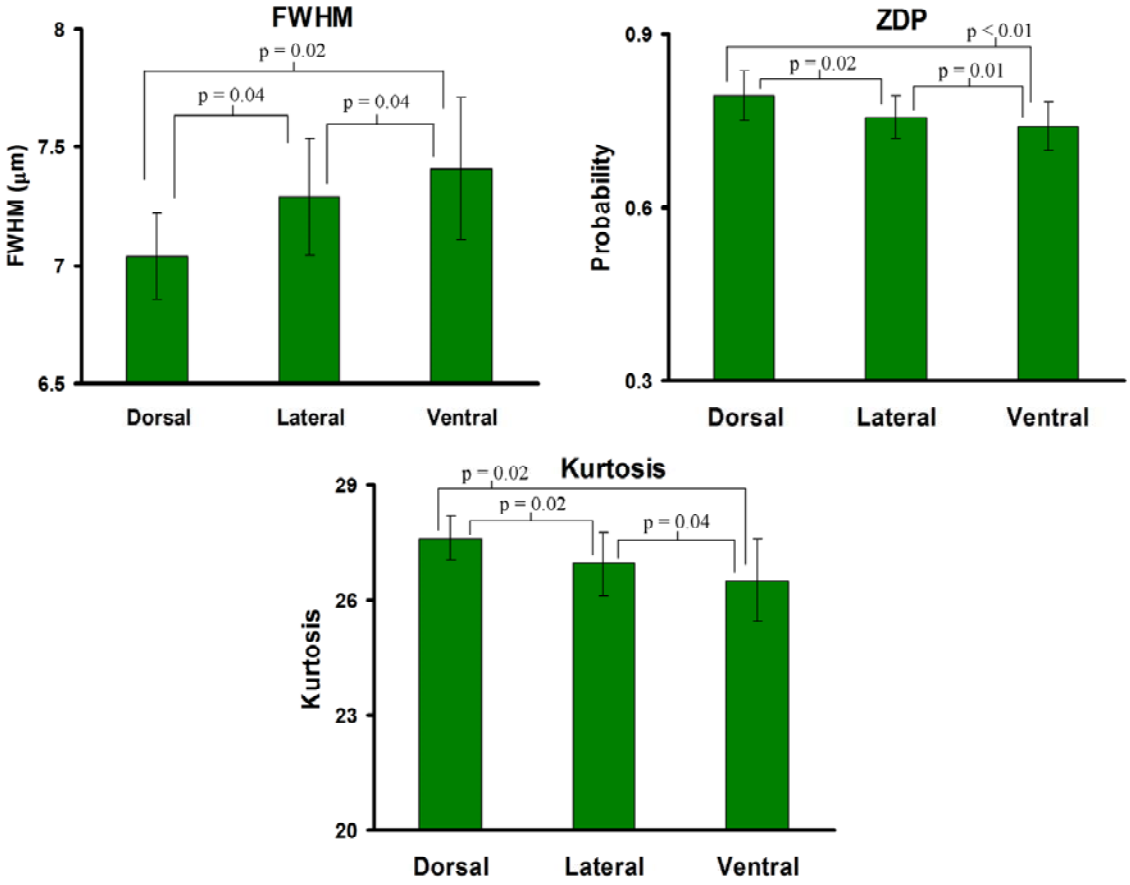

Figure 7.5. Bar graphs of mean FWHM, ZDP, and kurtosis values for each ROI average over all five specimens for δ = 90 ms. Standard deviation bars are shown. Significant p-values (<0.05) of paired t-tests between the different ROIs are shown.

To better visual differences, Figure 7.6 shows bar graphs of FWHM, ZDP, and kurtosis values for each ROI average over all five specimens for δ = 55 and 90 ms. The longer gradient duration data exhibit lower FWHM and higher ZDP and kurtosis values as expected (2). As indicated in the figure, paired t-tests between FWHM, ZDP and kurtosis values with shorter and longer gradient durations indicate that these differences are significant.

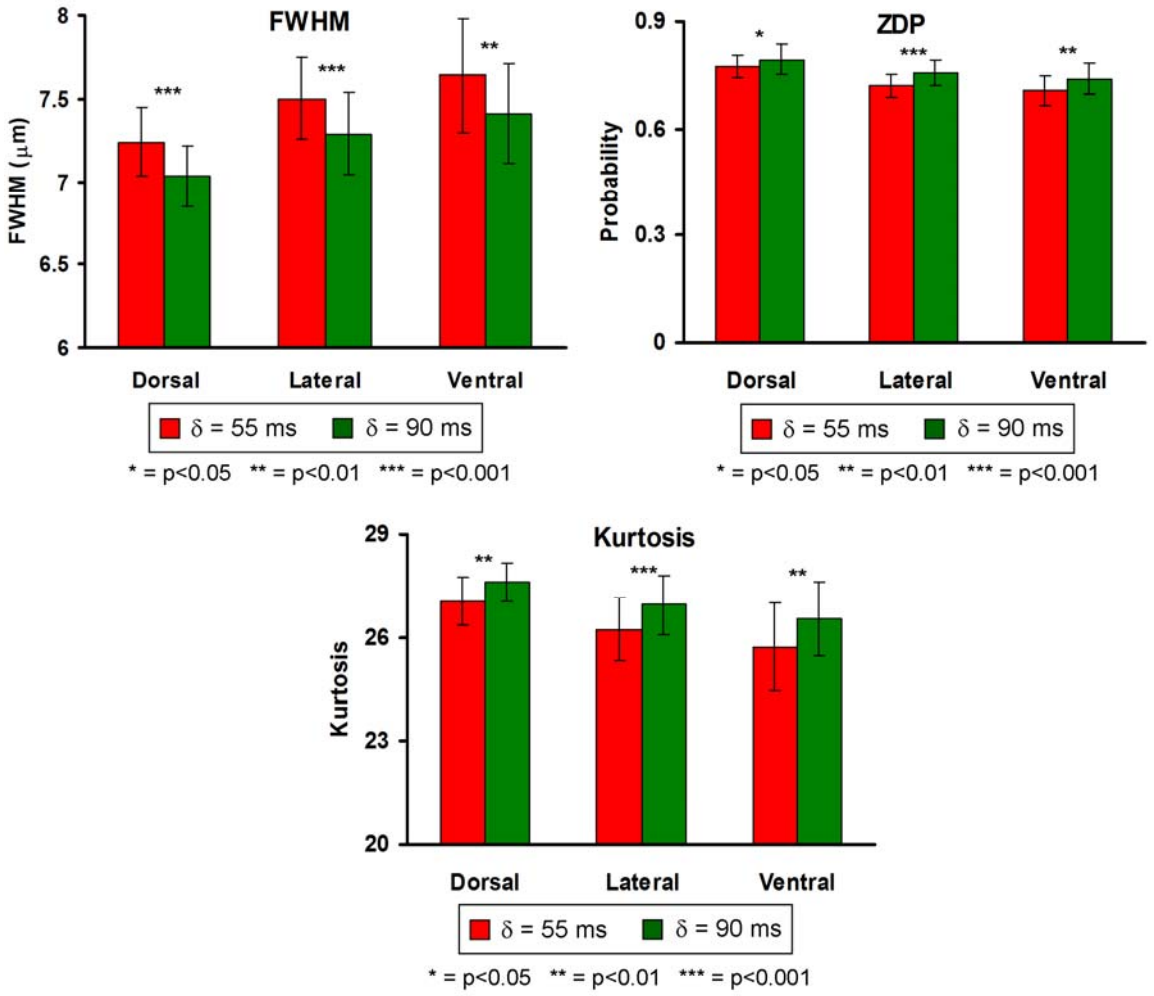

Figure 7.6. Bar graphs of mean FWHM, ZDP, and kurtosis values for each ROI average over all five specimens for δ = 55 (red) and 90 (green) ms. Standard deviation bars are shown. Asterisks indicate p-values of paired t-tests between the different gradient durations.

7.3.2 Low q-value method

Figure 7.7 shows a sample average echo attenuation plot for a lateral WM column ROI (blue diamonds) along with one-compartment (green line) and two-compartment (red line) low q-value fits. It is readily apparent that the one-compartment fit does not fit the measured echo attenuation well, whereas the two-compartment fit shows good

agreement (R^2 >0.98). All one-compartment fits were similar to that shown in Figure 7.7. Therefore, one-compartment fit results are not reported.

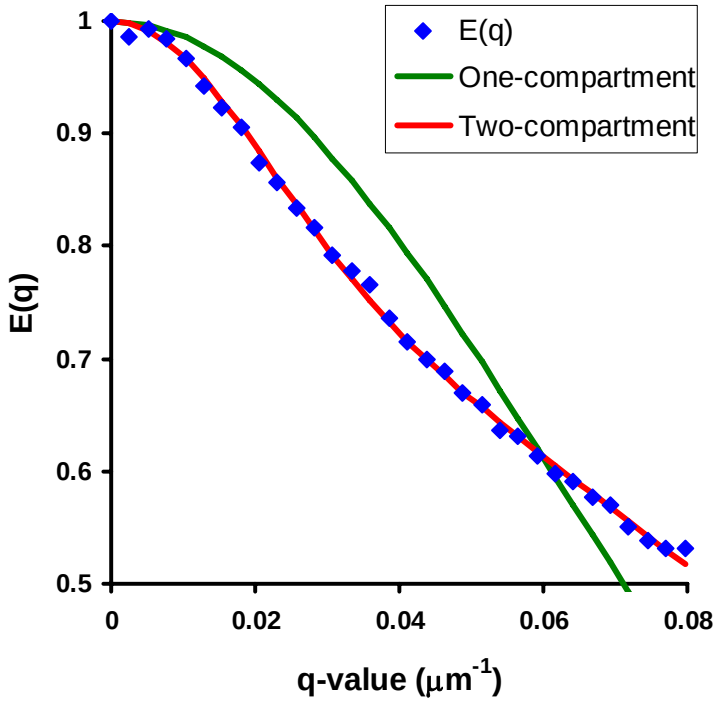

Figure 7.7. Plots of echo attenuation, E(q), for a lateral WM column ROI (blue diamonds) with one-compartment (green line) and two-compartment (red line) low q-value fits.

Figure 7.8 shows bar graphs of ECS weighting, ECS RMS displacement, ICS weighting, and ICS RMS displacement calculated from the two-compartment low q-value fit for each ROI average over all five specimens. It is important to note that the ECS RMS displacements are lower than that expected for free water with a diffusion time of 98.7 ms (~20 μm). The ADC calculated from the ECS RMS displacements were ~0.25×10^{-3} mm^2/s which agrees with literature values for fixed spinal cord WM tissue (5). It is also noteworthy that the ICS RMS displacements fall within 1-2 μm, which is the expected range of axon diameters in mammals (6).

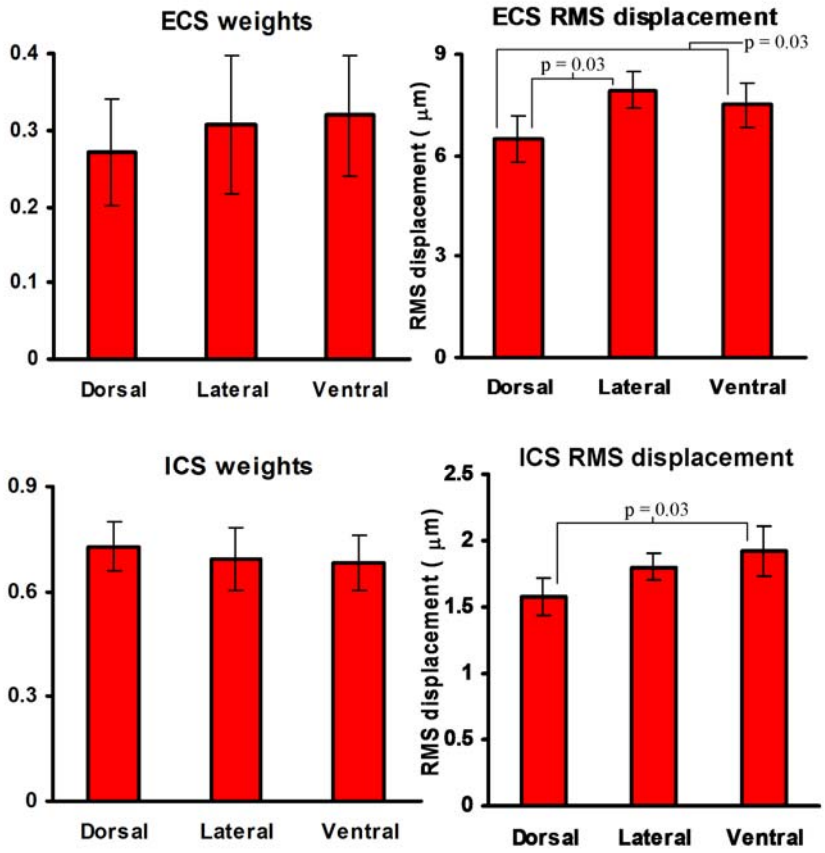

Figure 7.8. Bar graphs of ECS weighting, ECS RMS displacement, ICS weighting, and ICS RMS displacement calculated from the two-compartment low q-value fit for each ROI average over all five specimens. Standard deviation bars are shown. Significant p-values (<0.05) of paired t-tests between the different ROIs are shown.

An ANOVA analysis indicated that there was no significant difference in ECS and ICS weighting among all three ROIs, whereas there was a significant difference in ECS and ICS RMS displacement. Paired t-tests were the performed between ECS and ICS RMS displacement of various pairs of ROIs in order to discern what the significant difference was and significant p-values (<0.05) are shown in Figure 7.8. The results indicate that the dorsal WM column ECS and ICS RMS displacements are significantly smaller than those of the ventral WM column. No significant differences were found between the lateral and ventral WM columns.

7.3.3 VGPD method

Figure 7.9 shows echo attenuation plots for dorsal, lateral, and ventral ROIs averaged over all five specimens for both δ = 55 and 90 ms. The initial part of the echo attenuation does not show a clear difference between δ = 55 and 90 ms. However at higher q-values, it is clear that longer gradient duration leads to less echo attenuation for all ROIs. The difference in attenuation is much less than that observed for δ = 0.4 and 5 ms (Chapter 6). A rough estimate of P_d by visual inspection falls within the range of 0.85 to 0.95. Note that the standard deviation for the dorsal echo attenuations is largest as its SNR was lowest among the WM column ROIs.

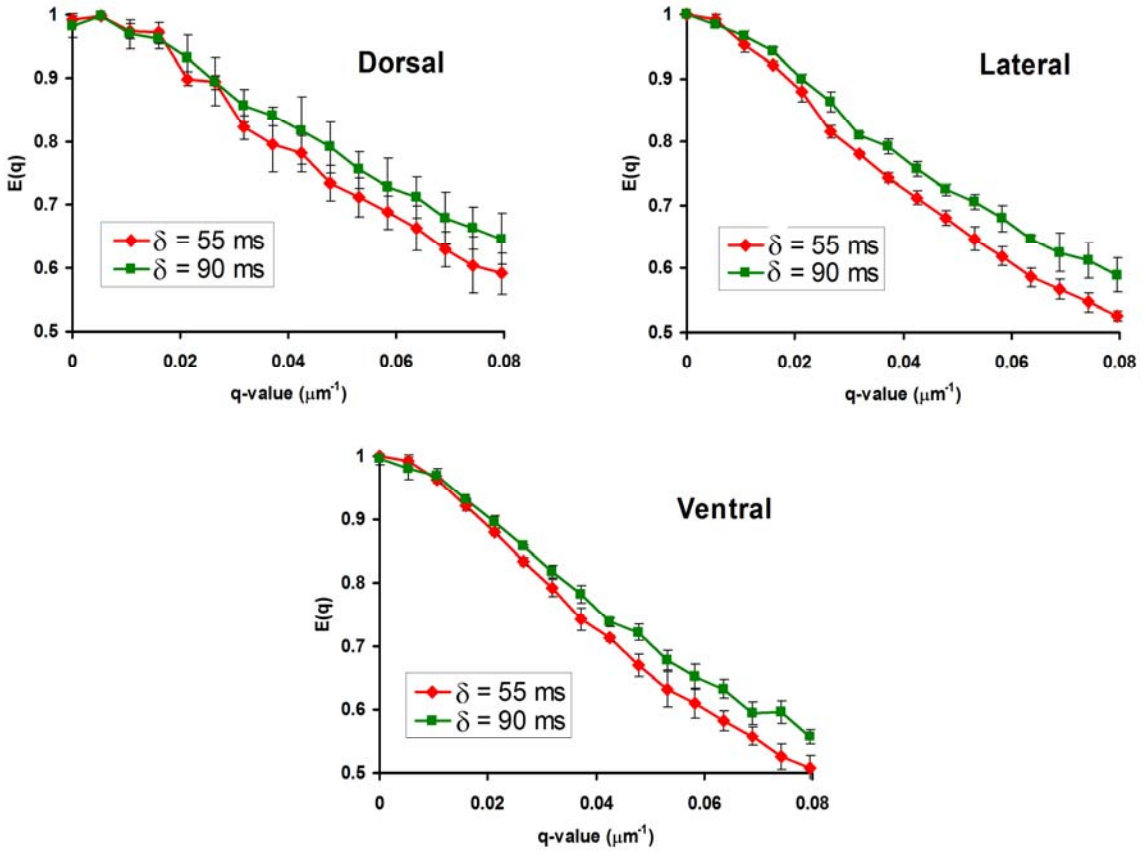

Figure 7.9. Echo attenuation plots for dorsal, lateral, and ventral ROIs averaged over all five specimens for both δ = 55 and 90 ms. Standard deviation bars are shown.

7.4 Discussion

It was necessary to acquire images with sufficient spatial resolution in order to spatially resolve GM and WM. Otherwise, partial voluming of GM and WM will complicate interpretation of the results as GM will introduce new hindered (ECS) and restricted (ICS) diffusion components. However to achieve this spatial resolution, the slice thickness had to be greatly increased to compensate for the loss of SNR. A slice thickness of 10 mm was deemed appropriate as the average vertebral cervical cord segment was ~20 mm, and it was assumed that axon morphology did not change significantly within a segment. In any *in vivo* spinal cord, however, there will be partial voluming of GM and WM. How this blurring of GM and WM affects the QSI-based methods described here is unclear and further investigation is needed.

7.4.1 Displacement PDF method

It was not expected that this method would provide accurate estimates of axonal architecture. The imaging parameters used here were chosen to try and maximize displacement resolution and it was still a factor of 10 lower that what was achieved with the Micro-Z gradient (Chapter 4). Furthermore, the gradient durations are over a factor of 10 longer, and this is known to narrow the displacement PDF. There are, therefore, two competing effects: a broadening of the PDF due to low displacement resolution and a narrowing of the PDF due to long gradient durations. A quantitative understanding of the interaction of these effects is lacking, but based on previous literature applying QSI to clinical scanners (7-9) it seems that low displacement resolution is the dominant effect.

A previous QSI study of excised pig spinal cord (10) reported FWHMs of ~13-14 μm, which is double what is reported here. This can be easily explained as that study has a lower displacement resolution (~10 μm vs. ~6 μm). Despite these limitations in resolution, these studies report enhanced sensitivity of FWHM and ZDP to pathology (7-10). Indeed, there seemed to be regional differences observed in the PDFs measure here on the pig cervical spinal cords. While there was no histology done on these cords, it is not unreasonable to expect in mammals that the dorsal column to contain the smaller axon compared with the lateral and ventral columns (6, 11, 12). Therefore, it would be expected that the dorsal ROI displacement PDFs would have smaller FWHM, and higher ZDP and kurtosis as it was observed.

Another interesting observation, which has implications for the VGPD method, was that the PDFs still showed the expected behavior when the gradient duration was increased. Specifically, the FWHM decreased while ZDP and kurtosis increased with longer gradient durations; these observations were statistically different from those with shorter gradient durations. Therefore, despite the much longer gradient durations and low displacement resolutions, the PDFs were still sensitive to changes in gradient durations. This suggests that the VGPD method may still be applicable on clinical scanners. Furthermore, this observed gradient duration dependence, which is only true for restricted diffusion (2), supports the assumption that ICS diffusion is still restricted even at diffusion time as long as $\Delta = 98.7$ ms.

7.4.2 Low q-value method

This method showed the greatest potential for clinical feasibility as its measurements of axon morphology did not depend on high displacement resolution. However, there were still uncertainties regarding the long gradient durations needed on the clinical scanner. The Gaussian approximation of the echo attenuation at low q-values is only strictly valid under the SGP limit (13, 14). While this condition could easily be fulfilled using the Micro-Z gradient, the SGP approximation would certainly be violated using clinical gradient hardware. In Chapter 5, the low q-value method was used under conditions violating the SGP approximation and ECS and ICS RMS displacements still showed good correlation and agreement with histology. However, in that case the gradient duration was only increased to 5 ms and it is not clear how those results would hold up when the gradient duration was pushed to 55 ms as it was done here.

In this preliminary data, it appears that the two-compartment low q-value method provides metrics that agree well with expected axon morphology. For example, the ICS RMS displacements fall within the range of 1-2 μm, which is the expected range of axon diameters in mammals (6). This estimate of MAD is a large improvement over the PDF FWHM used in the displacement PDF method. The ICS RMS displacement also showed regional differences and suggested that the dorsal column contained smaller axons, which as discussed above, may be a reasonable expectation. Again, it should be emphasized that these measurements were made without the need for high displacement resolution. Furthermore, the ICS weighting was ~0.7, which falls within the range of 0.6-0.8 expected for ICS volume fractions in nervous tissue (15). No significant regional

differences were observed for ICS weighting as was seen previously in mouse spinal cords (16).

The ECS RMS displacement fits also give interesting insight into axon morphology. The ADCs calculated from the ECS RMS displacement agree well with reported values. This provides further evidence that ADCs measured at low b-values (<2500 s/mm^2) primarily reflect diffusion in ECS (12, 17). ECS RMS displacement also shows regional differences and suggests that the dorsal column has the smallest ECS displacement due to diffusion. This agrees with our previous observations with the VGPD method that ECS displacement is correlated with MAD. Recall that the dorsal column may have smaller axons and hence a more tortuous ECS.

It is encouraging that the two-compartment low q-value method still provides insights into axon morphology as described above at a long gradient duration of 55 ms. Perhaps the long duration better discriminates between ECS and ICS signals due to their different echo attenuation dependence on gradient duration as discussed in Chapter 6. Unfortunately, there is no histologic data for the pig spinal cords. Therefore, while the results show interesting insights into anticipated axonal architecture, the low q-value method has not been rigorously validated. However, the preliminary results here are certainly encouraging and warrant further investigation.

7.4.3 VGPD method

The central requirement in the VGPD method is that diffusion in ECS is hindered, while diffusion in ICS is restricted (18). This means that the ECS and ICS echo attenuations have a different dependence on gradient duration. If this difference in

behavior cannot be observed, then the VGPD method cannot be applied. As mentioned earlier, the difference in echo attenuation for restricted diffusion between shorter and longer gradient duration is smaller with increasing duration (2). Therefore it was unclear whether or not echo attenuations acquired with δ = 55 and 90 ms would exhibit the necessary behavior for the VGPD method.

As already remarked with the displacement PDF method data, it appears that even with these long gradient durations, restricted diffusion behavior is observed in the echo attenuations as shown in Figure 7.9. The echo attenuation with a gradient duration of 90 ms (E(δ = 90ms)) is attenuated less than the echo attenuation with a gradient duration of 55 ms (E(δ = 55ms)). Thus a point of deviation, P_d, can be defined, but it is more difficult to observe as the differences between E(δ = 90ms) and E(δ = 55ms) are smaller. The metric used in Chapter 5, where P_d was defined as the point before E(δ = 90ms)/E(δ = 55ms) >1.2 is not valid here. The largest ratio of E(δ = 90ms)/E(δ = 55ms) is ~ 1.1, which is at q_{max}; therefore, it does not define a point of deviation and another metric must be developed.

It is important to remember that P_d is a relaxation-weighted estimate of ICS volume fraction. In order to maximize q_{max}, the gradient duration had to be increased substantially. This in turn will increase the TE of the PGSE diffusion preparation. When TE was set to 257 ms, as is done here, there must be significant ECS and ICS signal attenuation due to T_2, which will affect the accuracy of P_d as an estimate of ICS volume fraction. The P_d was roughly estimated by visual inspection to be in the range of 0.85-0.95, which is higher than the expected the range of 0.6-0.8 for ICS volume fractions in nervous tissue (15). This may be the result of a longer T_2 for ICS signal than ECS signal

(19). The exact relaxation dependence of P_d is not clear and would require further investigation.

The VGPD method still suffers from the inherent limitation of the displacement PDF method, which is the need for high displacement resolution. By splitting up the echo attenuation into ECS and ICS parts, the resolution for the ECS and ICS displacement PDFs will be worse than that for the displacement PDF method results above. The PDFs will be significantly broadened and any accurate measurement of MAD is unlikely. While the QSI subvoxel processing was designed to improve displacement resolution, it was only used to improve the resolution by a factor of two or four (Chapter 6). The PDFs shown here need an improvement in resolution by a factor of eight or more, and QSI subvoxel processing has not been validated for these conditions. While accurate measures of axonal architecture may not be possible, as discussed with the displacement PDF method, the VGPD method may still find utility if it can differentiate between changes in axon morphology either due to anatomy or pathology.

7.4.4 Feasibility of in vivo application

As mentioned earlier, the focus of this chapter was to investigate the feasibility of implementing the various QSI-based methods on a clinical scanner. The main focus was to study the effects of the much lower gradient amplitudes available and longer gradient durations necessary to achieve a significant q-value. In this section, various issues relating to *in vivo* applications are discussed.

In vivo imaging introduces various physiologic processes not present in excised tissue. In particular, motion due to blood flow, breathing, and both voluntary and

involuntary movement produces artifacts in diffusion MRI experiments (20-22). The diffusion gradients will encode for any displacement of the spins whether it arises from diffusion, flow or another type of movement. Any non-diffusion displacement will therefore complicate interpretation of the results. Motion correction methods such as parallel imaging (23) and navigator echoes (22) should be used to mitigate such artifacts.

There are significant differences in MR properties between fixed and unfixed tissue that must be considered (24). T_1 and T_2 relaxation constants and ADC tend to be reduced after fixation. It has been suggested that the observed ADC at low b-values primarily reflects diffusion in ECS (12, 18) and the effects of fixation on diffusion in ICS is not clear. Fixation also affects membrane permeability and thus the water exchange rate between ECS and ICS. It has been reported that fixation *increases* membrane permeability (24), which suggests that diffusion observed *in vivo* may be more restricted in ICS than in fixed tissue. Further, tissue temperature *in vivo* would be higher than that for the results reported here and it is known that higher temperature increases ADC (25).

All these changes in relaxation and diffusion properties between fixed and unfixed tissue must be considered for *in vivo* imaging. The longer T_1 and T_2 relaxation constants for unfixed tissue may aid *in vivo* imaging by improving SNR. The differences in diffusion and membrane permeability properties will determine the validity of the underlying assumption that diffusion in ECS is hindered while in ICS it is restricted. Increased ADC and water exchange may lessen the differences in diffusion properties and limit the ability to separate ECS and ICS signals. The precise effect of these changes on diffusion in ECS and ICS observed *in vivo* is not clear and requires further investigation.

Total scan time is an important consideration for *in vivo* imaging. A live subject cannot be imaged indefinitely and scan times on the order of minutes is preferred. The experimental parameters used in this chapter were chosen without regard to this requirement and the scan times were several hours long. This was done because of the need to have high spatial resolution to distinguish GM and WM. The high resolution necessitated a multi-shot EPI readout with averaging to improve SNR, which significantly increased scan time. As mentioned earlier, partial voluming of GM and WM will introduce new hindered (ECS) and restricted (ICS) diffusion components to the overall signal. The effects of these new components on the QSI experiment are not clear and would need further investigation. *In vivo* spinal cord imaging would not resolve GM and WM due to limits on scan time (9) and so understanding these partial voluming effects is important.

Another way to minimize scan time would be to reduce the number of q-values that are acquired. In particular, the low q-value method implemented in this work used 32 q-values, but similar results may be obtained with 16 or fewer q-values. The minimum number of q-values needed for proper fitting should be determined so that total scan time can be as short as possible. Finally, a PGSE with a single-shot EPI readout sequence would also greatly reduce scan time at the sacrifice of image resolution which would lead to partial voluming effects as discussed. Much can be done to optimize the implementation of the QSI-based methods for *in vivo* imaging and requires further investigation.

7.5 Conclusion

Preliminary data was presented here to investigate the feasibility of implementing the displacement PDF, low q-value, and VGPD methods on a clinical scanner. The major limitation was the maximum gradient strength available, which restricts the achievable displacement resolution. For the displacement PDF and VGPD methods, this leads to a broadened PDF and decreasing the likelihood of any accurate measurement of axon morphology. The two-compartment low q-value method showed the most promising results that provided anticipated insights into axonal architecture. Most importantly, the estimate of MAD was between 1-2 μm, which is within the range of expected axon diameters in mammals. Unfortunately, there was no histologic data so this method was not rigorously validated. Furthermore, any future *in vivo* application has significant challenges that must be overcome. The results are nonetheless encouraging and warrant further investigation.

7.6 Literature citations

1. Schmitt, F., M.K. Stehling, and R. Turner, *Echo-planar imaging: theory, technique, and application*. 1998, Berlin: Springer-Verlag.
2. Mitra, P. and B. Halperin, *Effect of finite gradient pulse width in pulsed gradient diffusion measurements.* Journal of Magnetic Resonance, Series A, 1995. **113**(1): p. 94-101.
3. Mills, R., *Self-diffusion in normal and heavy water in the range of 1-45 degrees.* J Phys Chem, 1973. **77**: p. 685-688.
4. Wright, A.C., et al., *Construction and Calibration of a 50 T/m Z-Gradient Coil for q-Space Microscopy.* Journal of Magnetic Resonance, 2007. **186**: p. 17-25.
5. Schwartz, E.D., et al., *Ex vivo evaluation of ADC values within spinal cord white matter tracts.* AJNR Am J Neuroradiol, 2005. **26**(2): p. 390-7.
6. Williams, P.L., et al., eds. *Gray's anatomy: the anatomical basis of medicine and surgery*. 38th ed. 1995, Churchill Livingstone: New York, NY.
7. Assaf, Y., et al., *High b-value q-space analyzed diffusion-weighted MRI: application to multiple sclerosis.* Magn Reson Med, 2002. **47**(1): p. 115-26.
8. Assaf, Y., et al., *High b value q-space-analyzed diffusion MRI in vascular dementia: a preliminary study.* J Neurol Sci, 2002. **203-204**: p. 235-9.
9. Farrell, J.A., et al., *High b-value q-space diffusion-weighted MRI of the human cervical spinal cord in vivo: feasibility and application to multiple sclerosis.* Magn Reson Med, 2008. **59**(5): p. 1079-89.

10. Biton, I.E., et al., *Improved detectability of experimental allergic encephalomyelitis in excised swine spinal cords by high b-value q-space DWI.* Exp Neurol, 2005. **195**(2): p. 437-46.

11. Ong, H.H., et al., *Indirect measurement of regional axon diameter in excised mouse spinal cord with q-space imaging: simulation and experimental studies.* Neuroimage, 2008. **40**(4): p. 1619-32.

12. Schwartz, E.D., et al., *MRI diffusion coefficients in spinal cord correlate with axon morphometry.* Neuroreport, 2005. **16**(1): p. 73-6.

13. Basser, P.J., *Relationships between diffusion tensor and q-space MRI.* Magn Reson Med, 2002. **47**(2): p. 392-7.

14. Malmborg, C., et al., *Mapping the intracellular fraction of water by varying the gradient pulse length in q-space diffusion MRI.* J Magn Reson, 2006. **180**(2): p. 280-5.

15. Sykova, E. and C. Nicholson, *Diffusion in brain extracellular space.* Physiol Rev, 2008. **88**(4): p. 1277-340.

16. Ong, H.H. and F.W. Wehrli, *Quantifying axon diameter and intra-cellular volume fraction in excised mouse spinal cord with q-space imaging.* Neuroimage, 2010. **51**(4): p. 1360-6.

17. Charles-Edwards, E.M. and N.M. deSouza, *Diffusion-weighted magnetic resonance imaging and its application to cancer.* Cancer Imaging, 2006. **6**: p. 135-43.

18. Assaf, Y., et al., *New modeling and experimental framework to characterize hindered and restricted water diffusion in brain white matter.* Magn Reson Med, 2004. **52**(5): p. 965-78.

19. Peled, S., et al., *Water diffusion, T(2), and compartmentation in frog sciatic nerve.* Magn Reson Med, 1999. **42**(5): p. 911-8.

20. Haacke, E.M., *Magnetic resonance imaging : physical principles and sequence design*. 1999, New York: Wiley. xxvii, 914 p.

21. Rohde, G.K., et al., *Comprehensive approach for correction of motion and distortion in diffusion-weighted MRI.* Magn Reson Med, 2004. **51**(1): p. 103-14.

22. Norris, D.G., *Implications of bulk motion for diffusion-weighted imaging experiments: effects, mechanisms, and solutions.* J Magn Reson Imaging, 2001. **13**(4): p. 486-95.

23. Bammer, R. and S.O. Schoenberg, *Current concepts and advances in clinical parallel magnetic resonance imaging.* Top Magn Reson Imaging, 2004. **15**(3): p. 129-58.

24. Shepherd, T.M., et al., *Aldehyde fixative solutions alter the water relaxation and diffusion properties of nervous tissue.* Magn Reson Med, 2009. **62**(1): p. 26-34.

25. Einstein, A., R. Fürth, and A.D. Cowper, *Investigations on the theory of the Brownian movement*. 1956, [New York]: Dover Publications. 119 p.

Chapter 8: Summary and Conclusions

8.1 Summary and conclusions

White matter is comprised of axons that transmit electric signals to and from neurons (1, 2). They can be covered with a myelin sheath that helps improve conduction velocity. Axon morphology is closely related to function. Evaluating axon morphology would provide insights into connectivity, maturation, and disease pathology. Unfortunately, the only way to directly assess axon morphology is histology, which is destructive and cannot be done *in vivo*. Diffusion MRI is a valuable tool for indirectly assessing tissue architecture without resolving the underlying structure (3). Conventional diffusion MRI methods like DWI and DTI can provide metrics that are related to axon morphology, but they cannot measure specific morphologic parameters such as mean axon diameter (MAD) or intracellular space (ICS) volume fraction.

Q-space imaging (QSI) is an advanced diffusion MRI technique that may be able to provide information on axonal architecture not amenable by conventional diffusion MRI techniques. It has already been demonstrated that QSI may be more sensitive than DTI to changes in axon morphology due to pathology (4, 5). However, QSI has several limitations that impair accurate assessment of axonal architecture. First, the maximum gradient amplitude available on the commercial systems is too low for the displacement resolution needed to study axon structure at cellular length scales. Second, QSI of biological tissues is complicated by the presence of water in extracellular and intracellular spaces (ECS and ICS) and exchange of molecules between these compartments. Third, up until now, MAD is the only specific measurement of axon morphology provided by QSI and other metrics would be valuable.

The main objective of this dissertation is to address the above limitations of QSI mentioned and to evaluate its capacity to accurately assess axonal architecture *in vivo*. First, a custom built high amplitude gradient coil was utilized to address the limitations in the maximum gradient amplitude achievable with commercial systems. Second, QSI simulations are used to investigate the effects of the presence of both ECS and ICS signals on QSI. Third, three QSI-based methods (displacement PDF, low q-value, and VGPD) designed to account for ECS and ICS signals and to extract different axonal architecture metrics are evaluated for accuracy and potential application *in vivo*.

The gradient coil was previously built in our laboratory (6). The coil had a maximum gradient of 5000 G/cm and showed reliable ADC measurements and diffusion-weighted images. Based on these results, it was concluded that the gradient coil was suitable for high resolution QSI experiments.

Q-space simulations were performed on both synthetic and histologic images of axons to investigate the effects of having signal from both ECS and ICS and of variability in cell size and shape on QSI measurements of axonal architecture. The simulation results showed that despite all the variable and unknown effects, QSI may still provide accurate measures of axon morphology. The insights from these results support the potential of QSI to indirectly assess axonal architecture

The three QSI-based methods were applied to fixed mouse spinal cords and various white matter tracts were analyzed. The results for each method are described below.

The one-compartment PDF method approach was able to differentiate between WM tracts based only on MAD, although MAD was overestimated by approximately

20%. The two-compartment PDF method separated the ECS and ICS displacement PDF and was able to measure MAD as accurately as compared to histology. It also allowed for measurement of ICS volume fraction and ADD, which provide additional information on axon morphology. However, the accuracy of these measurements is dependent on fulfilling the short gradient pulse (SGP) approximation. Results from increasing the diffusion gradient duration show a narrowing of the displacement PDF as predicted from theory.

The low q-value method has potential to indirectly assess axonal architecture without the need for strong gradients as needed with the displacement PDF method. The one-compartment method shows good correlation with histology, but the two-compartment method may provide accurate estimates of MAD as compared with histology. However, the ICS volume fraction was consistently overestimated by this method. The low q-value method also seems robust to experimental conditions violating the SGP approximation. This suggests the potential for the low q-value method to be implemented on commercial hardware.

The VGPD method has potential to separate ECS and ICS signals without the need for modeling. A QSI subvoxel processing algorithm was developed to increase the apparent displacement resolution and validated with experimental data. Experimental ICS volume fractions showed good correlation with histology. The FWHM, ZDP, and kurtosis of the ICS PDF showed good correlation with histology and the FWHM may provide accurate estimates of MAD as compared with histology. However, the ICS volume fraction was underestimated by this method. The FWHM, and kurtosis of the ECS PDF showed good correlation with histology and may provide a measurement of

ECS tortuosity. Violating the SGP approximation may reduce the accuracy of the VGPD method and underestimate MAD.

All three methods were implemented on a 1.5T Siemens Sonata MRI scanner to investigate their respective feasibility of application on a clinical scanner. The major limitation was the maximum gradient strength available, which restricts the achievable displacement resolution. For the displacement PDF and VGPD methods, this leads to a broadened PDF and decreasing the likelihood of any accurate measurement of axon morphology. The two-compartment low q-value method showed the most promising results that provided anticipated insights into axonal architecture. Unfortunately, there was no histologic data so this method was not rigorously validated.

8.2 Future work

The results of this dissertation demonstrated the potential for QSI and related methods to indirectly and accurately assess axonal morphology and suggest several avenues for future work.

First, histology should be done on the pig spinal cords used in the feasibility study in order to validate the results shown. The low q-value method showed the greatest promise of clinical feasibility and its measurements of MAD and ICS volume fraction need to be compared with histology to evaluate accuracy. If these histology results support the clinical potential of the low q-value method, then further work should include investigating the effects of GM and WM partial voluming on the QSI measures of axon morphology. Also, the implementation should be optimized to reduce scan time.

Second, all the work presented here has only looked at healthy WM tissue and the potential of the methods described in this dissertation to assess changes in axon morphology due to pathology should be investigated. There are several mouse models of WM diseases that could be used. For example, experimental autoimmune encephalomyelitis is an animal model for MS. Another approach could be using a spinal cord injury mouse model where the spinal cord is transected or crushed.

Finally, the feasibility of these methods to assess WM in the tortuous tracts of the brain should be tested. The ability to study WM in the brain would add clinical significance to the methods described in this dissertation. The accuracy of the QSI and related methods rely on the diffusion gradient being applied orthogonally to the WM tract. Different methods have been proposed to correct for non-orthogonal angles for QSI application in the brain (4, 7) and should be investigated for feasibility of implementation with displacement PDF, low q-value, and VGPD methods.

8.3 Literature citations

1. Purves, D., et al., eds. *Neuroscience*. 2nd ed. 2001, Sinauer Associates, Inc: Sutherland, MA.
2. Williams, P.L., et al., eds. *Gray's anatomy: the anatomical basis of medicine and surgery*. 38th ed. 1995, Churchill Livingstone: New York, NY.
3. Le Bihan, D., *Looking into the functional architecture of the brain with diffusion MRI.* Nat Rev Neurosci, 2003. **4**(6): p. 469-80.
4. Assaf, Y., et al., *High b-value q-space analyzed diffusion-weighted MRI: application to multiple sclerosis.* Magn Reson Med, 2002. **47**(1): p. 115-26.
5. Assaf, Y., et al., *High b value q-space-analyzed diffusion MRI in vascular dementia: a preliminary study.* J Neurol Sci, 2002. **203-204**: p. 235-9.
6. Wright, A.C., et al., *Construction and Calibration of a 50 T/m Z-Gradient Coil for q-Space Microscopy*. Journal of Magnetic Resonance, 2007. **186**: p. 17-25.
7. Bar-Shir, A., I.D. Duncan, and Y. Cohen, *QSI and DTI of excised brains of the myelin-deficient rat.* Neuroimage, 2009. **48**(1): p. 109-16.